ISTANBUL TECHNICAL UNIVERSITY ★ GRADUATE SCHOOL

CONVECTION-PERMITTING CLIMATE SIMULATIONS FOR THE 21st CENTURY BASED ON SSP3-7.0 SCENARIO OVER THE BLACK SEA BASIN

M.Sc. THESIS

Mehmet Barış KELEBEK

Department of Meteorological Engineering

Atmospheric Sciences Programme

DECEMBER 2022

ISTANBUL TECHNICAL UNIVERSITY ★ GRADUATE SCHOOL

CONVECTION-PERMITTING CLIMATE SIMULATIONS FOR THE 21st CENTURY BASED ON SSP3-7.0 SCENARIO OVER THE BLACK SEA BASIN

M.Sc. THESIS

Mehmet Barış KELEBEK
(511191031)

Department of Meteorological Engineering

Atmospheric Sciences Programme

Thesis Advisor: Assoc. Prof. Dr. Barış ÖNOL

DECEMBER 2022

ISTANBUL TEKNİK ÜNİVERSİTESİ ★ LİSANSÜSTÜ EĞİTİM ENSTİTÜSÜ

KARADENİZ HAVZASI ÜZERİNDE 21. YÜZYIL İÇİN SSP3-7.0 SENARYOSUNA DAYALI KONVEKSİYONA İZİN VEREN İKLİM SİMÜLASYONLARI

YÜKSEK LİSANS TEZİ

Mehmet Barış KELEBEK
(511191031)

Meteoroloji Mühendisliği Anabilim Dalı

Atmosfer Bilimleri Programı

Tez Danışmanı: Doç. Dr. Barış ÖNOL

ARALIK 2022

Mehmet Barış KELEBEK, a M.Sc. student of İTU Graduate School student ID 511191031, successfully defended the thesis entitled "CONVECTION-PERMITTING CLIMATE SIMULATIONS FOR THE 21st CENTURY BASED ON SSP3-7.0 SCENARIO OVER THE BLACK SEA BASIN", which he prepared after fulfilling the requirements specified in the associated legislations, before the jury whose signatures are below.

Thesis Advisor :	**Assoc. Prof. Dr. Barış ÖNOL** Istanbul Technical University	.....
Jury Members :	**Prof. Dr. Yurdanur ÜNAL** Istanbul Technical University	.....
	Dr. Ozan Mert GÖKTÜRK University of Bergen	.....

Date of Submission : 30 November 2022
Date of Defense : 8 December 2022

To my beloved ones…,

FOREWORD

This is the final report of my M.Sc. thesis before graduation. I would like to thank my advisor Assoc. Prof. Dr. Barış Önol for encouraging me since the beginning of this study. We thank the Turkish State Meteorological Service for providing us with the station observations. We also state that the numerical calculations reported in this paper were fully performed at TUBITAK ULAKBIM, High Performance and Grid Computing Center (TRUBA resources). Finally, I would like to thank my family for being with me during my education life.

November 2022

Mehmet Barış KELEBEK
(Meteorological Engineer)

TABLE OF CONTENTS

Page

ABBREVIATIONS

ARW : Advanced Research WRF
CHIRPS : Climate Hazards Group Infrared Precipitation with Stations
CMIP : Coupled Model Intercomparison Project
CORDEX : Coordinated Regional Climate Downscaling Experiment
COSMO-CLM : Consortium for Small-Scale Modelling CLimate Mode
DJF : Winter
DTR : Diurnal Temperature Range
ERA5 : European Centre for Medium-Range Weather Forecasts Reanalysis 5
GCM : Global Coupled Climate Model
GHG : Greenhouse Gas
GRDC : Global Runoff Data Centre
IPCC : Intergovernmental Panel on Climate Change
JJA : Summer
MAM : Spring
MYJ : Mellor-Yamada-Janjic
MPI-ESM : Max Planck Institute for Meteorology Earth System Model
MPI-ESM-HR : High Resolution MPI-ESM
MSWEP : Multi-Source Weighted-Ensemble Precipitation
PBL : Planetary Boundary Layer
R90P : Very Wet Days Index
R99P : Extremely Wet Days Index
RCM : Regional Climate Model
RCP : Representative Concentration Pathway
RegCM3 : Regional Climate Model Version 3
RMSE : Root Mean Squared Error
SON : Autumn
SRES : Regional Climate Model
SST : Sea Surface Temperature
Tmean : Daily mean 2m air temperature
Tmax : Daily maximum 2m air temperature

Tmin : Daily minimum 2m air temperature
TSMS : Turkish State Meteorological Service
TX90P : Very Warm Days Index
WCRP : World Climate Research Programme
WRF : Weather Research and Forecasting
WRFCP : WRF simulation outputs
WRFV3 : WRF Model Version 3.9.1
YSU : Yonsei University

SYMBOLS

°C	**:** Degree celcius
η	**:** Eta vertical level
$\boldsymbol{p_h}$	**:** Hydrostatic component of the pressure
$\boldsymbol{p_{hs}}$	**:** Bottom boundary pressure value
$\boldsymbol{p_{ht}}$	**:** Top boundary pressure value
$\boldsymbol{C_T}$	**:** Maximum Courant number
$\boldsymbol{\Delta t}$	**:** Timestep
$\boldsymbol{f_d}$	**:** Timestep decrease factor

LIST OF TABLES

Page

LIST OF FIGURES

Page

CONVECTION-PERMITTING CLIMATE SIMULATIONS FOR THE 21st CENTURY BASED ON SSP3-7.0 SCENARIO OVER THE BLACK SEA BASIN

SUMMARY

The human influence on global climate change has been at an unprecedented rate since the pre-industrial era. The general circulation models (GCMs) are the primary tools for climate change studies. Moreover, the regional climate models (RCMs) provide more detailed and physically more reliable climate information at higher resolutions. Recently RCMs are run at a horizontal resolution of higher or equal to 4 km, so-called convection-permitting models (CPMs). In this study, we performed CMIP6-based historical and future convection-permitting climate simulations at 3 km horizontal resolution for 2005-2014 and 2061-2070 periods based on the SSP3-7.0 greenhouse gas emission scenario by using the Weather Research and Forecasting (WRF) model. We downscaled the last generation high-resolution Max Planck Institute for Meteorology Earth System Model (MPI-ESM-HR) outputs over the Black Sea Basin. We evaluated the historical simulation outputs using high-resolution gridded observational and reanalysis datasets and station observations. Following that, we examined the future changes in the climate of the Black Sea Basin.

In terms of maximum temperature, the WRF model has a negative bias in winter and spring, especially in mountainous regions, and a positive bias of about 3°C compared to gridded datasets in summer and autumn over the study area. Compared with the monthly station observations, the WRF model significantly improves MPI-ESM-HR outputs and reduces the bias. Similarly, for the minimum temperatures, although the WRF model has a positive bias of about 4°C compared to the gridded datasets in all seasons, comparisons with station observations show that it significantly improves MPI-ESM-HR outputs by reducing the bias.

In terms of precipitation, compared to gridded datasets, the WRF model has a positive bias of about 6 mm/day in winter over mountainous areas due to the positive bias of MPI-ESM-HR. However, compared with the station observations, the WRF model better estimates the daily precipitation probabilities than one of the MPI-ESM-HR outputs. In particular, it outperforms MPI-ESM-HR for high amounts of daily precipitation exceeding 50 mm at high-elevation stations. Also, the WRF model provides better estimations of 3-hourly precipitation probabilities than MPI-ESM-HR, especially over the northeast of Turkey and the Eastern Black Sea region.

The future climate simulation results show that the daily 2m mean, minimum, and maximum air temperatures increase in the spring, summer, and autumn by about 3°C in the 2061-2070 period over the study area. In the winter, there is a suppression in the warming due to the increased low- and mid-level cloud covers. However, there is regional warming around 1°C over the Carpathians and Eastern Anatolia due to a reduction in the surface albedo. Furthermore, increase in the daily maximum temperatures leads to an increase in the warm extreme conditions in the future.

In terms of precipitation, there is a significant increase in the future by about 3 mm/day in winter over the Eastern Black Sea region. This precipitation increase is due to the increased evaporation enhanced by the warmer sea surface temperature. On the other hand, the total precipitation amount decreases in spring and summer across the study area. Moreover, there is an intensification in the daily and sub-daily precipitation amounts leading to extreme conditions in the subregions of the Black Sea Basin. The maximum daily precipitation amount reaches 350 mm over the northeast of Turkey and Georgia. Also, the daily extreme precipitation thresholds of the 90th, 99th, and 99.9th percentiles shift toward higher values, and the percentage of very wet days increases by about 3% over these regions. Furthermore, the hourly precipitation amounts exceed 100 mm in most coastal subregions. In particular, there is an increase in afternoon precipitation in autumn over the coastal regions of Turkey.

KARADENİZ HAVZASI ÜZERİNDE 21. YÜZYIL İÇİN SSP3-7.0 SENARYOSUNA DAYALI KONVEKSİYONA İZİN VEREN İKLİM SİMÜLASYONLARI

ÖZET

Küresel iklim değişimi üzerindeki insan etkisi sanayi öncesi dönemden bu yana çok yüksek oranda artış göstermiştir. Bu insan etkisine bağlı olarak gelecekte küresel ortalama sıcaklık artışının 2030'lu yıllarda 1.5°C'yi geçeceği tahmin edilmektedir. Ayrıca, sıcaklık artışına bağlı olarak gelecekte aşırı yüksek sıcaklık ve aşırı yağış olaylarında da artış olacağı öngörülmektedir. Bundan dolayı, iklim değişimini azaltma ve uyum çalışmaları için gelecek dönem iklim projeksiyonları büyük önem arz etmektedir. Bu kapsamda, küresel birleşik iklim modelleri (GCM'ler) iklim değişimi çalışmaları için birincil araçlardır. Fakat GCM'lerin yatay çözünürlükleri bölgesel olarak detaylı bilgi elde etmek için yeteri kadar yüksek değildir. Bölgesel iklim modelleri (RCM'ler) GCM'lere kıyasla daha yüksek çözünürlüklerde daha ayrıntılı ve fiziksel olarak daha güvenilir bölgesel iklim bilgisi sağlamaktadırlar. Son zamanlarda RCM'ler, konveksiyona izin veren modeller (CPM'ler) olarak adlandırılan, 4 km'ye eşit veya daha yüksek bir yatay çözünürlükte çalıştırılmaktadır. Biz bu çalışmada, Weather Research and Forecasting (Hava Araştırması ve Tahmini) (WRF) modeli ve CMIP6 tabanlı son nesil yüksek çözünürlüklü Max Planck Meteoroloji Enstitüsü Yer Sistemi Modeli'nin (MPI-ESM-HR) çıktılarını kullanarak, SSP3-7.0 sera gazı emisyon senaryosu altında, sırasıyla 2005-2014 ve 2061-2070 yılları arasında geçmiş ve gelecek dönem 3 km yatay çözünürlükte Karadeniz bölgesi ve Anadolu Yarımadası'nın geniş bir bölümü üzerinde konveksiyona izin veren bölgesel iklim simülasyonları gerçekleştirdik. Çalışmada ilk olarak geçmiş dönem simülasyon çıktılarını yüksek çözünürlüklü ızgaralı gözlemsel ve reanaliz referans veri setleri ve istasyon gözlemleri ile karşılaştırarak model başarımını değerlendirdik. Daha sonra, gelecek dönem simülasyon çıktılarını kullanarak bu bölgedeki gelecek dönem iklim değişimlerini araştırdık.

Mevsimsel maksimum sıcaklık ortalamaları incelendiğinde, ızgaralı gözlemsel ve reanaliz veri setlerine kıyasla, WRF modelinin kış ve ilkbaharda özellikle dağlık bölgelerde negatif yanlılığa, yaz ve sonbaharda ise çalışma alanında yaklaşık 3°C pozitif yanlılığa sahip olduğu tespit edilmiştir. Aylık istasyon gözlemleriyle karşılaştırıldığında ise WRF modelinin istasyon bazında kış ve ilkbahar aylarında negatif yanlılığa sahip olsa da MPI-ESM-HR çıktılarını önemli ölçüde iyileştirdiği ve yanlılığı azalttığı görülmüştür. Benzer şekilde, minimum sıcaklık ortalamaları için WRF modeli tüm mevsimlerde ızgaralı gözlemsel ve reanaliz veri setlerine kıyasla yaklaşık 4°C pozitif yanlılığa sahip olsa da istasyon gözlemleriyle yapılan karşılaştırmalar WRF modelinin MPI-ESM-HR çıktılarını önemli ölçüde iyileştirdiği ve yanlılığı azalttığı tespit edilmiştir.

Yağış çıktıları incelendiğinde MPI-ESM-HR'dan gelen sınır koşullarının pozitif yanlılığı nedeniyle WRF modelinin özellikle kış aylarında ve dağlık bölgelerde yaklaşık olarak 6 mm/gün pozitif yanlılığı vardır. İstasyon gözlemleri ile yapılan aylık

toplam yağış karşılaştırmaları da WRF modelinin bu yanlılığının açık şekilde sınır koşullarından kaynaklandığını göstermektedir. Ancak istasyon gözlemleri ile yapılan günlük toplam yağış karşılaştırmaları sonucunda WRF modelinin MPI-ESM-HR'ın günlük yağış çıktılarını önemli ölçüde iyileştirdiği tespit edilmiştir. Özellikle WRF modelinin yüksek rakımlı istasyon noktalarında 50 mm/gün'ü aşan yüksek miktarlardaki yağış miktarlarını temsil etmede MPI-ESM-HR'dan çok daha iyi olduğu görülmüştür. Ortalama değerler karşılaştırıldıktan sonra günlük aşırı yağışların bir göstergesi olarak MPI-ESM-HR ve WRF modelinin 90., 99. ve 99.9. eşik değerleri hesaplanarak ızgaralı referans verilerinin eşik değerleri ile karşılaştırılmıştır. Bu analiz sonucunda WRF modelinin çok yüksek miktardaki günlük yağışları özellikle dağlık bölgelerde referans veri setleri ile uyumlu olarak MPI-ESM-HR'dan daha iyi temsil ettiği tespit edilmiştir. Mevsimsel ve günlük yağış karşılaştırmalarına ek olarak çalışma alanının alt bölgelerinde gözlem ve reanalize dayalı ızgaralı 3 saatlik toplam yağış verisi ile model çıktıları karşılaştırılarak analizler yapılmıştır. Bu analizler sonucunda WRF modelinin özellikle Türkiye'nin kuzeydoğusunda ve Doğu Karadeniz bölgesinde 3 saatlik yağış olasılıkları için MPI-ESM-HR'dan yüksek miktarlardaki yağışlar için daha iyi sonuçlar verdiği tespit edilmiştir.

Gelecek dönem iklim simülasyonu günlük 2 metre ortalama hava sıcaklığının çalışma alanında kış hariç tüm mevsimlerde istatistiksel olarak anlamlı bir şekilde artacağını, ısınmanın özellikle yaz aylarında 3°C'yi geçeceğini göstermektedir. Kış aylarında ise artan alçak ve orta seviyeli bulutlar nedeniyle ısınmada bir yavaşlama olacağı ve ortalama sıcaklıklarda genel olarak bir değişim olmayacağı öngörülmektedir. Ancak kar örtüsündeki küçülme ile ilişkilendirebileceğimiz yüzey albedosundaki azalma nedeniyle Karpat Dağlarında ve Doğu Anadolu'nun yüksek kesimlerinde bölgesel olarak ısınma olacağı tespit edilmiştir. Bunlarla beraber, maksimum sıcaklıklardaki hızlı artışın gelecekte özellikle Türkiye'nin kuzeybatısında günlük sıcaklık açıklıklarını ve aşırı sıcak günlerin sayısını arttıracağı tespit edilmiştir. Hava sıcaklığına ek olarak Karadeniz'in deniz yüzey sıcaklıklarında tüm mevsimlerde 1.5°C civarında artış olacağı öngörülmektedir.

Gelecek simülasyonunun yağış çıktıları analiz edildiğinde kış mevsiminde çalışma alanında toplam yağış miktarının ve bununla ilişkili olarak yıllık ıslak gün sayısının artacağı tespit edilmiştir. Özellikle Doğu Karadeniz bölgesinin dağlık kesimlerinde bu artışın 3 mm/gün'ü aşacağı öngörülmektedir. Bu yağış artışı kışın deniz yüzeyinin Karadeniz'in güney ve güneydoğusunda belirgin şekilde ısınmasına bağlı olarak yaklaşık %15 oranında artan buharlaşmadan kaynaklanmaktadır. Alt troposferdeki bu ek nem içeriği 850 hPa seviyesinde gelecekte hızlanan ortalama batılı akışla Karadeniz'in doğu kıyısına taşınarak yağışı arttırır. Ayrıca 850 hPa seviyesindeki zayıflayan güneyli rüzgar bileşeni Türkiye kıyılarındaki nem içeriğini artırmakta ve orografik zorlama ile birlikte yağış artışına sebep olmaktadır. Toplam yağış miktarları ilkbahar ve yaz ayları için incelendiğinde gelecekte azalma olacağı bulunmuştur. Analizler sonbahar aylarında Türkiye'nin Karadeniz kıyılarında 1 mm/gün yağış artışı olacağını gösterse de bu artışın istatistiksel olarak anlamlı olmadığı tespit edilmiştir.

Çalışmada yağışlardaki mevsimsel ortalama değişimlere ek olarak günlük aşırı yağışlardaki değişimler de araştırılmıştır. Sonuçlar özellikle Türkiye'nin Karadeniz kıyılarında ve Gürcistan'da çok yağışlı günlerin yaklaşık %3, aşırı yağışlı günlerin ise yaklaşık %1 oranında artacağını göstermiştir. Buna ek olarak, günlük toplam yağışların 90., 99. ve 99.9. persantil değerlerinin yine aynı bölgelerde 18 mm'ye varan artış göstereceği tespit edilmiştir. Gelecek dönem maksimum günlük toplam yağış değerlerinin de bu bölgelerde 350 mm'nin üzerine çıkacağı öngörülmektedir. Benzer

günlük yağış analizleri çalışma alanının alt bölgeleri için de yapılmıştır. Analizler günlük aşırı yağışların özellikle Batı, Orta ve Doğu Karadeniz Bölgesi ve Gürcistan gibi kıyı bölgelerde gelecekte artış göstereceğine işaret etmektedir.

Kıyı bölgelerdeki günlük aşırı yağışların artışını daha detaylı incelemek için bu bölgelerde gün içi saatlik yağışların değişimi de incelenmiştir. Sonuçlar Türkiye'nin Karadeniz kıyı bölgelerinde ve Karadeniz'in doğu kıyı bölgelerinde saatlik yağışların gelecekte artacağını ve 100 mm'nin üzerine çıkabileceğini göstermektedir. Saatlik yağışların ortalama günlük çevrimi incelendiğinde öğleden sonra yağışlarında kıyı bölgelerinde özellikle yaz aylarında gelecekte azalma olacağı tespit edilmiştir. Sonbahar aylarında ise öğleden sonra yağışlarında Türkiye'nin Batı, Orta ve Doğu Karadeniz Bölgelerinde ve İstanbul'da artış olacağı öngörülmektedir.

1. INTRODUCTION

The anthropogenic forcing on global climate change is at a remarkable level compared to the pre-industrial era. According to the Sixth Assessment Report of the United Nations Intergovernmental Panel on Climate Change (IPCC AR6), in the 2011-2020 period, the global surface temperature increased by 1.09°C compared to the 1850-1900 period, and this increase is projected to reach 1.5°C global warming level in the early 2030s (Arias et al., 2021). Moreover, the human influence on the observed changes in the climate extremes is also beyond doubt, and the projections show that these extremes will increase in the future (Seneviratne et al., 2012; Seneviratne et al., 2021). In particular, warm extremes will become more frequent and intense globally, cold extremes will decrease, and regional warming trends will play a role in the extreme precipitation intensification (Seneviratne et al., 2021). Furthermore, compound extremes, for example, concurrent heat waves and extreme drought or extreme precipitation along with extreme wind events, will increase in the future with higher global warming rates (Seneviratne et al., 2021; Vogel et al., 2020), leading to an increase in the human exposure to multivariate climate extremes across the globe (Batibeniz et al., 2022). Therefore, future projections of the Earth's climate play a critical role in developing adaptation and mitigation strategies. In this context, one of the essential tools for climate change studies is the general circulation models (GCMs). GCMs simulate the Earth's climate by numerically solving the governing equations of the atmosphere and ocean based on physical and dynamical assumptions and represent the interactions through the coupling of atmosphere-ocean-cryosphere-land components of the climate system (Meehl et al., 1997). Besides, greenhouse gas (GHG) emission scenarios represent the human influence on climate change in the models. These scenarios estimate the future concentration of GHGs, such as carbon dioxide (CO_2), chlorofluorocarbons (CFCs), and methane (CH_4), based on socioeconomic development strategies. To this end, the IPCC introduced the IS92 scenarios (Houghton et al., 1992), the first full suite of global GHG emission scenarios (Nakićenović, 2000), and they were used in the models contributing to the IPCC

Second Assessment Report (Houghton, 1996). The IPCC updated these estimates in the Special Report on Emissions Scenarios (SRES) (Nakićenović, 2000). Furthermore, the World Climate Research Programme (WCRP) organized the Coupled Model Intercomparison Project (CMIP) activity in 1995 under the sponsorship of the Climate Variability and Predictability (CLIVAR) project for the systematic evaluation of the capability of GCMs by the scientific community (Meehl et al., 1997, 2000). The aims of the first and the second phases of the project, CMIP1 and CMIP2, respectively, were to document the performance of the models in simulating the historical climate (CMIP1) and to study the future climate change due to a 1% increase in CO_2 per year (CMIP2) (Meehl et al., 1997, 2000). Along with the several simulations based on the SRES projections, the outcomes of CMIP1 and CMIP2 experiments were used in the documentation of the IPCC Third Assessment Report (Watson et al., 2001). In the third phase of the CMIP (CMIP3), global climate simulations were performed under the SRES emission scenarios (Meehl et al., 2007), and these experiments have been the bases for the IPCC Fourth Assessment Report (Pachauri, 2008). In 2007, the IPCC presented the Representative Concentration Pathways (RCPs) to define future climates based on GHG concentrations under different mitigation strategies (Moss, 2008). The RCPs were used as inputs to the GCMs in the fifth phase of the CMIP (CMIP5) (Taylor et al., 2012), contributing to the IPCC Fifth Assessment Report (Pachauri and Mayer, 2015). The most recent future GHG scenarios are the Shared Socioeconomic Pathways (SSPs) based on different climate policies (O'Neill et al., 2017), and they were used as inputs to the models that contributed to the sixth phase of the CMIP (CMIP6) (Eyring et al., 2016). The results of the CMIP6 simulations were used in the preparation of the IPCC AR6 (Arias et al., 2021).

GCMs are of great importance for global climate change studies. On the other hand, despite having global effects, societal and environmental impacts of climate change are not the same for every region because regional climate change and changes in the extremes are the results of global forcing along with small-scale processes and local feedbacks (Dobles-Reyes et al., 2021; Seneviratne et al., 2021). The current horizontal resolution of most of the GCMs is around 100 km, which is inadequate for detailed regional climate change research or impact assessment. In this context, regional climate models (RCMs) (Dickinson et al., 1989; Giorgi and Bates, 1989) have been introduced to produce more detailed and physically more reliable regional climate

information compared to the GCM outputs (Feser et al., 2011; Giorgi, 2019; Gutowski et al., 2020; Prein et al., 2013; Rummukainen, 2016). RCMs are limited area models that take their boundary conditions from a GCM or are nested in another RCM to dynamically downscale the climatic variables in a historical or scenario-based future period. Their higher horizontal resolution compared to the GCMs, most of which are around 10 km, allows them to better capture small-scale and extreme weather events by enabling a better representation of complex topography and surface characteristics over mountainous and coastal areas (Feser et al., 2011; Giorgi, 2019; Rummukainen, 2016). Furthermore, the WCRP initialised the Coordinated Regional Climate Downscaling Experiment (CORDEX) framework for the coordinated evaluation and improvement of the regional climate downscaling techniques and production of fine-scale climate projections by promoting the interactions among the regional and global modelling community and the end-users (Giorgi et al., 2009; Giorgi and Gutowski, 2015). Recently, regional ensemble climate simulations have been performed over nine CORDEX domains, Europe, Africa, South Asia, East Asia, Southeast Asia, Australia, North America, Central America, and South America, under the CORDEX Coordinated Output for Regional Evaluations program (Giorgi et al., 2022; Gutowski Jr. et al., 2016). The RCMs used in the project downscaled the GCMs from the CMIP5 under different RCP scenarios at 25 km horizontal resolution (12 km for Europe) to investigate the future changes in the climate of these regions (Giorgi et al., 2022). Furthermore, numerous regional climate simulations have been performed under the Med-CORDEX initiative (Ruti et al., 2016) to assess the future climate change over the Mediterranean region. The simulations done by the CORDEX community have partly been used to assess regional climate projections in the IPCC AR6 (Diez-Sierra et al., 2022).

Despite the usefulness and benefits of the RCMs, unresolved sub-grid scale thermodynamic and dynamic processes are still parametrized at the current resolutions of RCMs (Kendon et al., 2017), which makes their performance questionable. In particular, convective parametrizations are the primary source of errors and uncertainties in climate simulations (Fosser et al., 2015; Hohenegger et al., 2008; Kendon et al., 2014; Lucas-Picher et al., 2021; Prein et al., 2015, 2020) which have primarily been developed for the simulation of convection over the Tropics at a low (50-100 km) resolution (Hohenegger et al., 2008). Moreover, the convective

parametrization scheme interacts with other parametrization schemes and further increases the uncertainty (Prein et al., 2015). The main problems of the convection-parametrizing RCMs are (i) the diurnal cycle of precipitation is not captured by the model because of the earlier peak in the precipitation due to the early-triggered convection by the parametrization scheme, and (ii) the poor performance in the representation of precipitation intensity (Dai et al., 1999; Kendon et al., 2012, 2017). To these issues, recent RCMs are run at grid spacings less than 4 km with increasing computational power (Prein et al., 2020). At these resolutions, RCMs resolve topography and land-surface processes at a scale that allows the explicit representation of deep convection without a convective parametrization scheme (Fosser et al., 2015; Hohenegger et al., 2008; Kendon et al., 2012). They are called the convection-permitting models (CPMs), in which the mesoscale convective organization and large storms are mostly resolved (convection-permitting scale), yet the convective plumes are unrepresented (Kendon et al., 2014). To avoid confusion, hereafter the term RCM refers to the convection-parametrizing RCM.

1.1 Literature Review

In the near past, many hindcast or historical simulations have been performed at the convection-permitting scale for different periods to test the regional performance of CPMs. For the first time, Hohenegger et al. (2008) tested the suitability of the COSMO-CLM model for climate applications at the convection-permitting scale by performing a month-long simulation over the Alpine region at 2.2 km horizontal resolution in July 2006 and compared the results with the driving 25 km grid-spacing RCM outputs. They found that the 2.2-km simulation improves the representation of the diurnal cycle of precipitation, spatial characteristic of the precipitation maximum, and reduces the cold bias. Prein et al. (2013) performed ten different seasonal simulations over the Eastern Alpine region at 10 km and 3 km horizontal resolutions to highlight the added values of the CPMs using three different limited area models for the summer and winter of 2007 and 2008, respectively. They indicated that the 3-km simulations outperformed the 10-km simulations in terms of temporal and spatial aspects and the representation of extreme precipitation events. Leutwyler et al. (2016) used a version of the COSMO model which is capable of running on a graphics processing unit to perform convection-permitting simulations over continental Europe

at 2.2 km horizontal resolution nested in a 12-km RCM for a week-long case-study in February 2007 and for the seasonal simulation of summer of 2006. They found that 12-km and 2.2-km simulations were similar for the winter simulation in terms of the synoptic development and the cloud and precipitation pattern, while they significantly differ for the summer simulation regarding the precipitation rates for different regions. Furthermore, a seasonal convection-permitting simulation over the complex topography of the Tibetan Plateau at 4 km horizontal resolution for the summer of 2014 by Liu et al. (2022) improved the characteristics of summer precipitation compared to its driving 28-km RCM. Similar results were found by Yun et al. (2020) in the perpetual warm season (from April to August) convection-permitting simulations over Eastern China at 3 km horizontal resolution between 2008-2017.

At the climate scale, Kendon et al. (2012) performed convection-permitting simulations over a region of the UK at 1.5 km horizontal resolution nested in a 12-km driving RCM between 1989-2008. Their results highlighted the improvements in the representation of precipitation intensity, the spatial structure of precipitation amount, and the hourly precipitation extremes (Kendon et al., 2014) at 3 km resolution. (Fosser et al., 2015) and (Brisson et al., 2016) performed simulations over southwest Germany between 1968-1999 and over Belgium between 2000-2010, respectively, at 2.8 km horizontal resolution and showed the improvements in the diurnal cycle of precipitation, precipitation intensity, and the spatial distribution of precipitation amount compared to 7-km RCM simulations. Ban et al. (2014) found similar results for the Alpine region between 1998-2007 in a 2.2-km COSMO-CLM simulation. Yürük and Ünal ran COSMO-CLM at the convection-permitting scale between 1971-2005 and compared simulation outputs with the observations to highlight the added value of the CPM in representing the seasonal means of temperature and precipitation (2017a) and climate extremes over Istanbul (2017b). Leutwyler et al. (2017) performed a decadal convection-permitting simulation over continental Europe at 2.2 km horizontal resolution nested in a 12-km RCM between 1999-2008. They found that the explicit representation of convection in the CPM improved the summer precipitation amount in terms of the diurnal cycle, wet hour frequency, of which the improvements are more pronounced over complex topography, and the extremes. Another 10-year-long climate simulation by Fumière et al. (2020) between 1997-2006 indicated the benefits of a 2.5-km CPM in the representation of fall season heavy precipitation

events over Mediterranean France. Berthou et al. (2020) performed convection-permitting simulations using two CPMs run by ETH Zürich and the Met-Office at 2.2 km horizontal resolution nested in a 12-km domain over Central Europe, the UK and the Mediterranean coasts between 1999-2007 to evaluate the model performances. They indicate that both models at the convection-permitting scale produce more intense and short-lasting precipitation events and improve the diurnal cycle of precipitation compared to 12-km simulations. Furthermore, climate simulations by Stocchi et al. (2022) point outs the improvements in the precipitation characteristics and the representation of extremes in the 3-km horizontal resolution CPM compared to its driving 12-km boundary conditions over the Alps, Central East and South East Europe between 2000-2009. Additionally, results of the convection-permitting climate simulations over North America by Pal et al. (2019) (3-km; 2000-2010 period) and Prein et al. (2020) (4-km; 2000-2013 period) highlighted a better representation of the characteristics of mesoscale convective systems in the CPMs.

In recent years, multi-model ensemble simulations at convection-permitting scale have become available. For the first time, Coppola et al. (2020) presented an ensemble convection-permitting climate experiments project under the CORDEX Flagship Pilot Studies (CORDEX-FPS) program, aiming to investigate convective processes and related extremes over Europe and the Mediterranean regions. They selected three test cases and performed 19 simulations using six CPMs with different model configurations: a summertime extreme precipitation event over Austria, a fall Foehn event over the Swiss Alps, and a fall event along the Mediterranean coast. The models were initialized just before the event in "weather-like mode" and one month before the event in "climate mode". They found that all models capture the events satisfactorily in the weather-like mode. In the climate mode, models also capture the fall events while the spread increases between the models.

Land – atmosphere (Dirmeyer et al., 2013) and soil moisture – climate (Seneviratne et al., 2013) interactions have significant importance in the future projection of temperature and precipitation extremes. Along with the better representation of convective development, the diurnal cycle of precipitation, precipitation amount and intensity, and the spatial distribution of precipitation amount, according to the IPCC AR6, there is medium evidence and high agreement that convection-permitting simulations are necessary to simulate soil-moisture – precipitation feedback

mechanisms realistically (Dobles-Reyes et al., 2021). Numerous studies focus on the sign and the magnitude of the soil moisture – precipitation feedback in convection-permitting simulations. Hohenegger et al. (2009) performed 25-km convection-parametrizing and 2.2-km convection-permitting simulations to test the model sensitivity by perturbing the initial soil moisture conditions over the Alpine region in July 2006. They indicated that the wetter soil conditions resulted in more precipitation in the 25-km simulation, whereas this feedback reversed in the 2.2-km runs because of stronger thermals over drier soil conditions. Taylor et al. (2013) indicates that convection-permitting simulations over the Sahel region imply a negative soil moisture – precipitation feedback in agreement with the observations. Leutwyler et al. (2021) performed convection-permitting simulations over Europe and highlighted the relationship between soil moisture and precipitation intensity.

In addition to hindcast and historical simulations, there are also future scenario downscaling experiments benefiting the advantages of the CPMs. Ban et al. (2015) downscaled the low-resolution Earth System Model of the Max-Planck-Institute outputs to 2.2 km horizontal resolution using COSMO-CLM CPM over the greater Alpine region nested in a 12-km European domain between 1991-2000 as the reference period, and 2081-2090 for the RCP 8.5 future scenario. Their simulations project a decrease in the mean summer precipitation over middle and southern Europe, while heavy precipitation events are becoming more frequent and intense at daily and hourly time scales. Furthermore, Ban et al. (2020) evaluated the performance of the 12-km convection-parametrizing and 2.2-km convection-permitting models (Ban et al., 2014) and investigated future changes in the precipitation (Ban et al., 2015) using the generalized extreme value theory over the aforementioned Alpine area. They indicate that convection-permitting simulation reduced the biases in precipitation frequency and intensity and highlighted the significant improvements in sub-daily precipitation. In the future simulation, they found a decrease in mean precipitation in winter and the difference between the models is low. Controversially, their results indicate an increase in hourly summer precipitation intensity, which is much higher in the 2.2-km simulation. Knist et al. (2020) ran the Weather Research and Forecasting (WRF) model at 3 km horizontal resolution nested in a 12-km European domain using ERA-Interim reanalysis to evaluate the model performance and using the low-resolution Earth System Model of the Max-Planck-Institute outputs to investigate the future changes

based on the RCP 4.5 scenario over Central Europe. They found that the 3-km convection-permitting simulation better captured the heavy and extreme hourly precipitation frequencies than the 12-km run. Also, their future simulations projected a slight decrease in mean summer precipitation for the 2038-2050 and 2088-2100 periods. On the other hand, they found an increase in heavy and hourly extreme precipitation intensities, higher in the convection-permitting simulation. At the continental scale, Liu et al. (2017) performed convection-permitting simulations using the WRF model to downscale the ERA-Interim reanalysis to 4 km horizontal resolution over North America in the October 2000-September 2013 base period. Also, they applied pseudo global warming approach based on the RCP 8.5 future scenario. Despite the regional differences, they found a general agreement between model outputs and observations for precipitation and temperature. Their projection suggests an increase in temperature and precipitation over most of their study area at seasonal time scale. For the first time over a Europe-wide domain, Chan et al. (2020) performed convection-permitting future simulations at 2.2 km horizontal resolution using UK Met-Office Unified Model under RCP 8.5 scenario between 2099-2108 and compared the results with its driving HadGEM3 GCM outputs. Their results indicate that the decrease in mean summer and autumn precipitation and increase in the mean winter precipitation in the CPM are generally controlled by the driving GCM. On the other hand, they highlighted the intensification of summer and autumn precipitation extremes which is more pronounced in the CPM. Sonuç et al. (2022) performed convection-permitting climate simulations based on the RCP8.5 scenario by using COSMO-CLM to investigate the future changes in the climate of northwestern Turkey.

1.2 Purpose of Thesis

The Black Sea region and the Anatolian Peninsula, with a complex topography and where strong land-sea interaction takes place, are one of the climate change hotspots in the Mediterranean region (Cos et al., 2022; Diffenbaugh and Giorgi, 2012; Giorgi, 2006; Kelebek et al., 2021; Lionello and Scarascia, 2018). Therefore, projections of the climate over this region play a critical role in developing suitable regional climate policies. Accordingly, this region has become the subject of numerous climate modelling studies. Önol and Semazzi (2009) performed climate simulations at 30 km horizontal resolution to investigate the future changes in the climate of the Eastern

Mediterranean region by using the RegCM3 model based on IPCC's SRES A2 GHG emission scenario. They found a significant increase in the winter precipitation between 2071-2100 over the eastern coast of the Black Sea, the Caucasus Mountains, the Kaçkar Mountains, and the Carpathian Mountains. They also highlighted the temperature increase across their study area. Önol and Unal (2014) analysed the outputs of these simulations over the climatic regions of Turkey and found that the projected warming rates will be the highest over the Marmara and the Aegean regions of Turkey. They state that increase in the future precipitation over the Black Sea region is due to the strengthening of the northerly 850 hPa wind pattern, which enhances the orographic forcing over this region. Önol et al. (2014) performed future climate simulations using the RegCM3 model forced with different boundary conditions coming from three GCMs for the 21st century based on SRES A2, A1F1, and B1 GHG emission scenarios over the Eastern Mediterranean – Black Sea region. They compared the simulation outputs with present-day climate simulations of Bozkurt et al. (2012) and found an increase in the temperature for each scenario simulation over their study area. Moreover, they indicate that winter runoff will increase over the mountainous region of Turkey, feeding many river systems due to the acceleration of the snowmelt process at higher elevations.

In addition to climate change simulations, several studies have investigated the possible impacts of the sea surface temperature (SST) increase over the Black Sea on the precipitation of its surrounding area by using limited area models because the warming of the Black Sea in recent decades (Lima et al., 2021; Mohamed et al., 2022; Sakalli and Başusta, 2018; Shaltout and Omstedt, 2014), which is projected to continue in the future (Sakalli and Başusta, 2018; Shaltout and Omstedt, 2014), has led to the intensification of extreme precipitation events around this region (Aksu et al., 2022; Meredith et al., 2015). Bozkurt and Sen (2011) performed 10-years long climate sensitivity simulations at 30 km horizontal resolution by increasing the observed SST values by 2 K of the seas surrounding the Anatolian Peninsula using the RegCM3 model. Their results highlight that increasing the SST of the Black Sea increases the precipitation around its basin and the Anatolian Peninsula, especially in summer and autumn. Meredith et al. (2015) performed convection-permitting simulations to test the sensitivity of the July 2012 extreme precipitation event over the town of Krymsk in the eastern Black Sea to the increased SST values using the WRF model. In this

case study, they performed simulations by removing the warming trend in the observed SSTs and found a more than 300% reduction in the simulated precipitation amount for colder conditions. Doğan (2018) performed simulations in a nested domain with a horizontal resolution of 27-9-3 km to examine the sensitivity of the August 2015 heavy rainfall event to SST in the province of Artvin, located in the Eastern Black Sea Region of Turkey by using the WRF model. As a result of the study, they found that higher SST values generally increased the precipitation amount. Moreover, they found that changing the SST values also changed the areal distribution of precipitation amount in several simulations.

The previous studies provided valuable climate information for the Black Sea region and the Anatolian Peninsula. However, the horizontal resolution of the RCMs used in these studies is low compared to recent RCMs, or high-resolution CPMs are only used for short-period case studies. On the other hand, high-resolution climate simulations are necessary to obtain detailed and reliable climate information over these regions, given the complex topographical features of the area and the effects of future SST increase on extreme precipitation. For example, Önol (2012) found in his climate simulations that there is an improvement in the representation of temperature and precipitation in the 10 km horizontal resolution nested domain compared to its mother 50-km domain over the coasts of Turkey. Moreover, the climate simulations in the previous studies are based on SRES GHG emission scenarios, which have been succeeded by the RCP and SSP scenarios. In this study, given the benefits of the CPMs, we performed convection-permitting historical and future climate simulations at 3 km horizontal resolution by using the WRF model for the periods of 2005-2014 and 2061-2070, respectively, based on the last generation SSP3-7.0 GHG emission scenario over the Black Sea Basin, including the coastal areas of the Black Sea and a broad part of the Anatolian Peninsula. For the first time, we downscaled the CMIP6 high-resolution Max Planck Institute for Meteorology Earth System Model (MPI-ESM-HR) (Gutjahr et al., 2019) outputs over the area of interest to further improve our understanding of climate change in this region.

2. METHOD AND DATA

In the study, we performed our climate simulations using the WRF model Version 3.9.1 (Skamarock et al., 2008), and we evaluated the model performance using high-resolution gridded reanalysis and observational datasets, in addition to station observations. Following that, we investigated future changes in the climate of the Black Sea region and the Anatolian Peninsula. This section gives information about the model used for simulations, the study area and simulation design, and the data used in the study.

2.1 Weather Research and Forecasting Model Version 3.9.1 (WRFV3)

The WRFV3, with its fully compressible, non-hydrostatic Advanced Research WRF (ARW) dynamics solver and physics options, including microphysics, atmospheric radiation physics, and surface and planetary boundary layer (PBL) physics, is an atmospheric simulation system used for both numerical weather prediction and research applications (Skamarock et al., 2008). It has been developed in a collaboration among the National Center for Atmospheric Research's Mesoscale and Microscale Meteorology Division, the National Oceanic and Atmospheric Administration's National Center for Environmental Prediction and Earth System Research Laboratory, the Department of Defense's Air Force Weather Agency and Naval Research Laboratory, the Center for Analysis and Prediction of Storms at the University of Oklahoma, and the Federal Aviation Administration. It can be used in computing environments from supercomputers to laptops with its flexible and modular source code (Skamarock et al., 2008).

The ARW solver of the WRFV3 uses a terrain-following hydrostatic-pressure vertical coordinate system which is denoted by η in Figure 2.1 and defined as

$$\eta = (p_h - p_{ht})/\mu \tag{2.1}$$

where $\mu = p_{hs} - p_{ht}$. p_h is the hydrostatic component of the pressure, and p_{hs} and p_{ht} are bottom and top boundary pressure values, respectively. η ranges from 1 at the

surface to 0 at the top boundary. As the spatial discretisation, the ARW solver uses a C grid staggering where the normal velocities are staggered one-half grid length from the thermodynamic variables at the mass point of the grid, as shown in Figure 2.2 (Skamarock et al., 2008).

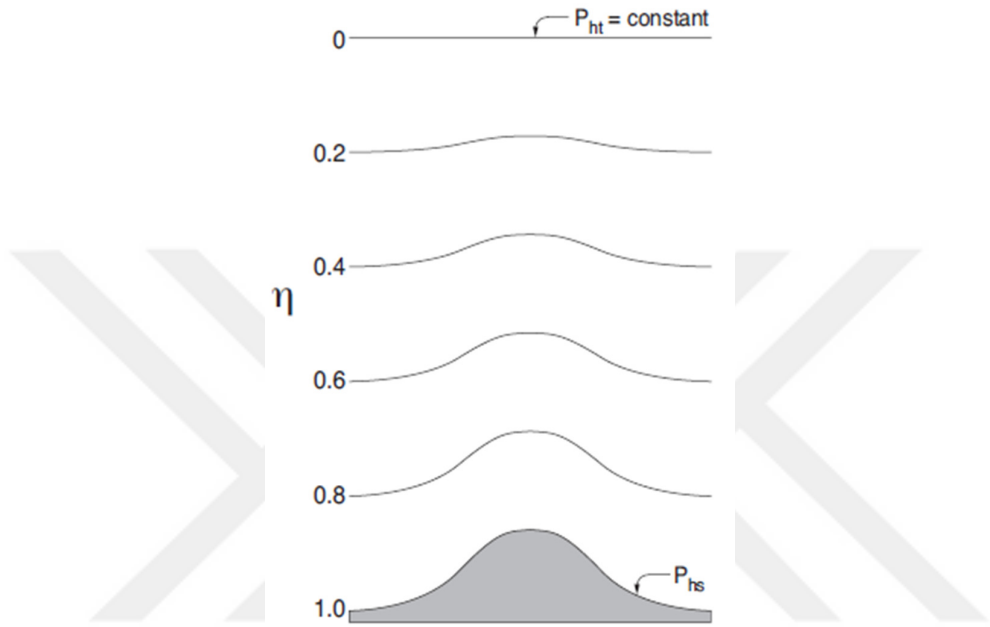

Figure 2.1 : The WRFV3 vertical coordinate system (adopted from Skamarock et al. (2008)).

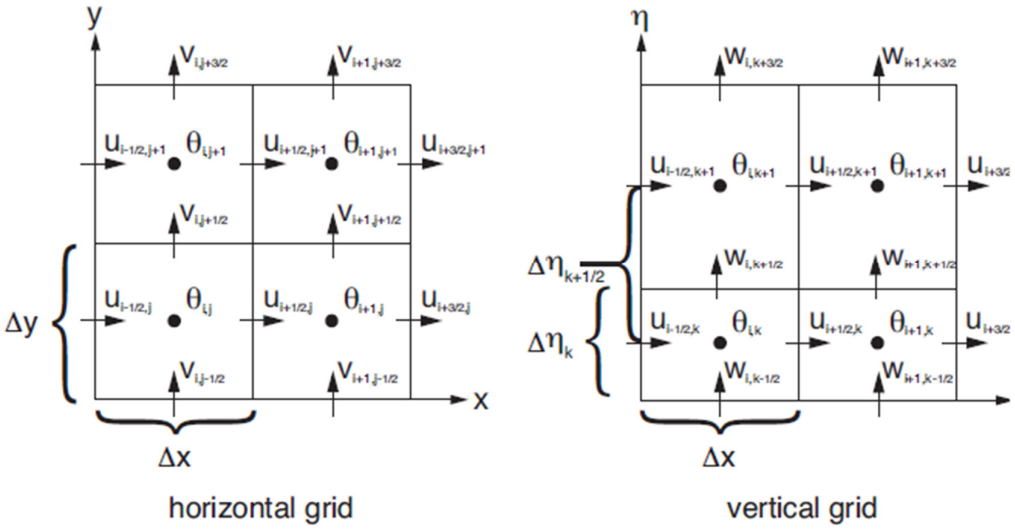

Figure 2.2 : The WRFV3 horizontal C grid staggering system (adopted from Skamarock et al. (2008)).

The ARW solver uses a third-order Runge-Kutta time integration scheme and has an adaptive time stepping capability, which chooses the timestep based on the wind fields varying in time. Adaptive time stepping capability lets the model choose an integration timestep regarding the model stability based on a target maximum Courant number ($C_{T_{target}}$), which is between 1.1 and 1.2 and reduces the wall-clock time of simulation compared to integrations with a fixed timestep. In general, the maximum stable timestep is higher than the fixed timestep (Skamarock et al., 2008). In the adaptive timestep scheme, the maximum Courant number in the domain is calculated ($C_{T_{domain}}$) for each velocity component, u, v, and w, and checked whether is lower than the $C_{T_{target}}$. If so, the integration timestep is increased by calculating the new timestep using

$$\Delta t_{current} = \min\left(1 + f_i\,, \frac{C_{T_{target}}}{C_{T_{domain}}}\right).\Delta t_{previous} \tag{2.2}$$

where $f_i \leq 5\%$ for the regulated increase. If $C_{T_{domain}}$ exceeds the $C_{T_{target}}$, then the timestep is reduced as

$$\Delta t_{current} = \min\left(1 - f_d\,, \frac{C_{T_{target}} - 0.5(C_{T_{domain}} - C_{T_{target}})}{C_{T_{domain}}}\right).\Delta t_{previous} \tag{2.3}$$

where $f_d = 25\%$ is the timestep decrease factor. The upper and lower bounds on the adaptively-chosen timestep are based on the model's horizontal resolution (Skamarock et al., 2008).

2.2 Simulation Domain

We ran the WRF model at 3 km horizontal resolution over the Black Sea region and a broad part of the Anatolian Peninsula (hereafter BSA), which is shown in Figure 2.3. The BSA has a complex topography and has an area of approximately 1641x1092 km^2 with 547 and 364 grid points in east-west and north-south directions, respectively. It is surrounded partly by the Carpathian and Balkan Mountains in the west, the Black Sea and Eastern Anatolia mountains in the south, and the Caucasus Mountains in the east and the model elevation reaches up to 3000 metres. As a moisture source, the Black Sea has a significant impact on the regional climate. For example, northerly flow carries moisture from the Black Sea to the northern coasts of Turkey and causes high amount of precipitation with enhanced orographic forcing (Bozkurt and Sen, 2011).

Furthermore, northeasterly flow over the Black Sea in the winter causes sea-effect snow in Istanbul, which is the most populated metropolitan of this area (Kindap, 2010). Therefore, we selected our simulation domain covering the entire Black Sea to represent its impacts within the simulations. This domain is a slightly modified version of the one used in Doğan (2018).

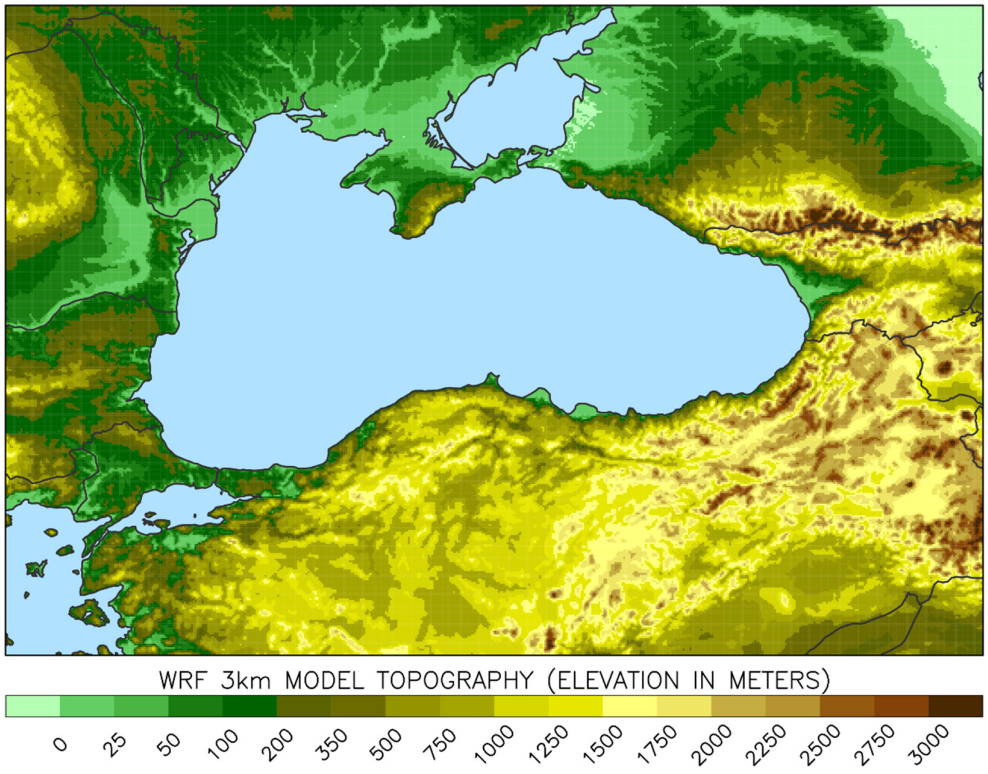

Figure 2.3 : The simulation domain topography.

2.3 Selection of GCM, Simulation Period and SSP3-7.0 Scenario

For the simulations, we provided the lateral boundary conditions with the outputs of the MPI-ESM-HR at a horizontal resolution of ~100 km at 28 isobaric levels at 6-hour intervals, including the SST. We used the MPI-ESM-HR GCM outputs because:

- MPI-ESM-HR is a comprehensive GCM with atmospheric, land-surface, ocean, and sea ice components and has a higher resolution than the standard horizontal resolution of the CMIP6 by following the High Resolution Model Intercomparison Project (Haarsma et al., 2016) protocol (Gutjahr et al., 2019).
- Boundary conditions directly affect regional climate simulation results. In this context, the MPI-ESM-HR represents the temperature and precipitation

climate over Turkey better than most of the CMIP5 and CMIP6 models (Bağçaci et al., 2021), increasing our confidence in data quality for boundary conditions.

- Certain variables are required to run the WRF model (Skamarock et al., 2008), and these variables are stored in the Earth System Grid Federation repositories where the MPI-ESM-HR outputs are at ~100 km horizontal resolution and 6-hour intervals. On the other hand, to our knowledge, not every CMIP6 GCM outputs for all required variables are stored at 6-hour intervals.

We performed historical and future climate simulations between September 1, 2004 - January 1, 2015, and September 1, 2060 - January 1, 2071, respectively. The first four months of the simulations are left as spin-up time, and the outputs are not included in the analyses. We selected the 2005-2014 period as the reference period because it is temporally the nearest period to the current climatic conditions (Historical CMIP6 simulations end at the end of 2014.). We chose the future simulation period after analysing MPI-ESM-HR outputs to find the local maxima of the SST values over the Black Sea and the daily maximum precipitation amount for each month over the Black Sea coast of Turkey over the years. Figure 2.4 shows the annual mean SST for the historical (1980-2015) and the SSP3-7.0 based future (2015-2100) periods over the Eastern and the Western Black Sea. The results show that the annual mean SST of the Eastern and the Western Black Sea will continuously increase from 2061 to 2070 until reaching local maximums of about 18.5°C and 18°C, respectively.

Figure 2.5 shows the daily maximum precipitation amount for each month for the historical and the SSP3-7.0 based future periods over the Black Sea coast of Turkey. The results show that MPI-ESM-HR has local maxima of daily precipitation between 2061-2070 in February, March, May, September, October, and December. Given these SST and precipitation extremes, and as being a mid-century period, we selected 2061-2070 as the future simulation period.

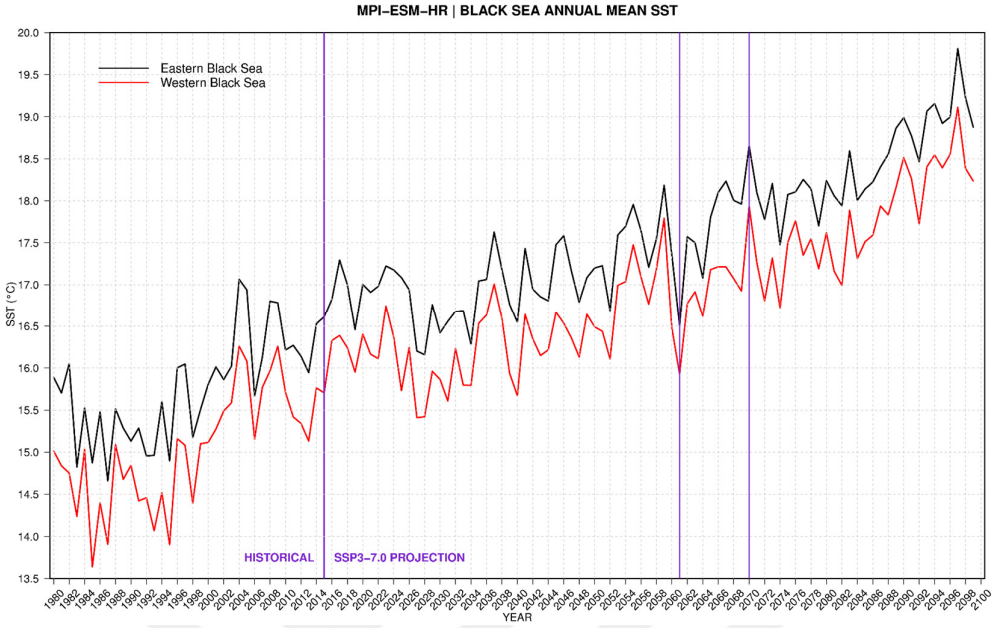

Figure 2.4 : The annual mean SST of MPI-ESM-HR averaged over the Eastern (black) and the Western (red) Black Sea.

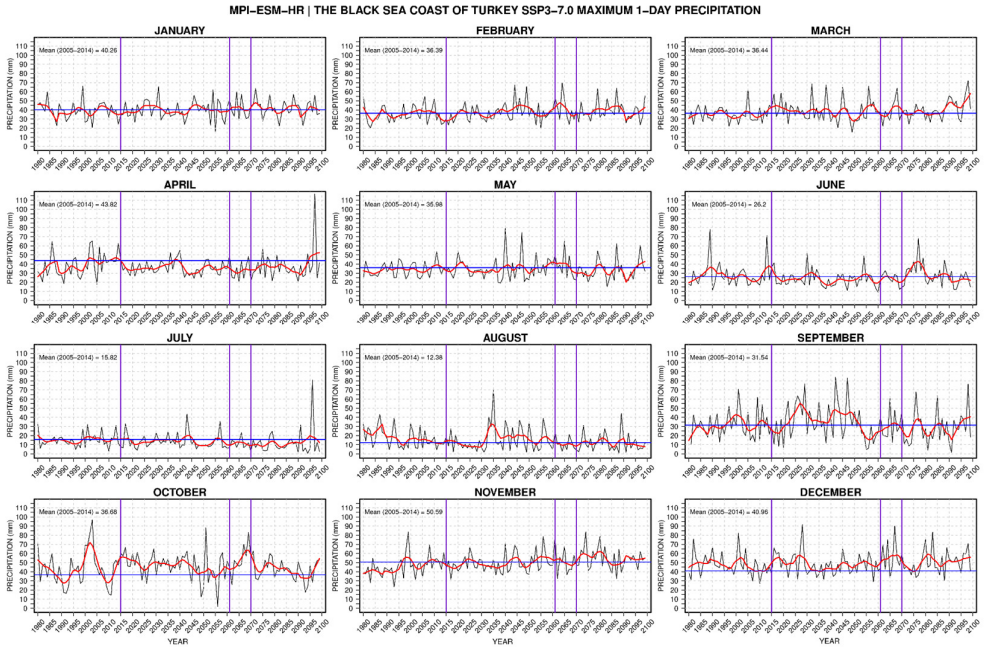

Figure 2.5 : The daily maximum precipitation of MPI-ESM-HR over the Black Sea coast of Turkey. The blue line is the 2005-2014 period average, the red line is the smoothed time series curve.

Our simulations are based on SSP3-7.0 GHG emission scenario. SSP scenarios have been developed considering the future changes in the human environment, including demographics, economy and technology, and changes in the natural environment and

resources (O'Neill et al., 2017). SSP scenarios generally project higher GHG concentrations in the future than preceding RCP scenarios (Meinshausen et al., 2020). SSP3-7.0 scenario projects strict regionalisation policies with a low international priority on environmental issues in the future (O'Neill et al., 2017) and a radiative forcing of 7 W/m^2 by the end of 2100 (Meinshausen et al., 2020). In addition, the SSP3-7.0 scenario projects a higher concentration of CO_2 and CH_4 in the northern hemisphere (Meinshausen et al., 2020). Therefore, the annual GHG concentrations for the northern hemisphere instead of global means (Meinshausen et al., 2020) are given as input to the WRF model, as shown in Figure 2.6.

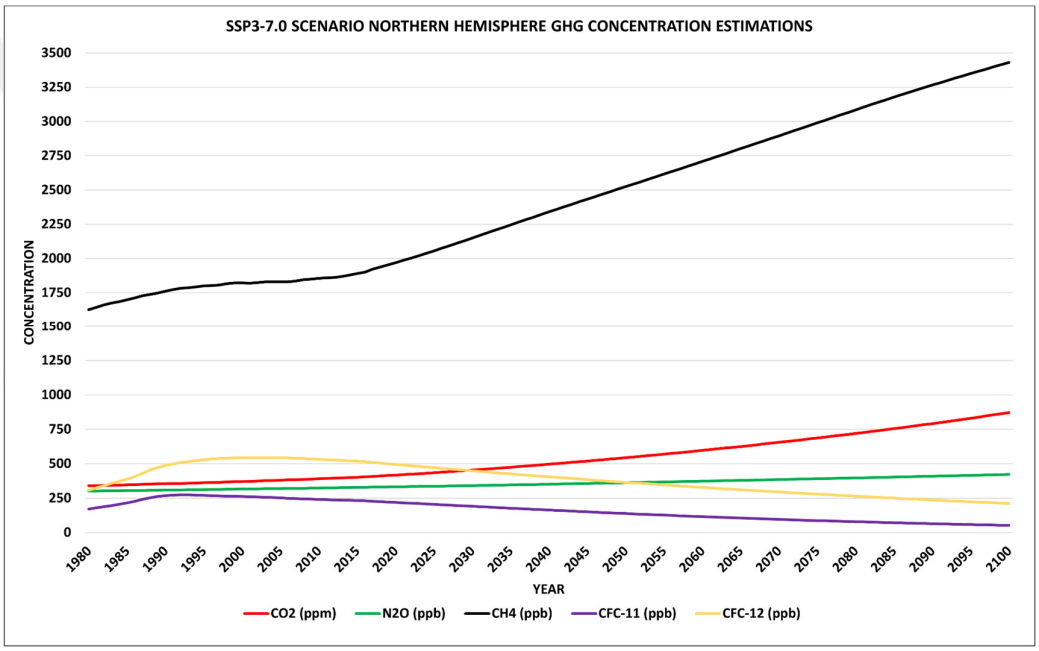

Figure 2.6 : The SSP3-7.0 scenario northern hemisphere GHG concentration estimations (Meinshausen et al., 2020).

2.4 Simulation Design

We downscaled MPI-ESM-HR outputs directly to 3 km horizontal resolution without an intermediate nest. In vertical model has 50 η levels with a top at 5000 Pa. The boundary conditions are relaxed exponentially in 10 grid points at the boundaries of the domain (relaxation zone). As for the integration timestep, we benefitted from the adaptive timestep capability of the WRF, letting the model set the maximum stable timestep, which is 24 seconds for our simulations. Additionally, we activated the vertical velocity damping option in the model affecting only strong updraft cores with locally high vertical velocities to keep the model stable (Skamarock et al. 2008).

Moreover, land-atmosphere interactions are essential in climate-scale simulations. Therefore, we used the 4-layer Noah land-surface model (Ek et al., 2003) with initial soil temperature and moisture conditions to represent land-atmosphere interactions in the simulations. The simulation outputs (hereafter WRFCP) at vertical model levels are saved at 6-hour intervals, and surface variables are saved at 1-hour interval.

2.4.1 Sensitivity tests and model parametrizations

In addition to dynamic calculations in the model, we used several parametrization options to represent the sub-grid scale processes. Howerver, before choosing the parametrization options for the simulations, we performed sensitivity tests to investigate the model response to microphysics and PBL schemes in extreme future conditions over the eastern Black Sea region. To this end, we perfomed 3-days-long simulations using different microphysics and PBL parametrization scheme combinations for cold and warm future cases based on the SSP5-8.5 scenario over the simulation domain of Doğan (2018). As the PBL options, we used Mellor-Yamada-Janjic (MYJ) and Yonsei University (YSU) PBL schemes, and for the microphysics, we used single-moment Kessler, Lin, WSM5, and double-moment Thompson, Morrison and WDM5 schemes.

First, we performed cold case simulations for 22-24 February 2050. Figure 2.7 shows the 3-day total precipitation amount in these simulations for different microphysics and PBL options. In the simulations, the 3-day total precipitation exceeds 100 mm over the Eastern Black Sea region of Turkey and locally reaches 175 mm for double-moment schemes such as the Morrison scheme. Among the simple moment schemes, the Kessler scheme produces the least precipitation since it does not account for ice microphysics related to snowfall.

Figure 2.8 shows the standart deviation of the 3-day total precipitation amounts for microphysics schemes in simulations with MYJ and YSU PBL schemes. For both PBL schemes, the precipitation amount differs mostly over the mountainous areas of the Eastern Black Sea region and a part of western Anatolia.

Figure 2.9 shows the 3-day total precipitation difference between the two PBL options for different microphysics options. The results show that the lowest difference between the two PBL schemes occurs in the simulations with Thompson and Morrison microphysics options.

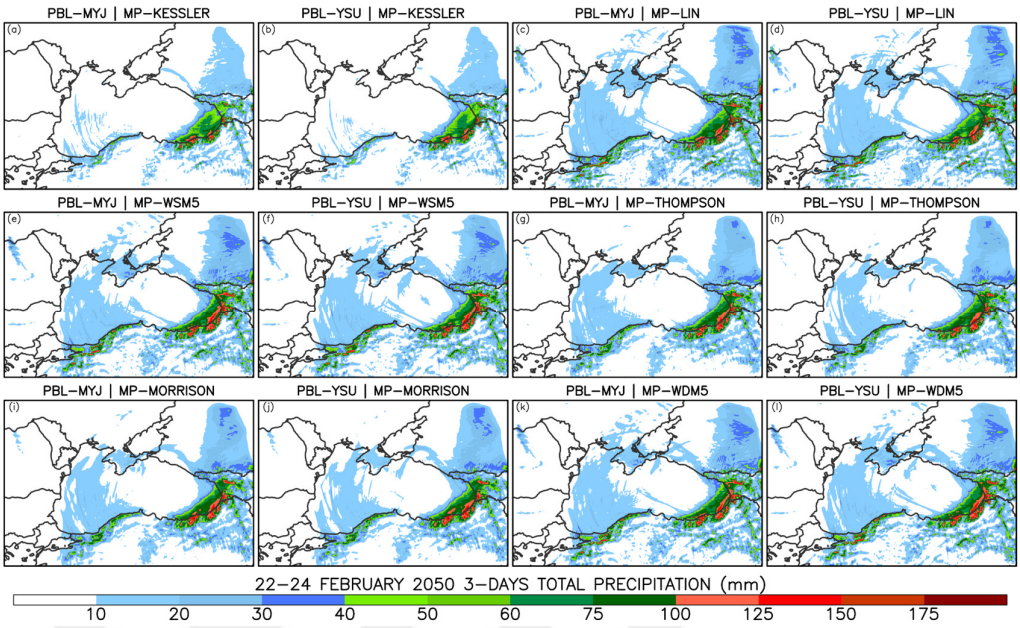

Figure 2.7 : The 3-days total precipitation amount for different microphysics and PBL schemes between 22-24 February 2050.

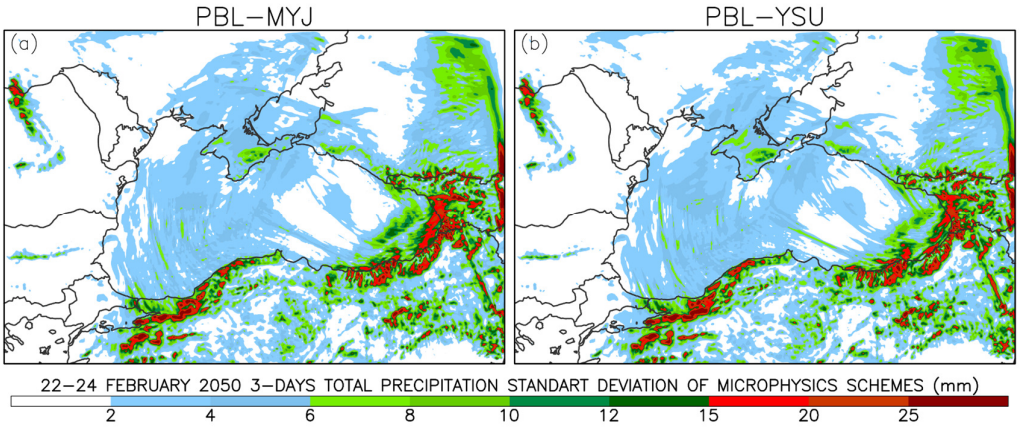

Figure 2.8 : The standard deviation of 3-days total precipitation between 22-24 February 2050 for different microphysics options.

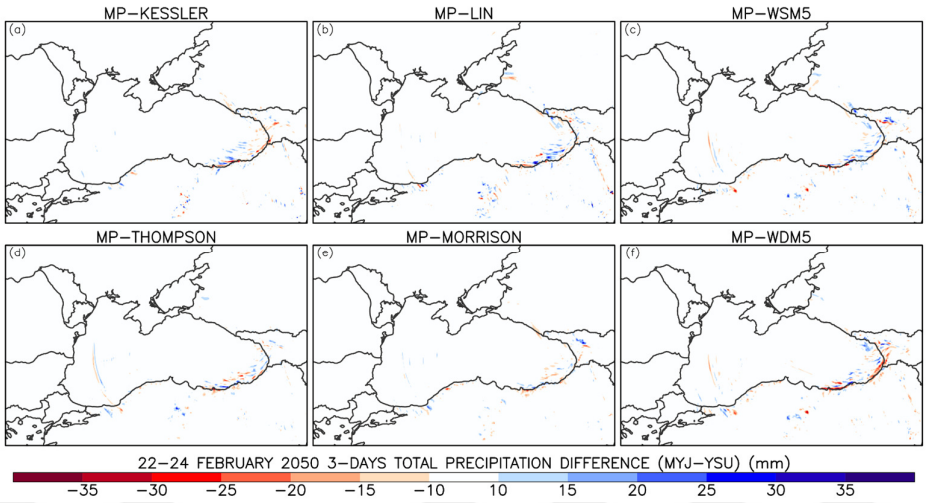

Figure 2.9 : The 3-days total precipitation difference of MYJ and YSU PBL schemes between 22-24 February 2050.

As another warm case study, we performed simulations for 3-5 October 2090. The 3-day total precipitation amount in the warm case simulations for different microphysics and PBL options are shown in Figure 2.10. In these simulations, the highest precipitation amount occurs over the Eastern Black Sea region, and 3-day totals locally exceed 500 mm in most simulations. According to the standard deviation of the precipitation amount for different microphysics, the MYJ PBL scheme results in a higher difference over this region, as shown in Figure 2.11. For the MYJ PBL option, the standard deviation reaches up to 100 mm.

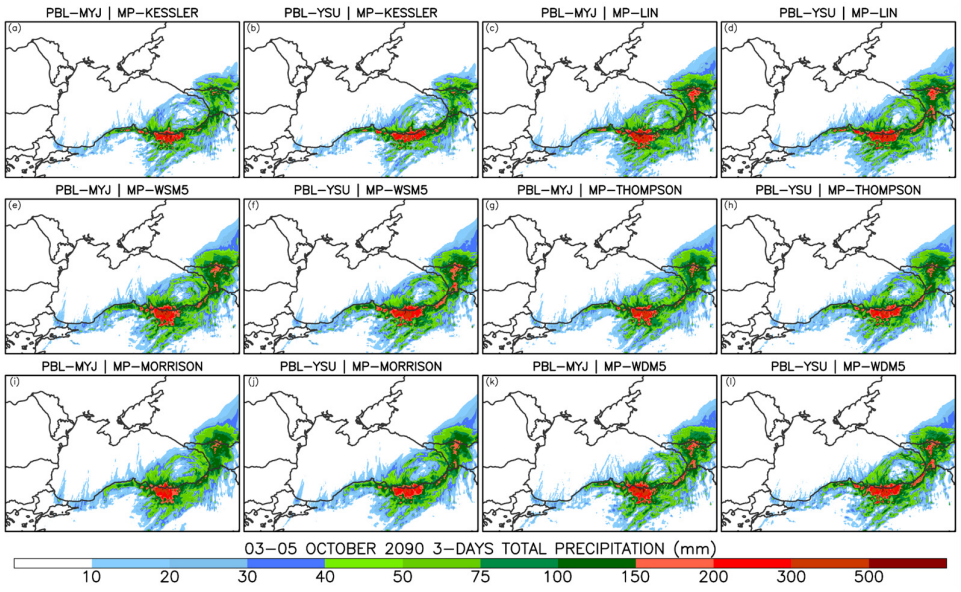

Figure 2.10 : The 3-days total precipitation amount for different microphysics and PBL schemes between 3-5 October 2090.

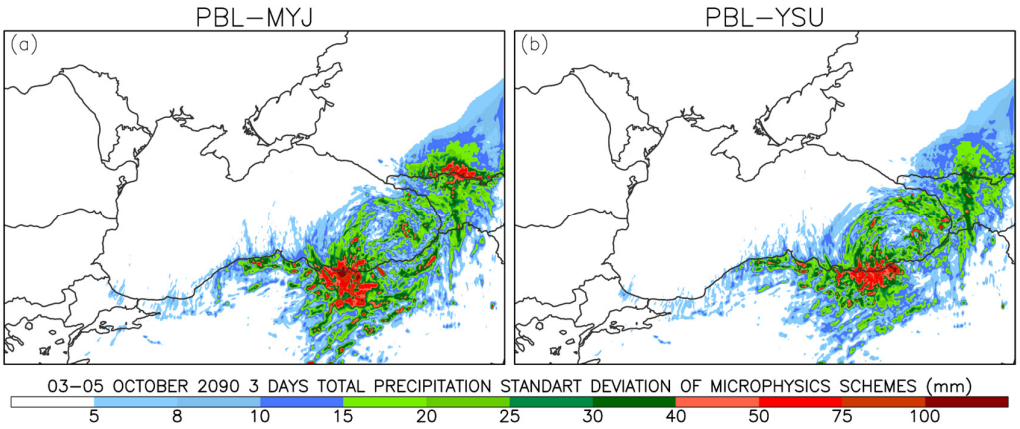

Figure 2.11 : The standard deviation of 3-days total precipitation between 3-5 October 2090 for different microphysics options.

In the warm case simulation, the choice of the PBL scheme affects the spatial distribution of precipitation amount. Figure 2.12 shows the 3-day total precipitation difference between MYJ and YSU PBL schemes for different microphysics options over the Eastern Black Sea. For all microphysics options, the YSU PBL scheme results in higher precipitation amounts on the eastern coast compared to the MYJ scheme.

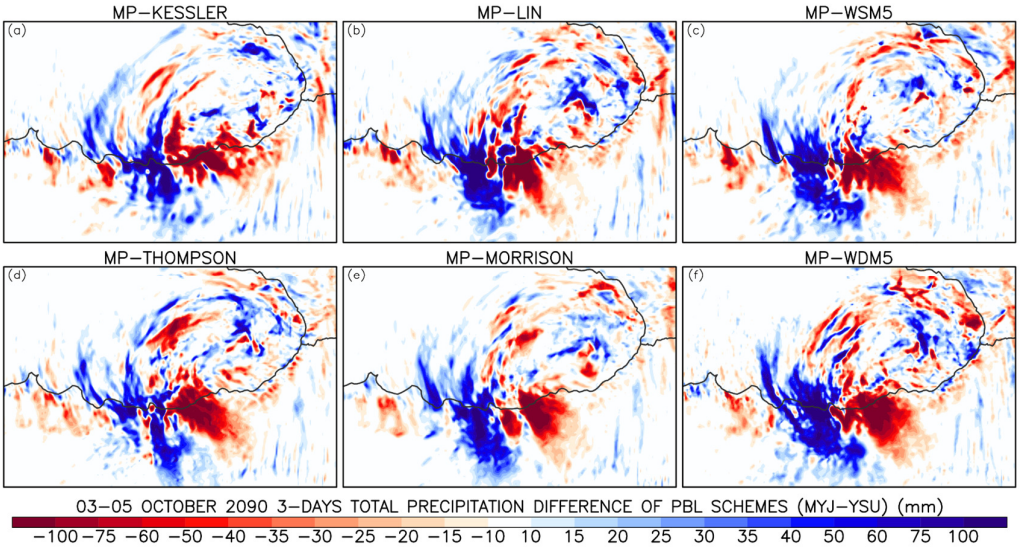

Figure 2.12 : The 3-days total precipitation difference of MYJ and YSU PBL schemes between 3-5 October 2090.

The difference between the MYJ and YSU PBL schemes can be related to the sea-atmosphere interactions that enhance precipitation. Figure 2.13 shows time – longitude Hovmöller diagram of upward moisture flux at the surface in the simulations for a cross-section taken over the Eastern Black Sea coast of Turkey. The results highlight

that the MYJ scheme results in higher moisture flux after the 36th hour of the case over the western side compared to the YSU scheme. This enhanced moisture flux in the MYJ scheme is due to the faster wind speeds in the simulations. Similar to Figure 2.13, Figure 2.14 shows 10m wind speeds in the simulations as a time – longitude Hovmöller diagram. The simulations using the YSU PBL scheme estimate slower wind speed over the west coast compared to the MYJ scheme and result in a less amount of upward moisture flux over the same region.

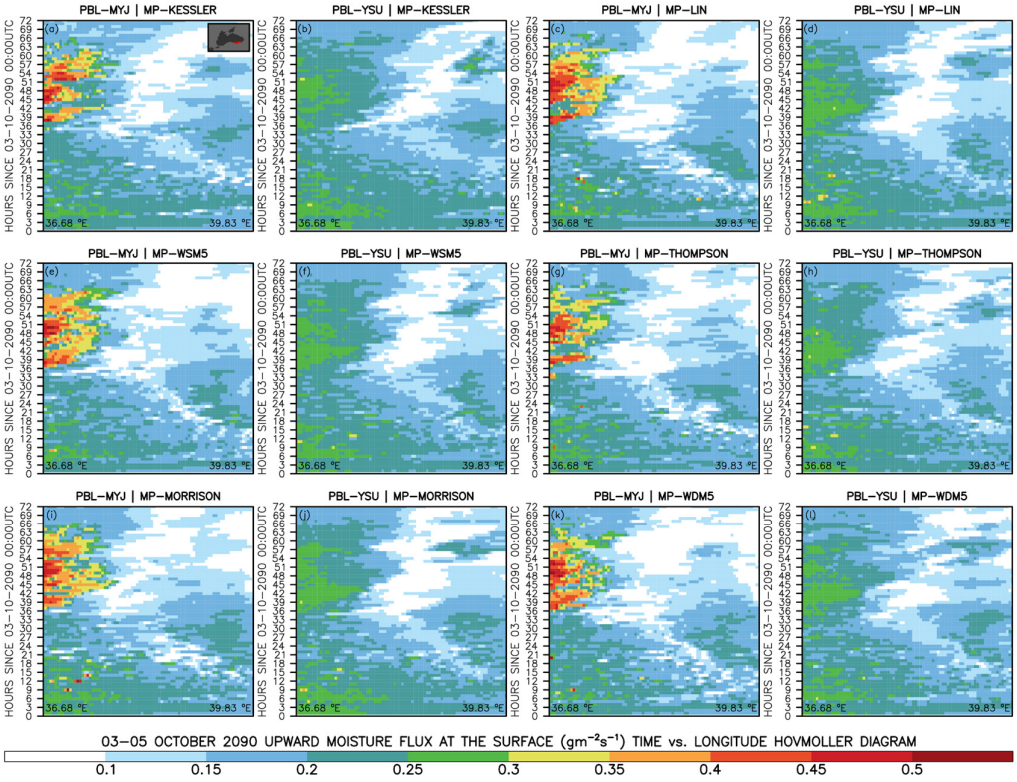

Figure 2.13 : The time – longitude Hovmöller diagram of upward moisture flux at the surface for different microphysics and PBL schemes between 3-5 October 2090.

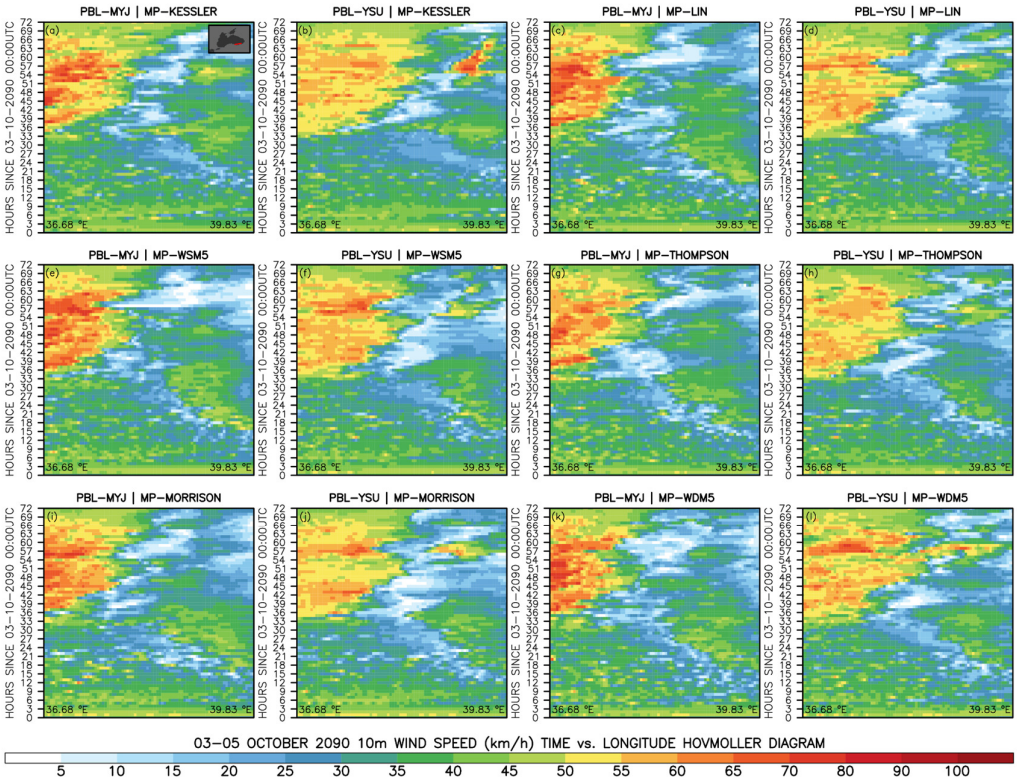

Figure 2.14 : The time – longitude Hovmöller diagram of 10m wind speed for different microphysics and PBL schemes between 3-5 October 2090.

As a result of the sensitivity analyses, the cold case simulations with the Thompson microphysics for different PBL schemes produce similar precipitation outputs. Similarly, the warm case simulations with the YSU PBL scheme for different microphysics options does not differ significantly. Therefore, in the climate simulations, for the microphysics, we used Thompson double-moment parametrization option (Thompson et al., 2008), which represents cloud, rain, ice, snow, and graupel processes and contains ice and rain number concentrations (Skamarock et al., 2008). As the parametrization of PBL processes, we used the non-local Yonsei University (Hong et al., 2006) parametrization option, in addition to the Monin-Obukhov Eta similarity surface layer scheme (Jiménez et al., 2012). For shortwave and longwave radiation physics, we used the RRTMG parametrization option (Iacono et al., 2008). On the other hand, most importantly, we switched off the deep and shallow cumulus (convective) parametrization schemes to let the model solve the convection explicitly as the purpose of a convection-permitting simulation.

2.5 Data

In order to run the WRF model, static topography and land use data are required. To this end, we used the Global Multi-resolution Terrain Elevation Data 2010 surface elevation data at 30-arc-second (~1 km) horizontal resolution (Danielson and Gesch, 2011) and Moderate Resolution Imaging Spectroradiometer International Geosphere-Biosphere Programme 21-class land use data (Skamarock et al., 2008) at ~500m resolution (Broxton et al., 2014). Land use over the simulation domain is shown in Figure 2.15.

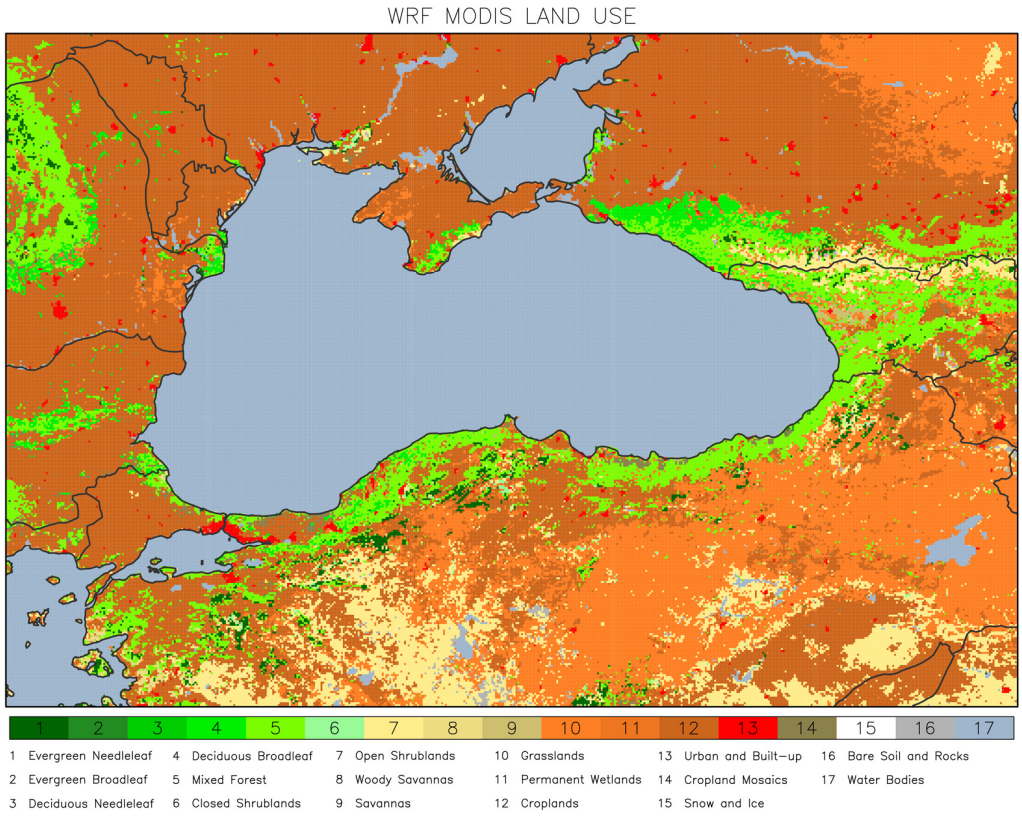

Figure 2.15 : The simulation domain land use classes.

For the model performance evaluation, we compared historical simulation outputs with high-resolution gridded observational and reanalysis datasets (hereafter reference datasets), summarized in Table 2.1. The Climate Hazards Group Infrared Precipitation with Stations (CHIRPS) is a daily precipitation dataset at 0.05-degree horizontal resolution and is produced using satellite imageries and station observations, spanning over the latitudinal band of 50°S-50°N (Funk et al., 2015). CHIRPS data is consistent with station observations over Turkey at the monthly time scale (Aksu and Akgül,

2020) and has been used for drought assessment over western Turkey (Aksu et al., 2022). Multi-Source Weighted-Ensemble Precipitation (MSWEP) version 2 gridded precipitation dataset at 0.1-degree horizontal resolution blends satellite data, reanalyses, and station observations to produce reliable global precipitation data at 3-hourly and daily intervals (Beck et al., 2019). Previously, this data has been used for extreme precipitation assessment over the Europe-Mediterranean region (Kelebek et al., 2021). ERA5-Land (ERA5LAND) (Muñoz Sabater, 2019) is a reanalysis dataset that replays the land component of the European Centre for Medium-Range Weather Forecasts ERA5 climate reanalysis, using the ERA5 atmospheric variables as input. It has a 0.1-degree horizontal resolution, which is higher than the one for ERA5 and applies a lapse rate correction between the grids of forcing data and the ERA5LAND (Url-1). In the study, we used hourly ERA5LAND data to calculate daily precipitation accumulations and daily minimum and maximum temperatures. TerraClimate (TERRACLIMATE) (Abatzoglou et al., 2018) is an observation-based monthly gridded temperature and precipitation dataset at ~4 km horizontal resolution and is produced by bilinearly interpolating the low spatial resolution monthly anomalies of Climate Research Unit time series data version 4.0 over the high spatial resolution climatology of WorldClim version 2 data (Abatzoglou et al., 2018). In the study, we used the minimum and maximum temperature fields of TERRACLIMATE.

Table 2.1 : The gridded dataset used in the analyses and their related information.

Dataset	Type	Horizontal Resolution	Variable
CHIRPS	Observational	0.05 degrees	Precipitation
MSWEP	Observations and reanalyses	0.1 degree	Precipitataion
ERA5LAND	Reanalyses	0.1 degree	Precipitaion and temperature
TERRACLIMATE	Observational	~4 km	Temperature

We also compared historical simulation outputs, MPI-ESM-HR outputs, and reference datasets using the Turkish State Meteorological Service (TSMS) station observations (37 stations in total) to validate the model results for temperature and precipitation. The list of the stations, their data coverage period and elevations are given in Table 2.2. The stations are mainly selected from high-elevation regions to evaluate the model performance over complex mountainous areas. For simplicity, we categorized the stations based on their elevations: E1 stations at an elevation between 0-1000 m (8 stations); E2 stations at an elevation between 1000-1500 m (9 stations); E3 stations at

an elevation between 1500-2000 m (12 stations); E4 stations at an elevation between 2000-2550 m (8 stations). The simulation outputs and reference data are bilinearly interpolated to the station coordinates. For the MPI-ESM-HR outputs, we used the nearest grid point to the station location.

Table 2.2 : The TSMS station IDs, elevations in metre, and data start and end years.

Station ID	Elevation (m)	Data Start Year	Data End Year
18584	2550	2014	2020
18715	2257	2016	2020
18732	2230	2016	2020
18149	2210	2013	2020
18730	2133	2016	2020
17692	2102	2005	2011
18174	2052	2014	2020
18378	2006	2014	2020
18525	1991	2014	2020
18674	1968	2016	2020
18376	1925	2014	2020
18904	1890	2014	2020
17676	1877	2005	2011
18177	1828	2014	2020
18194	1818	2014	2020
18349	1710	2014	2020
18669	1707	2016	2020
17786	1706	2005	2011
17840	1599	2005	2011
17688	1576	2005	2011
18707	1404	2016	2020
17713	1354	2010	2014
18179	1280	2013	2020
18075	1264	2013	2020
17747	1250	2005	2014
17018	1112	2005	2014
17756	1075	2005	2014
17846	1047	2005	2011
18518	1015	2014	2020
17808	993	2005	2011
18162	912	2013	2020
18135	900	2013	2020
18597	865	2015	2020
18511	750	2014	2020
18102	330	2013	2020
18437	139	2014	2020
17024	64	2005	2014

Furthermore, since the BSA is a broad region with complex topographical features, in addition to domain-wide analyses, we performed subregional analyses. To this end, we defined 36 subregions based on the Nomenclature of Territorial Units for Statistics statistical regions of the statistical office of the European Union (European Commission. Statistical Office of the European Union., 2022) and Global Runoff Data Centre's (GRDC) major river basins (GRDC, 2022). The borders of the subregions with their related name abbreviation along with the TSMS station locations are given in Figure 2.16. It should be noted that the relaxation grids at the boundaries of the simulation domain are not included in the subregional analyses to avoid unrealistic temperature and precipitation values.

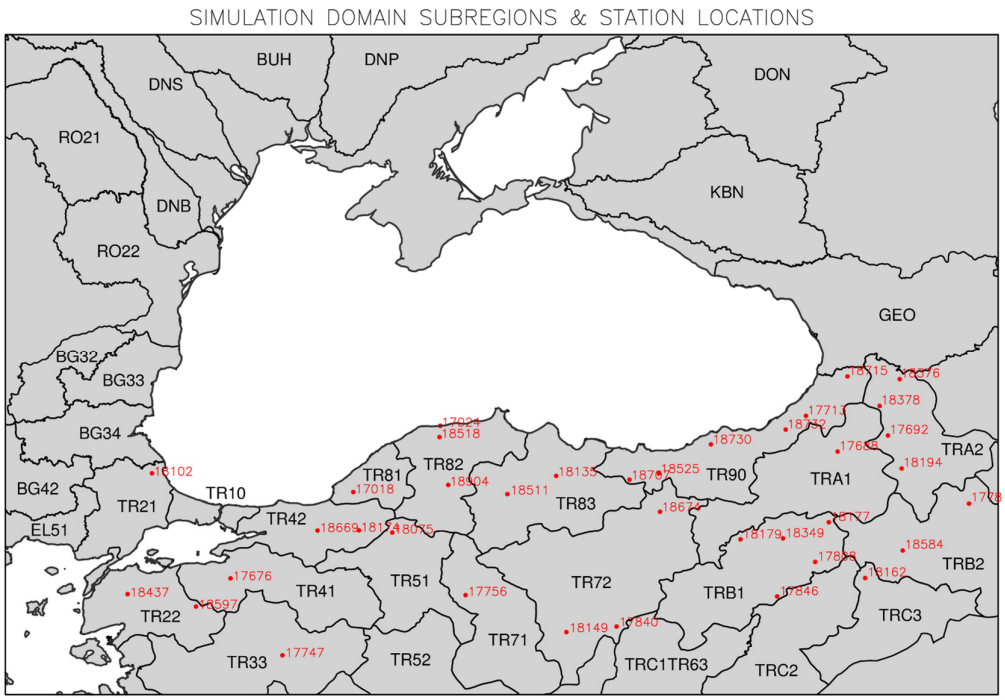

Figure 2.16 : The BSA subregions with the name abbreviations (black) and the TSMS station locations (red).

3. EVALUATION OF HISTORICAL SIMULATION

In this section, we analysed historical simulation outputs for maximum and minimum temperature and precipitation between 2005-2014 to evaluate the model performance. To this end, we compared model outputs with reference datasets and station observations.

3.1 Evaluation of Temperature

The seasonal means of daily maximum (Tmax) and minimum (Tmin) 2m air temperatures of MPI-ESM-HR, WRFCP, TERRACLIMATE and ERA5LAND are given in Figure 3.1 and Figure 3.2, respectively. WRFCP represents the spatial distribution of temperature values satisfactorily over the study area. It gives closer results to the reference data and provides more detail compared to lower resolution MPI-ESM-HR over the complex mountainous areas such as the Caucasus and Eastern Anatolia, indicating the added value of WRFCP.

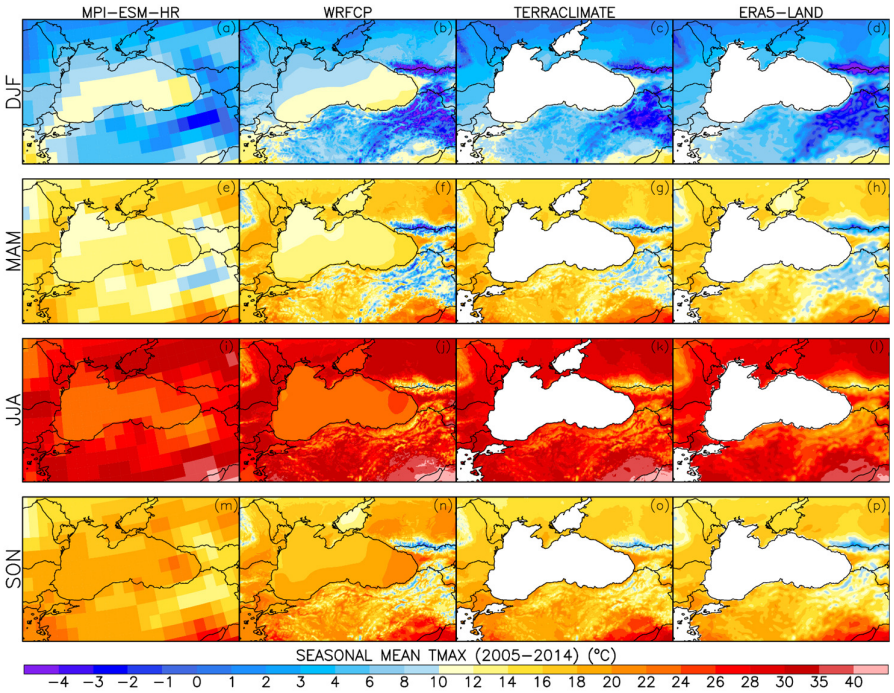

Figure 3.1 : The seasonal mean Tmax of each dataset between 2005-2014.

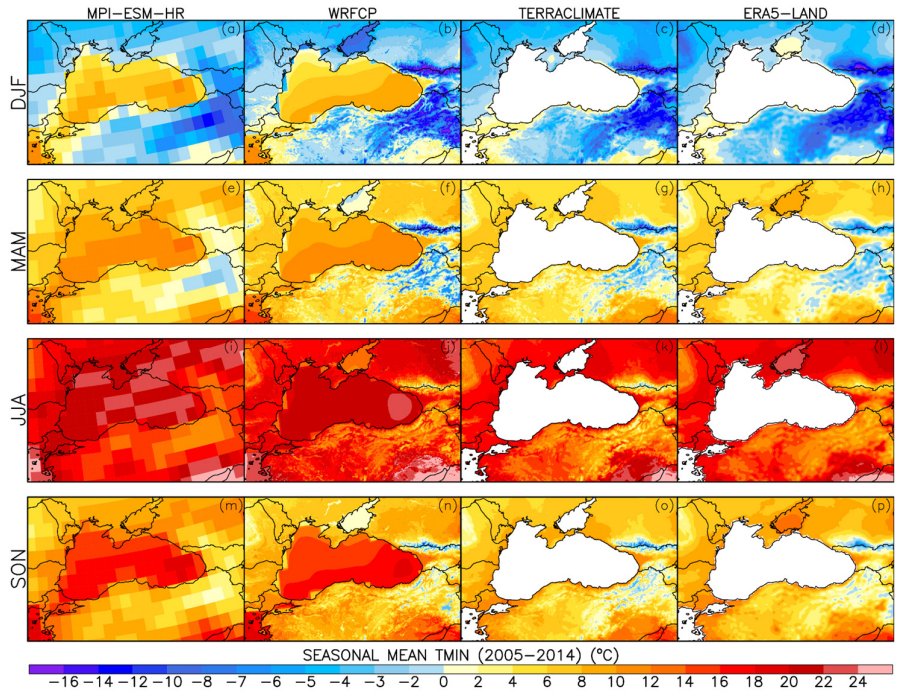

Figure 3.2 : The seasonal mean Tmin of each dataset between 2005-2014.

As a quantitative assessment, we calculated the root mean squared error (RMSE) of WRFCP with respect to (w.r.t.) TERRACLIMATE and ERA5LAND over the study area and showed the results in Table 3.1. For the Tmax, WRFCP has a lower RMSE for the comparison with TERRACLIMATE than for the ERA5LAND. The maximum RMSE for TERRACLIMATE is 1.90°C in autumn, and for ERA5LAND is 2.63°C in summer. For the Tmin, WRFCP has a higher RMSE w.r.t. ERA5LAND for all seasons except summer. The maximum RMSE w.r.t. TERRACLIMATE is 2.50°C in summer and 2.38°C w.r.t. ERA5LAND in winter.

Table 3.1 : The seasonal mean Tmax and Tmin RMSE w.r.t. TERRACLIMATE and ERA5LAND.

	DJF RMSE (°C)	MAM RMSE (°C)	JJA RMSE (°C)	SON RMSE (°C)
Tmax WRFCP-TERRACLIMATE	1.79	1.65	1.71	1.90
Tmax WRFCP-ERA5LAND	1.81	1.90	2.63	2.33
Tmin WRFCP-TERRACLIMATE	1.68	1.27	2.50	1.83
Tmin WRFCP-ERA5LAND	2.38	1.89	2.16	1.94

Moreover, seasonal biases of Tmax are given in Figure 3.3. The choice of observational or reanalysis data for temperature bias calculations resulted in differences. In terms of maximum temperature, WRFCP has negative biases of around

2°C and 4°C in winter and spring, respectively, compared to TERRACLIMATE over the Anatolian Peninsula and the Caucasus. In comparison to ERA5LAND, WRFCP bias becomes positive over most of this area and is around 3°C. Similarly, in the autumn, the model has a positive bias around 3°C compared to ERA5LAND. This bias reduces to 1°C for TERRACLIMATE and even becomes negative over Eastern Anatolia. Most significantly, in the summer, while WRFCP has a negative bias of about 3°C compared to TERRACLIMATE over the mountains of the Eastern Black Sea region of Turkey, there is no significant difference between WRFCP and ERA5LAND over the same region. These differences may be related to the different production methods of the reference data. TERRACLIMATE uses observational data to produce high-resolution temperature information (Abatzoglou et al., 2018), while the ERA5LAND is a reanalysis based on a dynamic model (Muñoz Sabater, 2019). The representation of clouds in the models affects and decreases the near-surface air temperature. TERRACLIMATE does not include cloud information, and observational deficiencies in data-sparse regions can lead to errors in the production of this data which employs simple bilinear interpolation (Abatzoglou et al., 2018). Therefore, the different biases of WRFCP between TERRACLIMATE and ERA5LAND can be explained by cloud dynamics which affect the surface radiation budget.

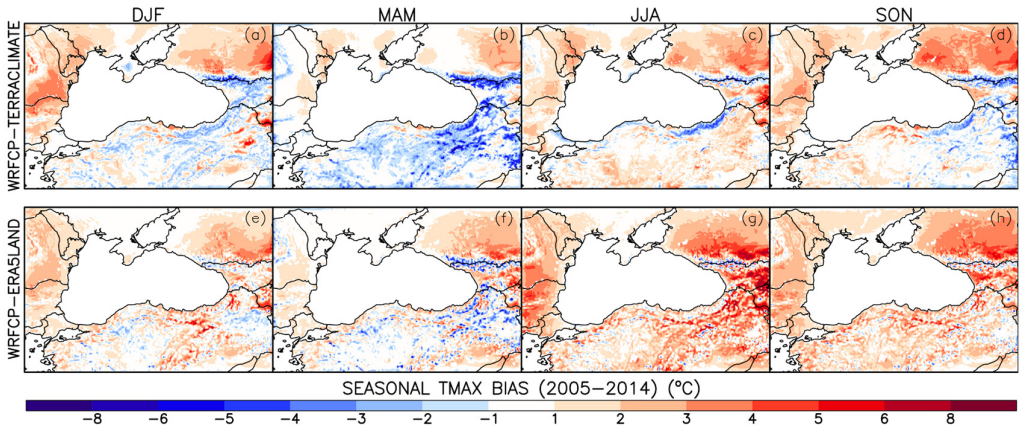

Figure 3.3 : The seasonal Tmax biases w.r.t TERRACLIMATE (a-d) and ERA5LAND (e-h).

Figure 3.4 shows the seasonal biases of Tmin. Compared to both TERRACLIMATE and ERA5LAND, in winter, WRFCP has a positive bias of about 2°C and 4°C, respectively. In spring, the model has a negative bias of around 3°C over Eastern

Anatolia, comparing both data. The positive bias over other regions is around 2°C. The highest difference between WRFCP and the reference datasets is in the summer months. In summer, WRFCP has a positive bias reaching up to 5°C across the Anatolian Peninsula. The model also exhibits significant positive bias in the autumn months, which is around 4°C over the study area.

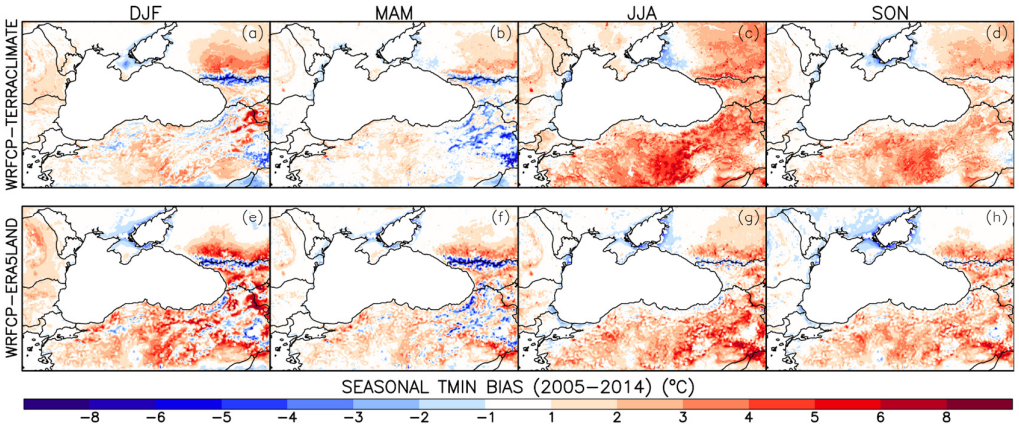

Figure 3.4 : The seasonal Tmin biases w.r.t TERRACLIMATE (a-d) and ERA5LAND (e-h).

3.1.1 Station-based temperature analyses

Reanalysis and observational gridded data are partly based on station observations, and low-density station network at higher elevations increases the observational uncertainty over these areas (Önol and Semazzi, 2009; Önol, 2012). Therefore, we also compared monthly mean Tmax and Tmin at TSMS station points. In general, WRFCP outputs are closer to the station observations compared to MPI-ESM-HR outputs. Figure 3.5 and Figure 3.6 show monthly mean Tmax of each dataset for E4 and E3 high-elevation stations above 2000 m and between 1500-2000 m, respectively. In most stations, WRFCP better captures the annual cycle compared to MPI-ESM-HR and is closer to the observations. Nevertheless, in some stations, for example, 18149 and 18174 E4 stations and 18904 E3 station, WRFCP has a negative bias in winter and spring and a positive bias in summer. However, this bias is much lower compared to MPI-ESM-HR and indicates the added value of WRFCP.

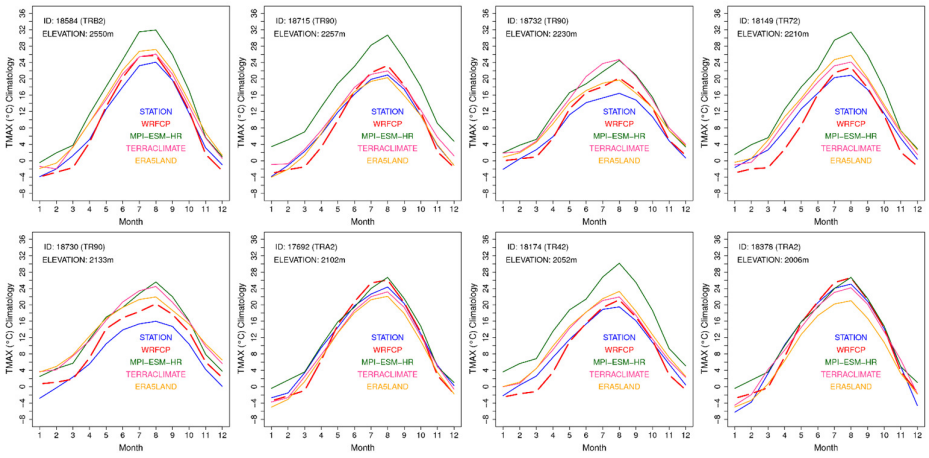

Figure 3.5 : The monthly mean Tmax of each dataset at the TSMS stations for E4 elevation category.

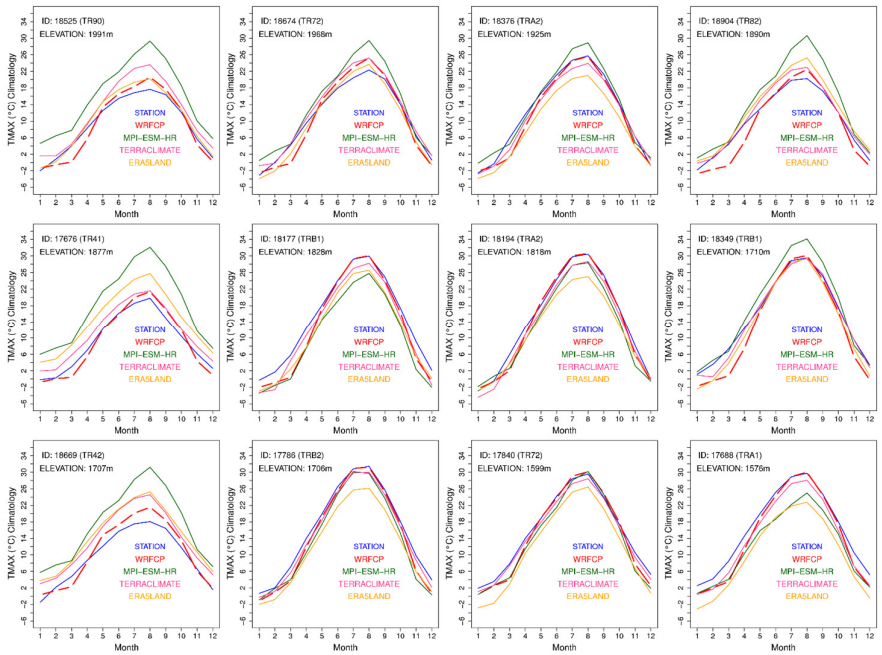

Figure 3.6 : The monthly mean Tmax of each dataset at the TSMS stations for E3 elevation category.

For E2 stations between 1000-1500 m elevation, as shown in Figure 3.7, WRFCP generally agrees with the observations, but similar to the E4 and E3 stations, it has a negative bias in winter and spring for numerous stations such as 17756 and 18518. Still, in most stations, it is closer to the observations compared to MPI-ESM-HR. For the low elevation E1 stations from 0 to 1000 m, as in Figure 3.8, in most stations, there

is no significant difference between WRFCP and the observations, and WRFCP is closer to the observations than the MPI-ESM-HR outputs.

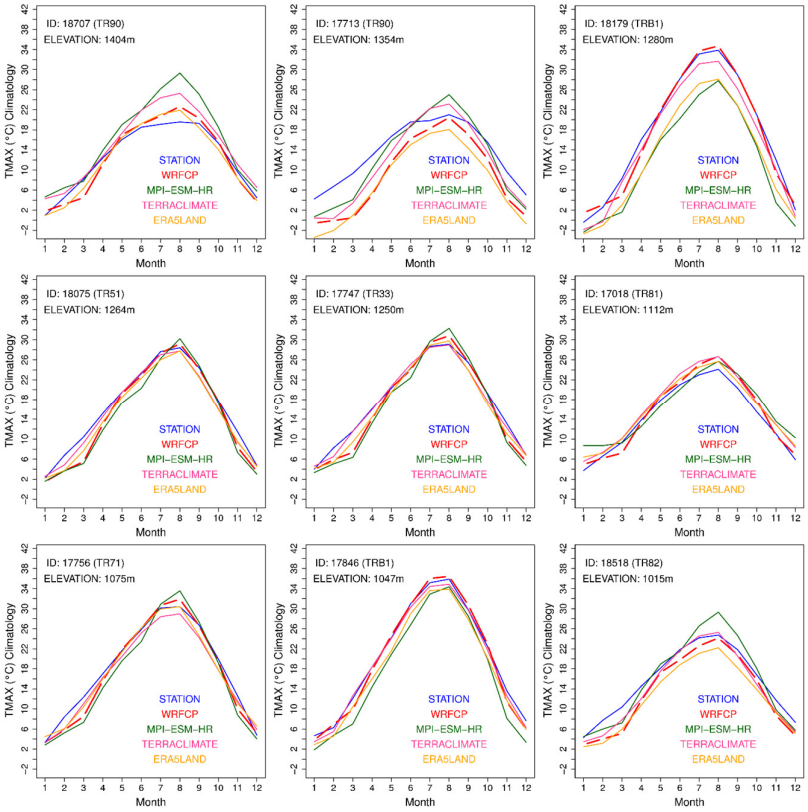

Figure 3.7 : The monthly mean Tmax of each dataset at the TSMS stations for E2 elevation category.

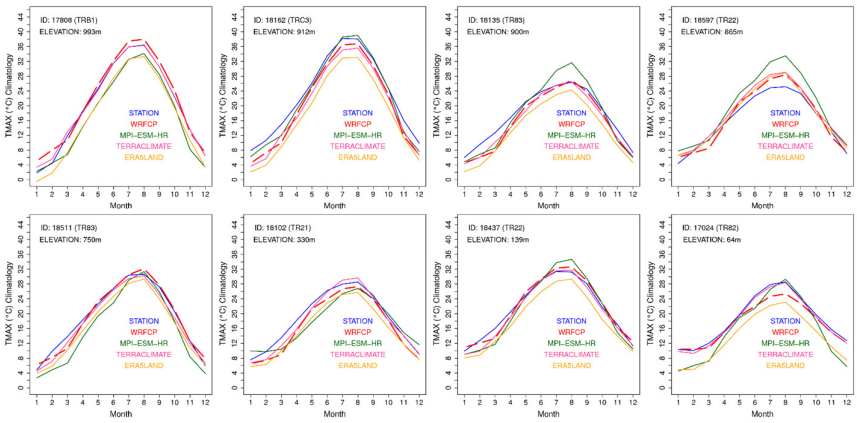

Figure 3.8 : The monthly mean Tmax of each dataset at the TSMS stations for E1 elevation category.

The RMSE of monthly mean Tmax for WRFCP, MPI-ESM-HR, and reference datasets comparing with the station observations are given in Table 3.2. In 32 out of

37 stations, WRFCP has a lower RMSE compared to MPI-ESM-HR. Moreover, in 8 stations, WRFCP has the lowest RMSE among all datasets.

Table 3.2 : The monthly mean Tmax RMSE for each dataset at the selected TSMS station observation points.

Station ID	WRFCP RMSE (°C)	MPIESMHR RMSE (°C)	TERRACLIMATE RMSE (°C)	ERA5LAND RMSE (°C)
18584	1.53	5.45	2.34	3
18715	1.9	7	1.51	0.71
18732	2.01	4.94	5.06	2.72
18149	2.63	6.01	1.99	2.96
18730	2.77	5.99	6.24	5.8
17692	2.07	1.59	1.04	1.96
18174	1.93	6.89	1.93	2.45
18378	2.11	2.88	1.46	3.08
18525	1.86	6.98	3.29	1.44
18674	2.17	3.57	1.88	1.38
18376	1.84	1.87	1.47	3.61
18904	2.41	5.08	1.61	2.66
17676	1.51	8.88	2.14	5.09
18177	2.69	4.67	2.48	3.39
18194	1.47	2.66	1.63	3.48
18349	3.21	2.53	1.16	2.28
18669	1.96	8.07	4.22	4.92
17786	1.97	2.8	1.31	4.19
17840	1.79	2.32	0.95	3.93
17688	2.36	4.32	2.29	5.97
18707	1.71	4.38	2.88	1.38
17713	5.1	3.04	3.52	6.17
18179	1.64	6.19	1.94	5.17
18075	2.07	2.72	1.17	1.72
17747	1.89	2.6	0.9	1.55
17018	1.64	2.61	1.9	1.6
17756	1.66	2.59	1.54	1.48
17846	1.18	3.48	0.81	2
18518	2.55	2.18	1.79	3.21
17808	1.73	3.53	0.59	3.41
18162	2.86	1.68	3.24	5.42
18135	2.21	2.7	2	3.93
18597	1.74	4.34	2.18	1.73
18511	1.38	3.69	1.32	2.53
18102	2.12	2.93	1.31	3.09
18437	1.22	2.22	1.25	3.07
17024	1.69	3.84	0.55	4.86

The monthly mean Tmin of E4 and E3 stations are shown in Figure 3.9 and Figure 3.10, respectively. Similar to the Tmax, WRFCP captures the annual cycle and corrects MPI-ESM-HR outputs significantly in most stations but has a negative bias in winter and spring for numerous high-elevation stations, such as 18584 and 18732 E4 stations, and 18525 and 18674 E3 stations. Besides, WRFCP has a positive bias in some stations in summer but the difference between the observations is lower compared to MPI-ESM-HR.

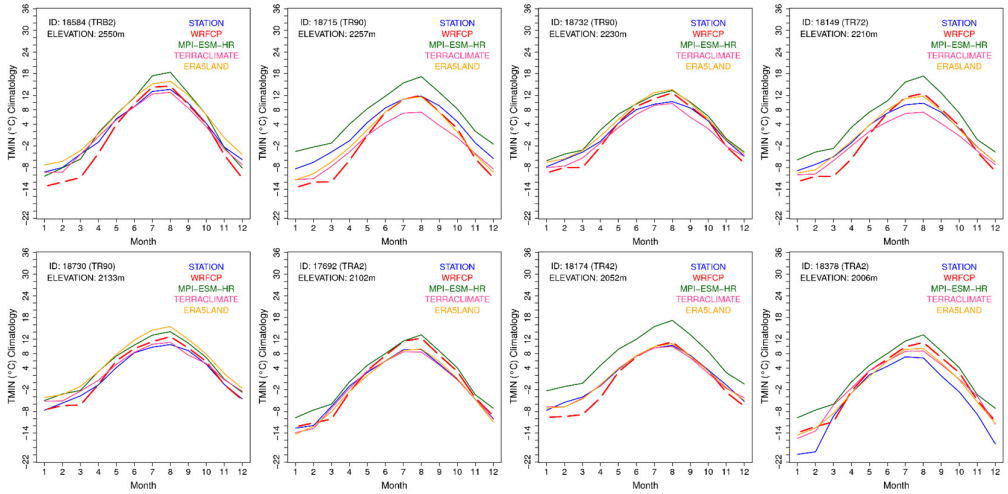

Figure 3.9 : The monthly mean Tmin of each dataset at the TSMS stations for E4 elevation category.

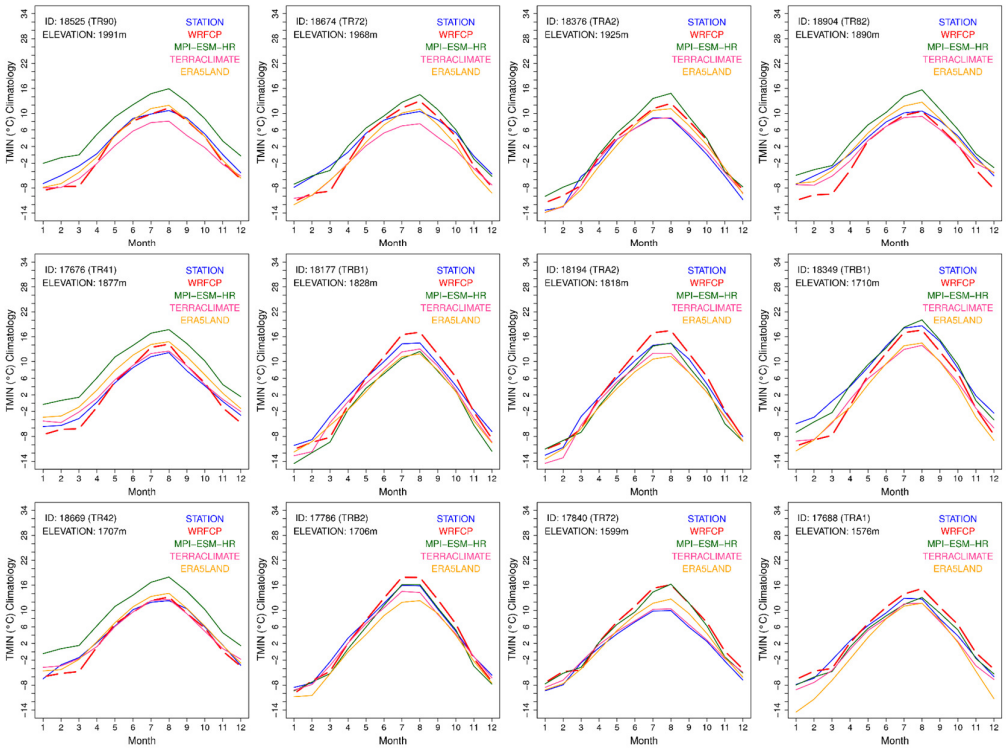

Figure 3.10 : The monthly mean Tmin of each dataset at the TSMS stations for E3 elevation category.

The monthly mean Tmin for E2 and E1 stations are shown in Figure 3.11 and Figure 3.12, respectively. At these lower elevation stations, WRFCP has a lower bias compared to E4 and E3 stations and follows the annual cycle of observations. In comparison with MPI-ESM-HR, WRFCP provides better estimations in most stations, particularly in 17018 E2 and 18102 E1 stations.

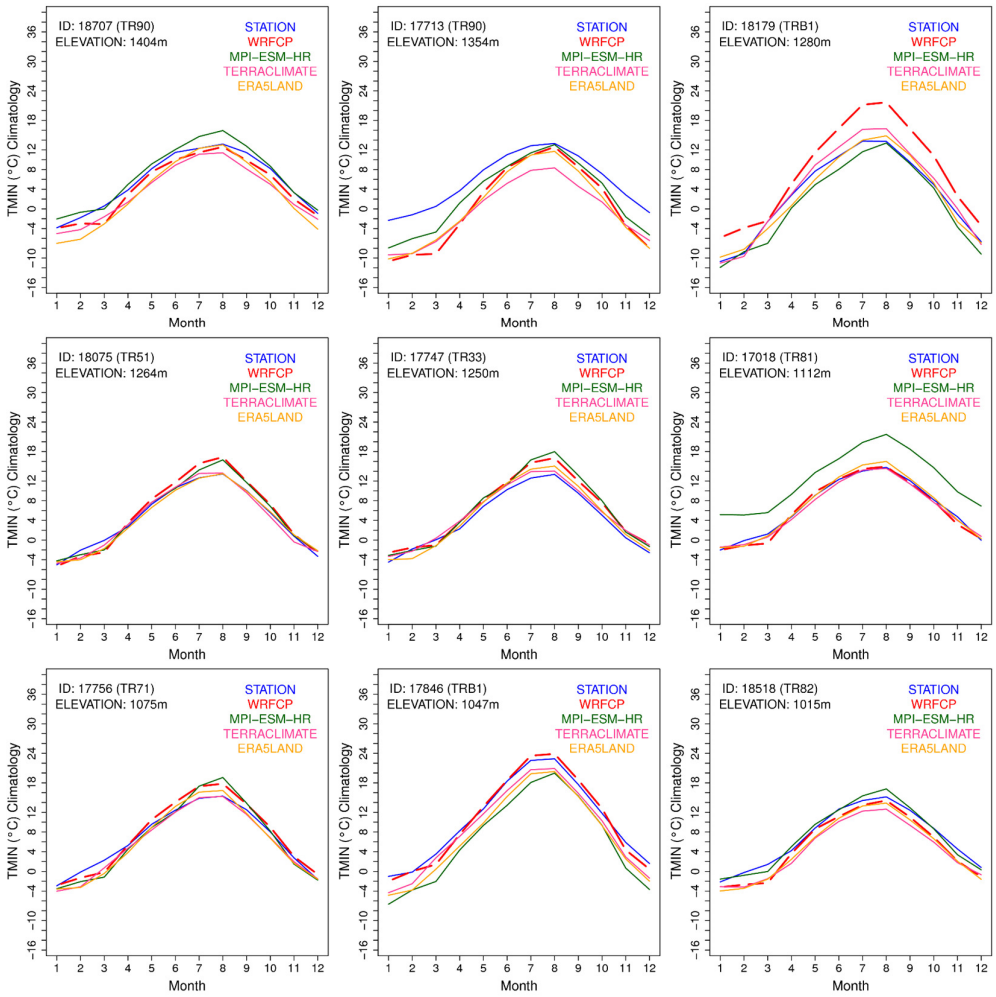

Figure 3.11 : The monthly mean Tmin of each dataset at the TSMS stations for E2 elevation category.

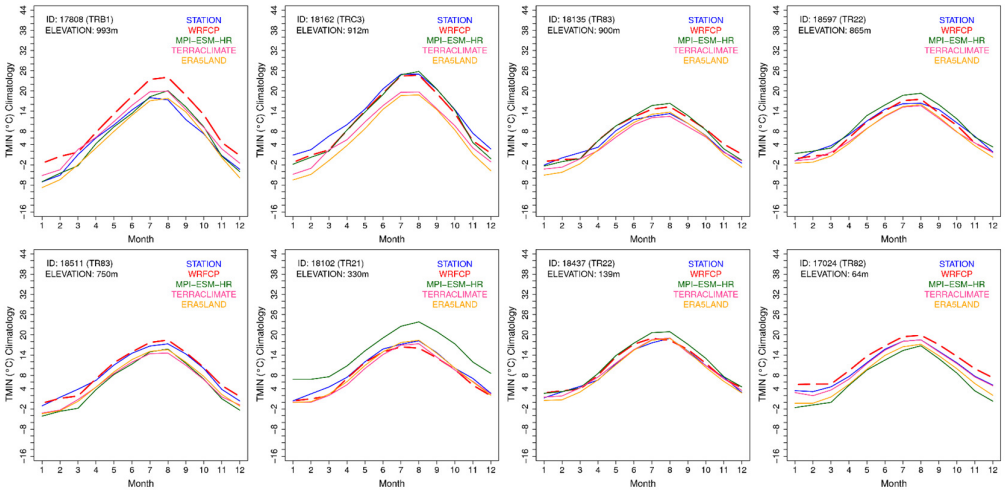

Figure 3.12 : The monthly mean Tmin of each dataset at the TSMS stations for E1 elevation category.

The RMSE of monthly mean Tmin for WRFCP, MPI-ESM-HR, and reference datasets comparing with the station observations are given in Table 3.3. In 23 stations, WRFCP has a lower RMSE compared to MPI-ESM-HR. Furthermore, in 5 stations, WRFCP has the lowest RMSE among all datasets.

These results highlight the superior performance of a high-resolution CPM compared to a low-resolution GCM over the complex topography in terms of the representation of mean temperature.

Table 3.3 : The monthly mean Tmin RMSE for each dataset at the selected TSMS station observation points.

Station ID	WRFCP RMSE (°C)	MPIESMHR RMSE (°C)	TERRACLIMATE RMSE (°C)	ERA5LAND RMSE (°C)
18584	3.17	2.55	0.94	2.05
18715	4.31	4.03	3.93	2.46
18732	1.91	1.94	1.4	1.63
18149	2.85	4.32	1.97	0.95
18730	1.29	2.61	1.28	3.5
17692	1.93	2.77	0.58	0.89
18174	2.26	5.2	0.72	0.54
18378	4.36	6.81	3.55	3.58
18525	1.96	4.17	2.68	1.12
18674	2.84	1.81	3.33	3.04
18376	2.43	3.58	0.95	1.81
18904	3.18	2.66	1.58	1.06
17676	1.56	5.56	0.9	2.66
18177	2.18	3.54	1.82	2.43
18194	1.81	1.88	1.95	2.36
18349	4.1	1.32	4.23	5.05
18669	1.35	4.4	1.1	0.99
17786	1.56	1.53	0.98	2.71
17840	3.83	3.38	0.8	1.66
17688	1.79	1.22	1.47	3.75
18707	1.47	1.39	2.35	2.77
17713	5.85	3.51	6.24	5.66
18179	5.2	2.26	1.41	1.19
18075	1.78	1.36	0.82	0.88
17747	2.03	2.39	1.06	1.22
17018	0.84	5.74	0.62	0.69
17756	1.49	1.85	1.2	1.5
17846	1.07	4.3	2.12	3.1
18518	1.83	0.88	2.47	2.15
17808	4.85	1.87	1.84	1.86
18162	1.8	2.15	4.88	6.47
18135	1.8	1.84	1.36	1.9
18597	1.22	1.6	1.88	2.21
18511	0.97	3.19	2.69	2.37
18102	1.37	5.09	1.53	1.13
18437	1.19	1.83	0.59	0.98
17024	1.78	3.54	0.55	2.42

3.2 Evaluation of Precipitation

The annual mean total precipitation of MPI-ESM-HR, WRFCP, and the reference data are given in Figure 3.13. In terms of the spatial distribution of the total precipitation amount, WRFCP agrees with reference datasets over a broad part of the simulation domain. Nevertheless, the model has a positive bias over the Western and Eastern Black Sea regions of Turkey and mountainous areas such as the Caucasus.

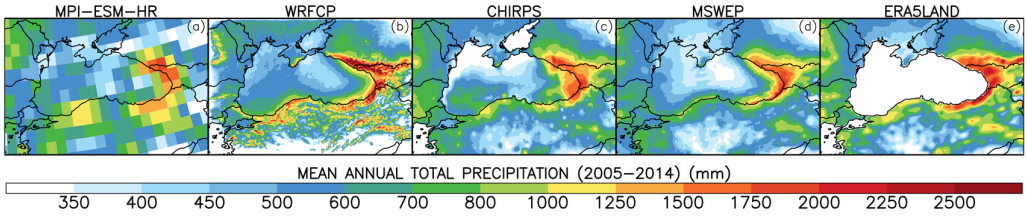

Figure 3.13 : The mean annual total precipitation of each dataset between 2005-2014.

Moreover, we showed the seasonal means of total precipitation in Figure 3.14. WRFCP captures spatial distribution of the precipitation amount satisfactorily in all seasons except for the winter. We calculated RMSE between WRFCP-CHIRPS, WRFCP-MSWEP, and WRFCP-ERA5LAND over the domain and found the highest (around 165 mm) and the lowest (around 67 mm) errors occur in the winter and autumn months, respectively, as shown in Table 3.4.

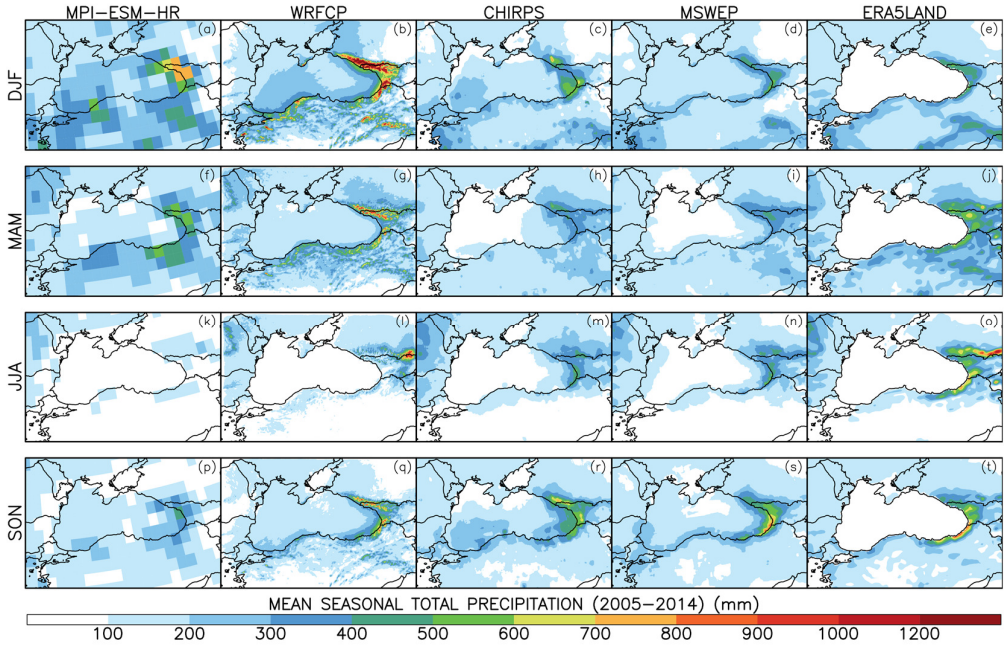

Figure 3.14 : The seasonal mean of total precipitation for each dataset between 2005-2014.

Table 3.4 : The WRFCP seasonal total precipitation RMSE w.r.t. CHIRPS, MSWEP, and ERA5LAND.

	DJF RMSE (mm)	MAM RMSE (mm)	JJA RMSE (mm)	SON RMSE (mm)
WRFCP-CHIRPS	164.77	101.93	80.47	68.01
WRFCP-MSWEP	167.91	100.81	72.47	67.65
WRFCP-ERA5LAND	156.83	92.62	101.45	78.3

Additionally, we calculated the seasonal total precipitation bias of WRFCP at each grid point to reveal the region in which and how much the model most differed from the reference datasets and showed the results in Figure 3.15. The highest difference occurs in the winter months, especially over the mountainous areas of the Anatolian Peninsula and the Eastern Black Sea region. Model bias is around 6 mm/day over the mountains and, in particular, reaches up to 15 mm/day over the Caucasus.

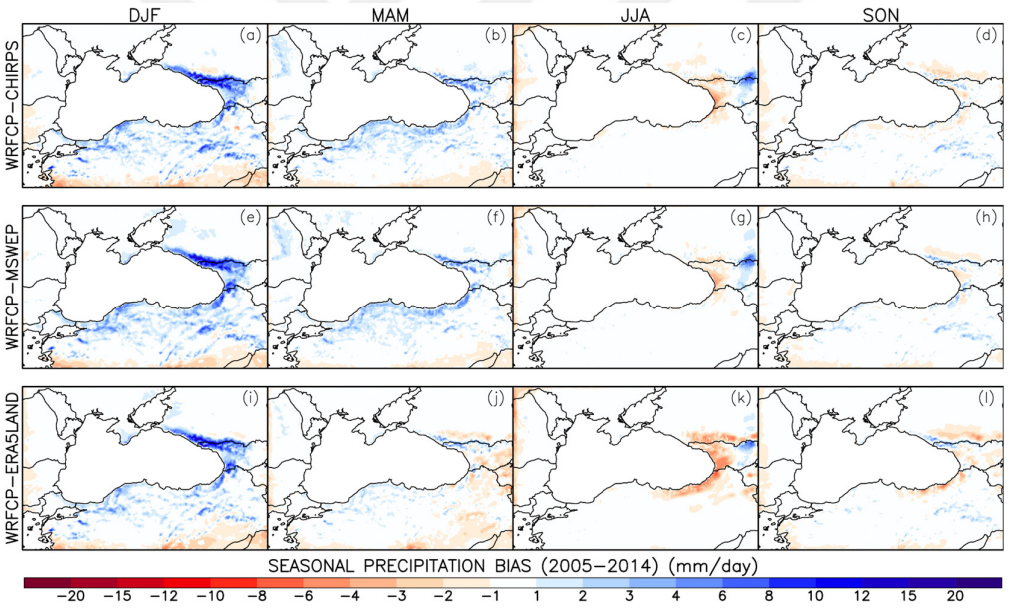

Figure 3.15 : The seasonal precipitation bias w.r.t CHIRPS (a-d), MSWEP (e-h), and ERA5LAND (i-l).

The bias of the WRFCP can be explained by the driving boundary conditions coming from MPI-ESM-HR. We found that, in the winter, MPI-ESM-HR produces more precipitation by 200-400 mm over the Western Black Sea region, parts of Eastern Anatolia, and the Caucasus Mountains. These indicate that the WRFCP bias over these regions is a direct consequence of the boundary conditions on the regional climate simulation. A similar issue occurs in the summer months when MPI-ESM-HR produces less precipitation over the Eastern Black Sea region compared to the reference datasets. During these months, WRFCP has a negative bias of around 4

mm/day compared to CHIRPS and MSWEP observations and 6 mm/day compared to ERA5LAND reanalysis over this region. In the spring months, the difference is lower compared to the winter and summer months, which becomes a maximum of about 8 mm/day over the Caucasus and does not become more than 6 mm/day in other regions. Additionally, in spring, WRFCP has a lower bias for ERA5LAND compared to CHIRPS and MSWEP in magnitude over the Black Sea coast of Turkey. These bias differences in summer and spring due to different datasets highlight the inconsistencies among the reference data.

3.2.1 Station-based seasonal precipitation analyses

Given inconsistencies among the reference data, we compared monthly mean total precipitations at TSMS station points. In general, WRFCP captures the annual cycle of monthly total precipitation but has a bias. Figure 3.16 shows monthly total precipitation climatologies for each dataset at E4 station points. At high-elevation stations above 2000 m, WRFCP has a positive bias, especially in winter months, compared to station observations and reference datasets. For a part of the stations, for example, 18715 and 18174 stations, the bias is due to the positive bias MPI-ESM-HR.

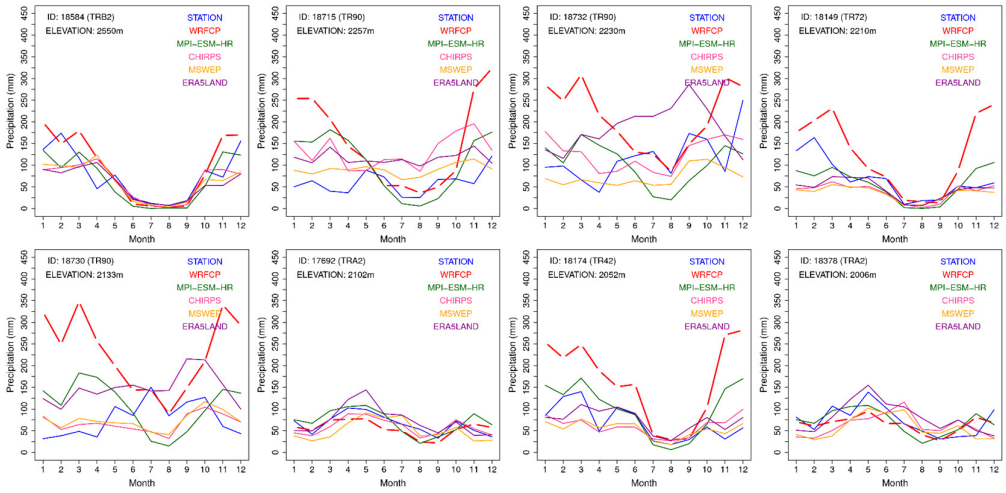

Figure 3.16 : The monthly mean total precipitation for each dataset at the TSMS stations for E4 elevation category.

Similar to the E4 station points, at E3 stations between 1500-2000 m elevation, the WRFCP has a positive bias of monthly precipitation totals in winter and spring months for most stations, as shown in Figure 3.17. Still, the WRFCP corrects MPI-ESM-HR outputs in summer for 18525 station, and in spring, summer, and autumn for 18376

and 17688 stations. For 18194, 17786, and 17840 stations, both MPI-ESM-HR and WRFCP agree with the station observations.

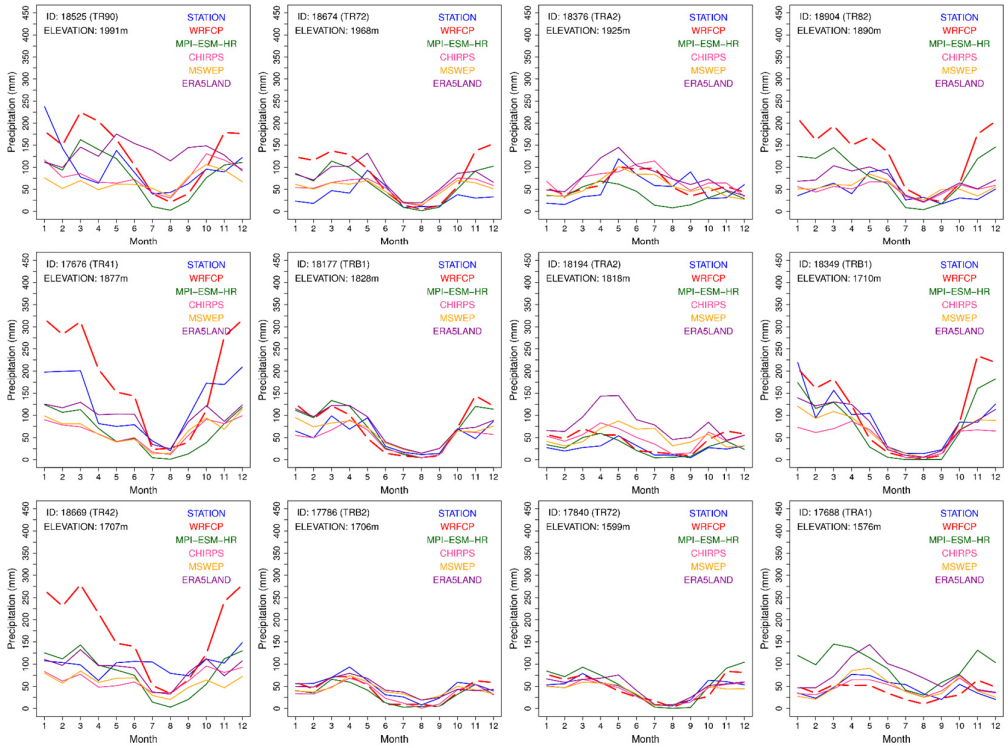

Figure 3.17 : The monthly mean total precipitation for each dataset at the TSMS stations for E3 elevation category.

In the E2 stations between 1000-1500 m elevation, the results are shown in Figure 3.18. The WRFCP is close to the observations for 18179, 17747, and 17846 stations but has a positive bias in winter and spring for other stations. For the low-elevation E1 stations from 0 to 1000 m, MPI-ESM-HR and WRFCP are generally close to the station observations and reference datasets, as shown in Figure 3.19.

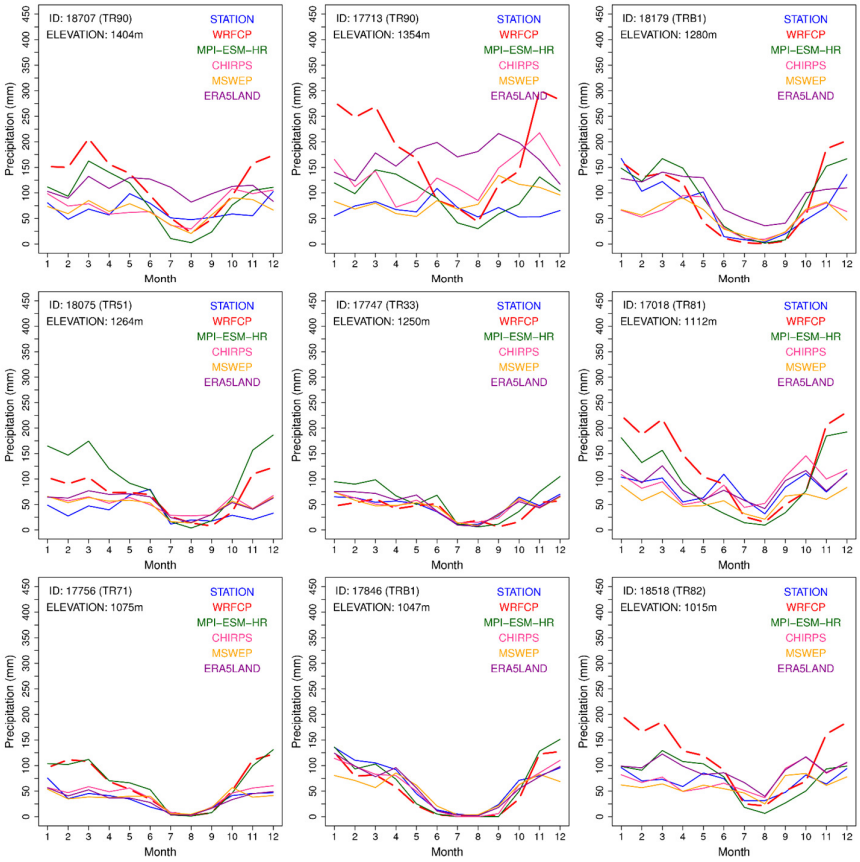

Figure 3.18 : The monthly mean total precipitation for each dataset at the TSMS stations for E2 elevation category.

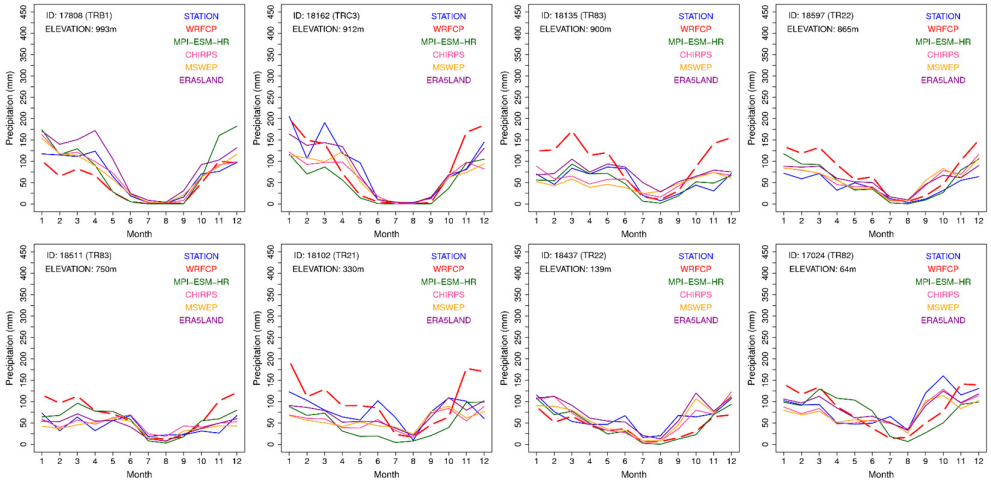

Figure 3.19 : The monthly mean total precipitation for each dataset at the TSMS stations for E1 elevation category.

The RMSE of monthly total precipitation climatologies for WRFCP, MPI-ESM-HR, and reference datasets comparing with the station observations are given in Table 3.5.

In 11 stations, WRFCP has a lower RMSE compared to MPI-ESM-HR, but it has a higher RMSE compared to reference datasets for all stations.

Table 3.5 : The monthly mean total precipitaton RMSE for each dataset at the selected TSMS station observation points.

Station ID	WRFCP RMSE (mm)	MPIESMHR RMSE (mm)	ERA5LAND RMSE (mm)	MSWEP RMSE (mm)	CHIRPS RMSE (mm)
18584	44.26	37.43	42.86	39.89	40.73
18715	131.57	76.5	64.08	38.18	82.73
18732	130.24	79.38	98.44	66.99	52.66
18149	86.68	36.59	42.36	48.83	45.65
18730	189.07	90.12	77.55	43.51	44
17692	19.24	20.71	18	22.24	12.89
18174	124.3	56.17	26.11	31.83	34.79
18378	25.38	24.25	30.92	35.28	39.28
18525	69.03	55.34	69.77	61.26	48.18
18674	71.75	44.98	44.19	24.9	27.34
18376	26.98	38.8	37.53	23.81	37.27
18904	102.91	60.77	27.41	15.74	18.66
17676	86.27	74.55	54.66	75.48	78.47
18177	41.19	35.08	27.69	16.45	17.07
18194	24.1	13.18	61.03	30.04	26.15
18349	58.48	41.06	27.87	36.04	54.95
18669	108.5	45.93	31.53	47.18	39.18
17786	15.3	19	9.72	13.11	15.97
17840	17.35	22.01	10.73	9.46	7.41
17688	22.36	62.52	33.63	10.34	10.89
18707	72.75	47.15	46.53	21.29	25.55
17713	147.12	46.67	105.1	34.71	80.29
18179	44.07	36.24	35.95	44.8	42.82
18075	48.12	88.73	21.97	19.96	22.69
17747	18.4	25.36	8.93	5.87	5.39
17018	83.05	59.62	14.83	27.68	17.8
17756	42.45	43.66	7.28	10.61	12.28
17846	25.87	25.12	10.98	25.98	12.69
18518	68.69	28.04	28.89	18.45	21.75
17808	28.44	41.59	31.18	16.16	16.22
18162	42.29	52.73	22.93	42.2	42.72
18135	59.14	14.5	22.71	27.43	21.67
18597	45.88	24.04	21.4	25.55	24
18511	40.7	24.71	15.59	16.24	12.63
18102	51.79	45.31	23.85	32.8	32.22
18437	26.38	26.01	23.54	21.19	20.97
17024	42.05	53.04	20.31	22.13	16.46

3.2.2 Validation of daily precipitation extremes

In order to evaluate the model performance for daily precipitation extremes, we compared the daily maximum precipitation amount of each dataset, as shown in Figure 3.20. The analyses indicate that WRFCP gives better daily maximum precipitation amount estimates than MPI-ESM-HR, especially over mountainous areas, compared to reference datasets. In particular, WRFCP is closely in agreement with high-resolution CHIPRS estimates over the Black Sea coast of Turkey, Eastern Anatolia, and the Caucasus.

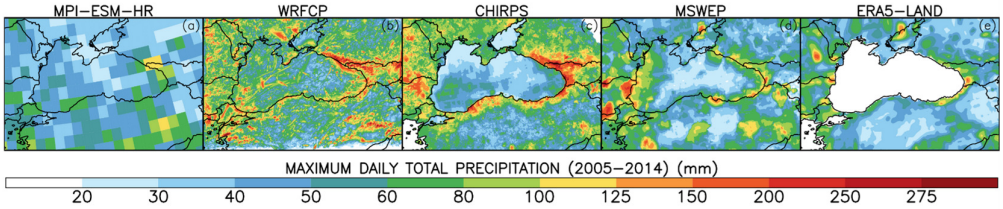

Figure 3.20 : The maximum daily total precipitation of each dataset between 2005-2014.

Moreover, we compared the daily precipitation probabilities of WRFCP, MPI-ESM-HR, and MSWEP with the station observations. Figure 3.21, Figure 3.22, Figure 3.23, and Figure 3.24 show daily precipitation probabilities for E4, E3, E2, and E1 stations, respectively. Although WRFCP has a general positive bias for monthly total precipitations, it better represents the daily precipitation probabilities compared to MPI-ESM-HR. Furthermore, for most stations, the daily precipitation probabilities of WRFCP are closer to the observations compared to MPI-ESM-HR and MSWEP for daily precipitation values above 50 mm/day, which can be considered extreme precipitation. In particular, this is more pronounced for high-elevation E4 stations, for example, 18732 and 18149 stations.

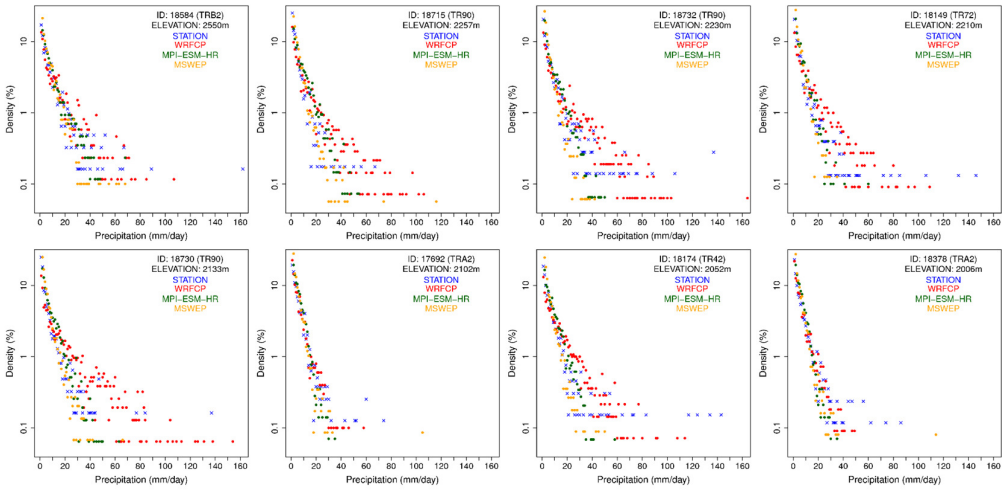

Figure 3.21 : The daily total precipitation probabilities of WRFCP (red), MPI-ESM-HR (green), and MSWEP (yellow) at the TSMS stations for E4 elevation category.

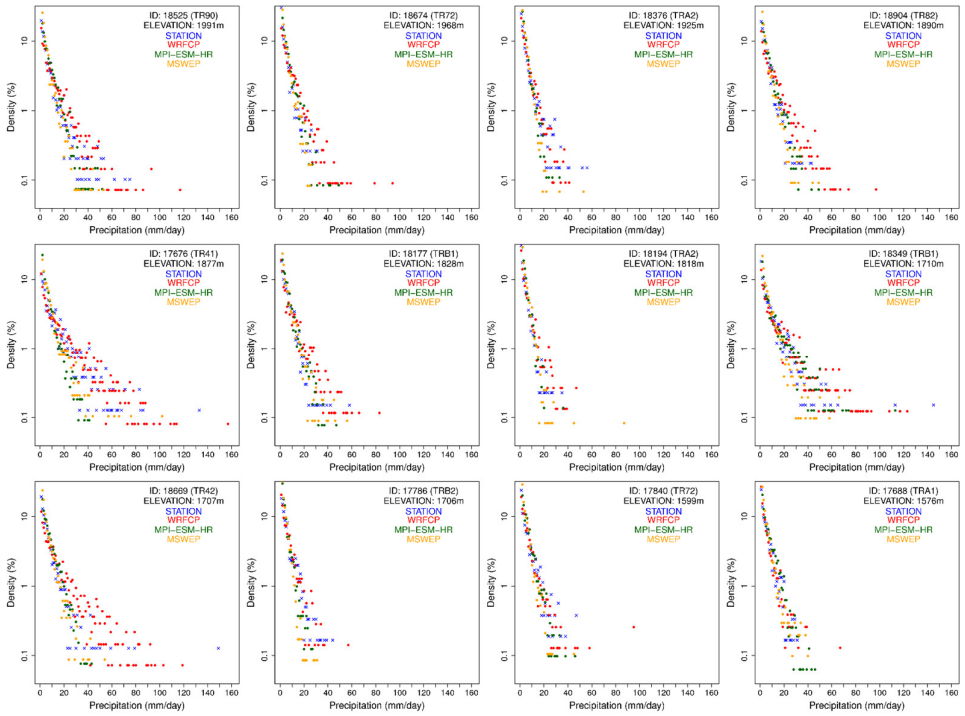

Figure 3.22 : The daily total precipitation probabilities of WRFCP (red), MPI-ESM-HR (green), and MSWEP (yellow) at the TSMS stations for E3 elevation category.

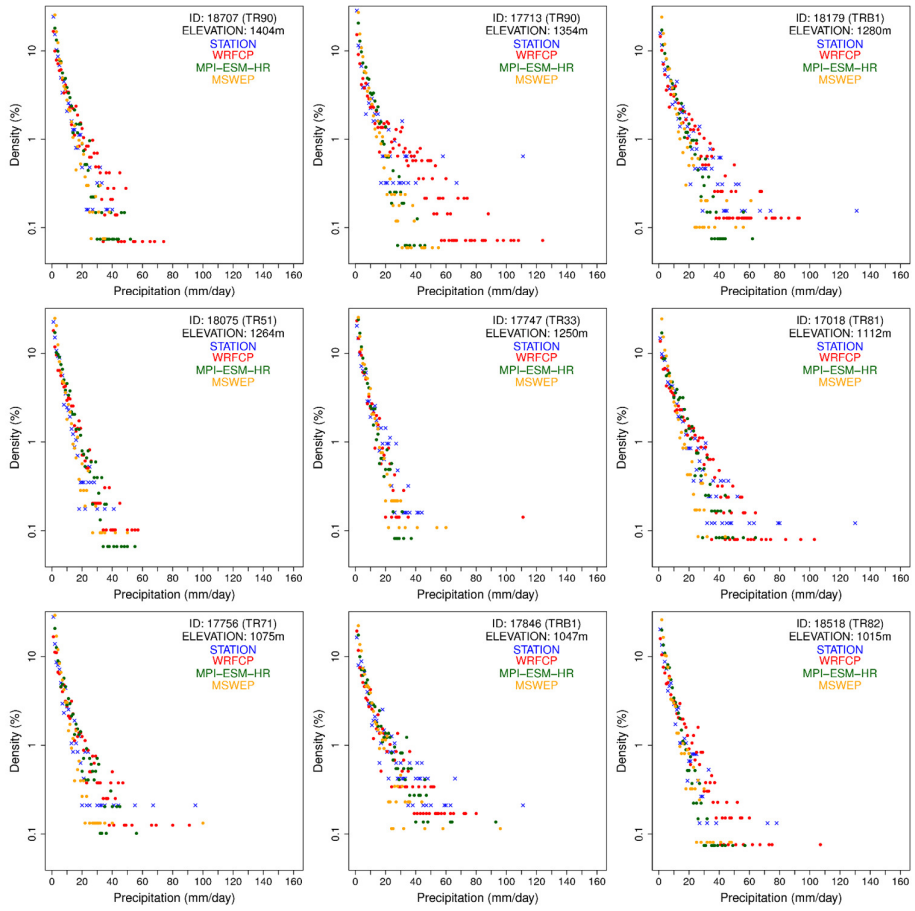

Figure 3.23 : The daily total precipitation probabilities of WRFCP (red), MPI-ESM-HR (green), and MSWEP (yellow) at the TSMS stations for E2 elevation category.

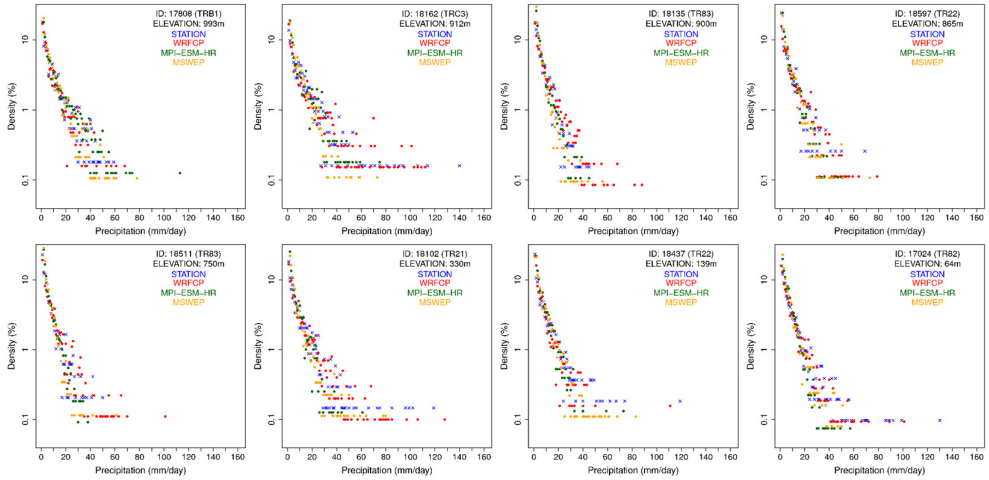

Figure 3.24 : The daily total precipitation probabilities of WRFCP (red), MPI-ESM-HR (green), and MSWEP (yellow) at the TSMS stations for E1 elevation category.

Furthermore, as an extreme indicator, we calculated daily extreme precipitation thresholds as the 90th, the 99th, and the 99.9th percentiles for each dataset between 2005-2014 and gave the results in Figure 3.25. We found that WRFCP has higher daily extreme precipitation thresholds and these values are closer to the reference datasets compared to MPI-ESM-HR outputs. In particular, WRFCP is in significant agreement with CHIRPS and substantially improves the MPI-ESM-HR outputs for the 99th and the 99.9th percentiles over mountainous areas.

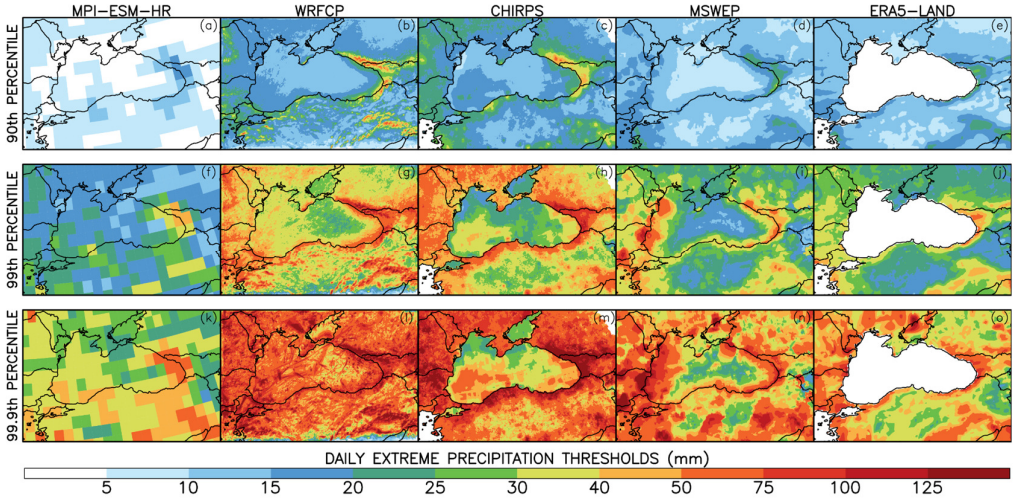

Figure 3.25 : The daily extreme precipitation thresholds as the 90th (a-e), the 99th (f-j), and the 99.9th (k-o) percentiles of each dataset between 2005-2014.

3.2.3 Comparison of subregional 3-hourly precipitation probabilities

In addition to seasonal and daily comparisons, we compared 3-hourly MPI-ESM-HR and WRFCP precipitation outputs with 3-hourly MSWEP precipitation for each subregion of the BSA. We calculated 3-hourly precipitation probabilities for all grids points and timesteps within the regions and showed the results in Figure 3.26. In general, MPI-ESM-HR follows the density curve of MSWEP until around 12 mm/3hr precipitation amount, but for higher values, it gives lower probabilities compared to MSWEP and lacks in the representation of extreme precipitation values. On the other hand, although WRFCP exhibits a positive bias, it is in agreement with the density curve of MSWEP. In particular, WRFCP densities are very close to MSWEP densities for TR83, TR90, TRA1, and TRA2 subregions over the northeast and the Eastern Black Sea region of Turkey.

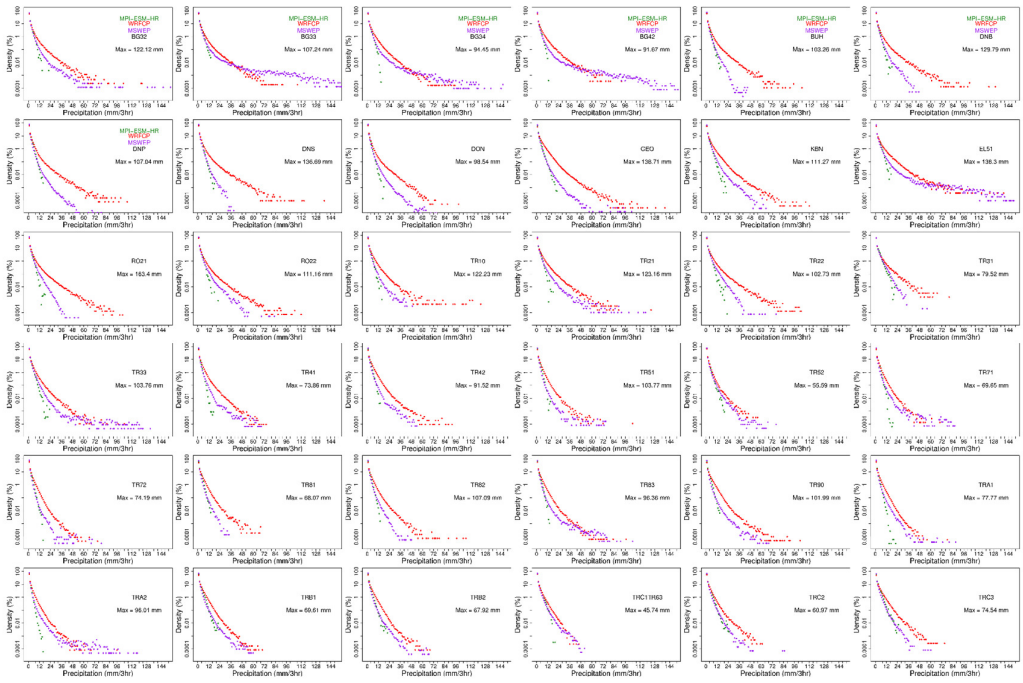

Figure 3.26 : The 3-hourly precipitation probabilites of MPI-ESH-HR (green), WRFCP (red), and MSWEP (purple) in each subregion.

To summarise, although the WRFCP has regional and seasonal biases compared to reference datasets and station observations, it significantly improves the daily and sub-daily precipitation amounts compared to MPI-ESM-HR. These results highlight the added value of our high-resolution convection-permitting simulation over the complex topography compared to a low-resolution GCM in the representation of precipitation.

4. RESULTS OF FUTURE CLIMATE SIMULATION

In this section, we examined the changes in the temperature and precipitation over the BSA for the 2061-2070 period and discussed possible reasons for the changes.

4.1 Changes in Temperature

4.1.1 Seasonal mean temperature changes

The future change of the daily mean 2m air temperature (Tmean) for each season and the confidence level of the change based on Welch's t-test are given in Figure 4.1 and Figure 4.2, respectively. The results show that the seasonal mean temperature increases in spring, summer, and autumn at a 99% confidence level across the area of interest. In the spring, this warming is by 2-2.5°C over most of the simulation domain. Especially the warming rate over the mountainous Eastern Anatolia region of Turkey reaches up to 3°C. Furthermore, the most pronounced warming occurs in summer, exceeding 3°C over a broad part of the Anatolian Peninsula, the Balkans, and a part of Ukraine and Russia. In the autumn, the mean temperature increases between 1.5-3°C, and the warming rate is higher over the east of the BSA.

The temperature changes are related to changes in the surface energy budget, which is directly affected by the cloud cover. Therefore, we analysed future changes of the low-, mid-, and high-level cloud covers and showed the results in Figure 4.3. The results indicate that the Tmean does not change significantly in winter. This can be related to the increase in the low-level clouds in winter suppressing the warming over a broad part of the BSA. Even there is a local cooling signal of about 0.75°C over Georgia and the south of Russia, where the low-level cloud cover increases by about 8%.

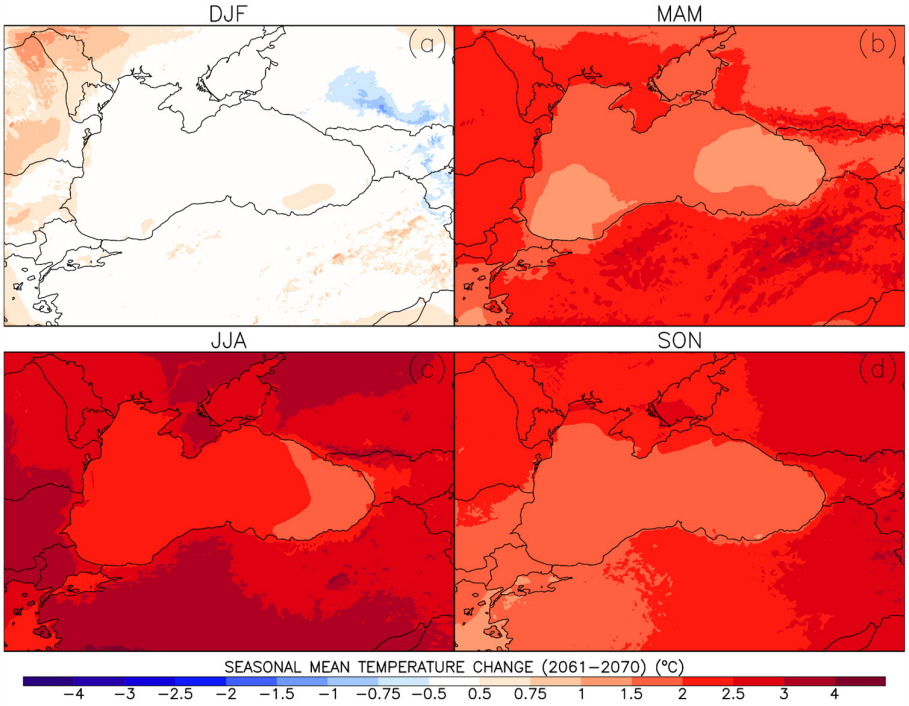

Figure 4.1 : The future change of 2m air temperature for all seasons.

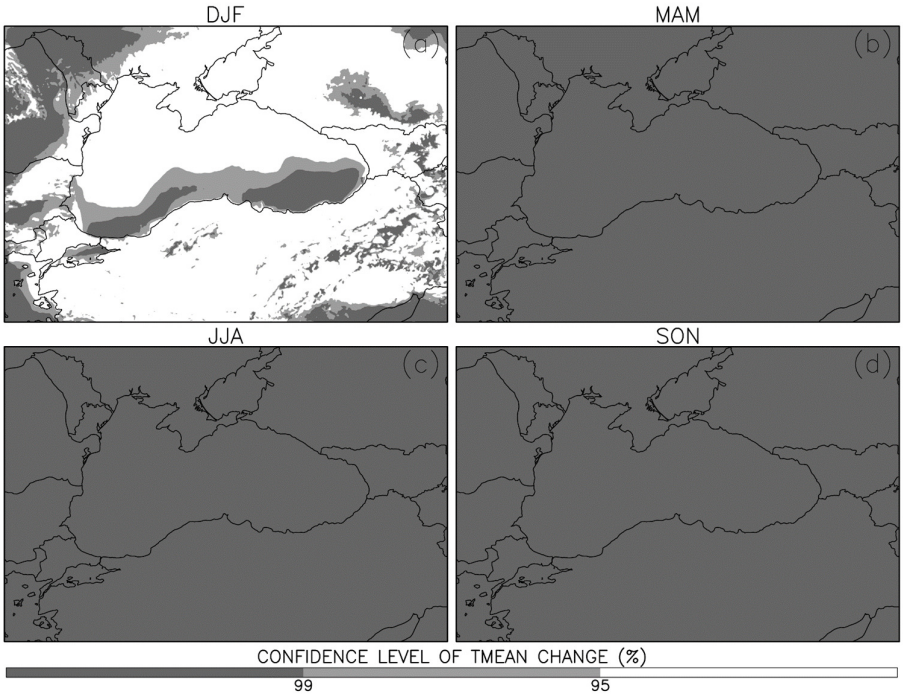

Figure 4.2 : The confidence level of future change of 2m air temperature.

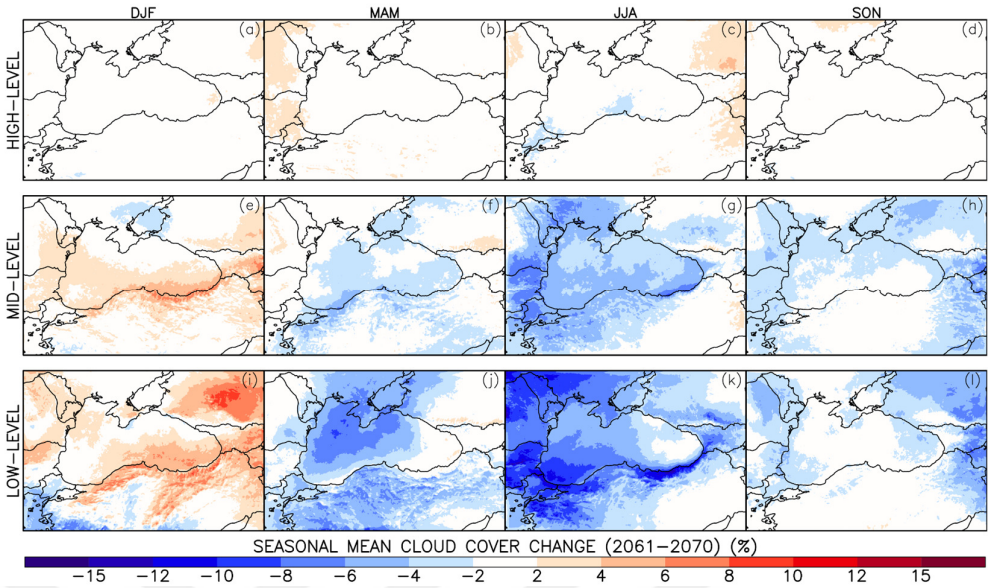

Figure 4.3 : The future change of the seasonal mean high- (a-d), mid- (e-h), and low-level (i-l) cloud cover.

Nonetheless, there is regional warming of about 1°C in winter over the higher elevations of Bulgaria, Romania, Moldova, and Turkey. This warming can be explained by the change in the surface albedo, which triggers a feedback mechanism. Figure 4.4 shows the change in the seasonal mean surface albedo. In winter, the mean surface albedo decreases by about 6% over the Carpathians and Eastern Anatolia. Moreover, the most pronounced decrease in the mean surface albedo occurs in spring by more than 10% over the mountains of Eastern Anatolia, where the most significant warming is in the same season over the BSA. These high-elevated regions are snow-covered areas in winter and spring, and future warming can cause a reduction in the snow cover leading to a decrease in the surface albedo. The albedo decrease further increases the shortwave radiation absorption and causes additional warming over these regions. Besides, the warming of the higher elevations, particularly the mountains of Eastern Anatolia, can cause hydrological impacts in the future because the snow melt over these regions is the source of many river systems, including the Euphrates and the Tigris Rivers.

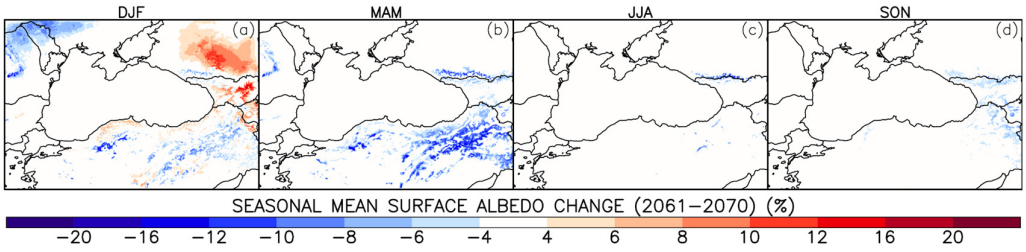

Figure 4.4 : The future change of the seasonal mean surface albedo.

Moreover, we calculated changes in the seasonal mean SST over the Black Sea and showed the results in Figure 4.5. In the winter, a broad part of the Black Sea warms by 0.5-1°C. Furthermore, the highest warming rate is between 1-1.5°C and occurs over the central and eastern Black Sea coast of Turkey. In the spring, the mean SST increases by about 1°C across the Black Sea. In the summer, the highest warming rates exceeding 2°C are over the western and central parts of the Black Sea. The warming rate over the eastern Black Sea is between 1.5-2°C. In the autumn, the warming of the SST is around 1.5°C across the Black Sea.

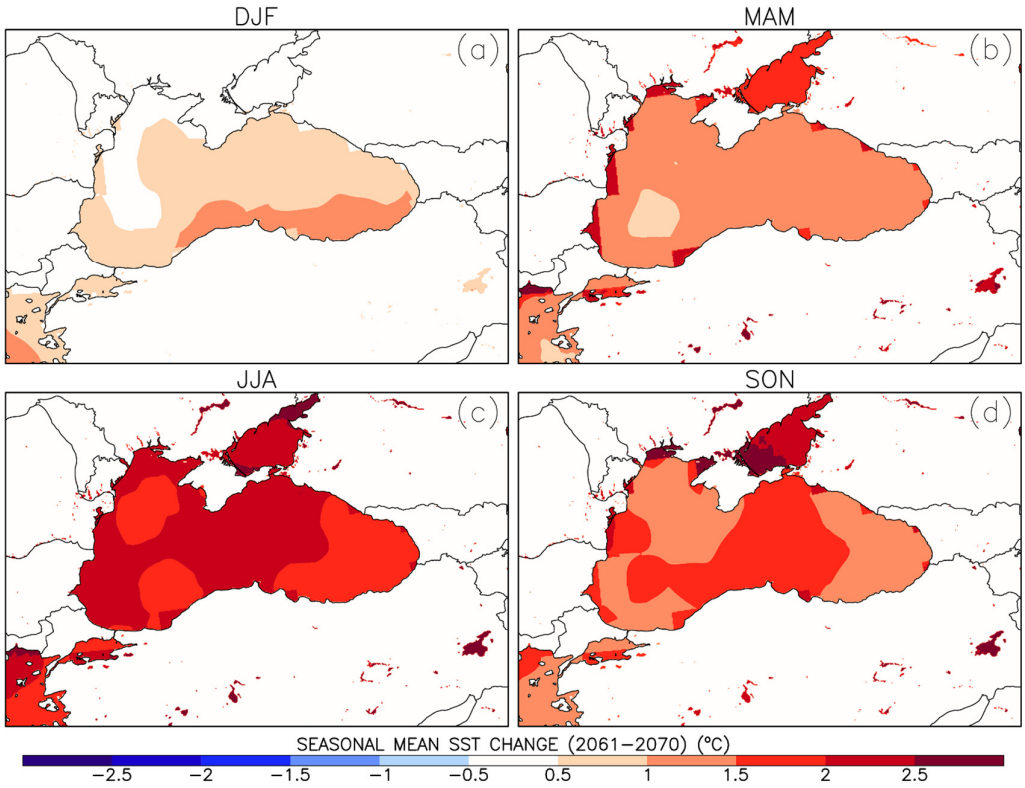

Figure 4.5 : The seasonal SST change for 2061-2070.

4.1.2 Future temperature extremes

In addition to the mean temperature changes, we also analysed future changes of Tmin and Tmax. Figure 4.6 shows the future change of seasonal mean Tmin. In the winter, there is significant warming over the mountains of Eastern Anatolia and the Carpathians between 1-1.5°C. Similarly, in the spring, the warming rate over the same region in addition to the Caucasus exceeds 3°C. In the summer, the increase in the Tmin is around 2.5°C across the domain. For the autumn, the change of the Tmin point outs a 2°C warming over the area of interest.

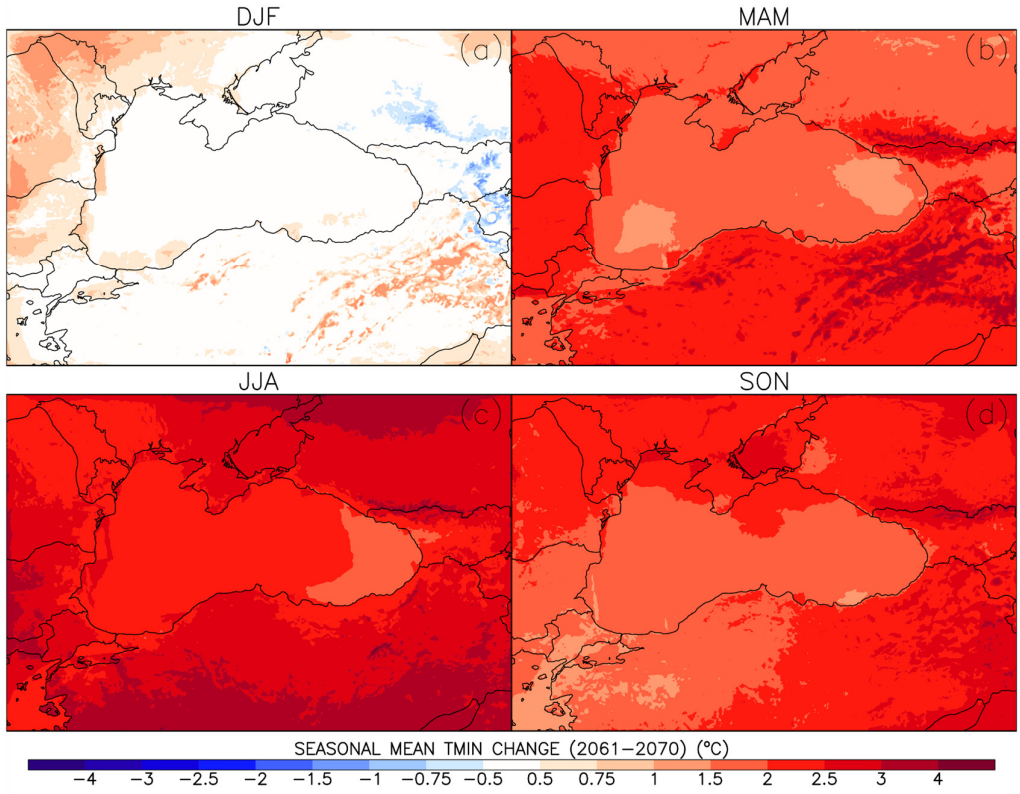

Figure 4.6 : The future change of mean 2m minimum air temperature for all seasons.

Figure 4.7 shows the future change of seasonal mean Tmax. The results show that there is a significant cooling in winter over the south of Russia by around 1.5°C. On the other hand, in the spring, there is a warming by about 2.5°C across the BSA and, in particular, exceeds 3°C over Eastern Anatolia. The highest increase in the Tmax is in the summer, reaching up to 3°C over a broad part of the simulation domain. In the autumn, while the increase of the Tmax is around 1.5°C over the west of the domain, it exceeds 2.5°C over the eastern part of the study area.

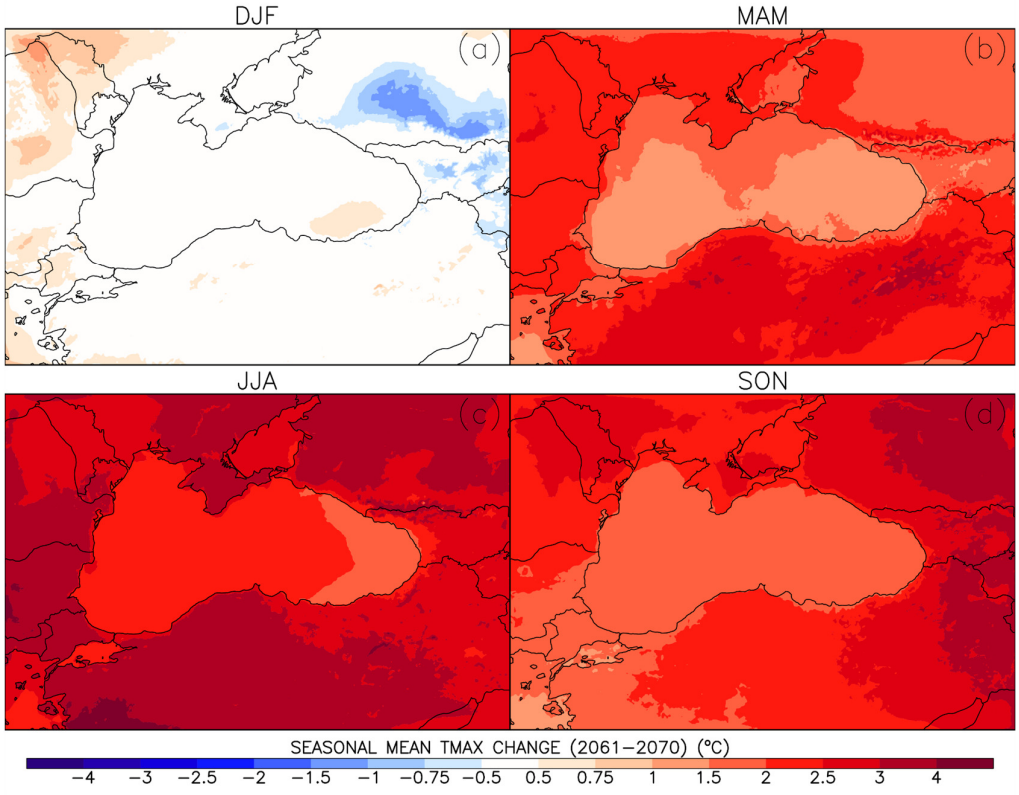

Figure 4.7 : The future change of mean 2m maximum air temperature for all seasons.

We also calculated seasonal changes in the diurnal temperature range (DTR) and showed the results in Figure 4.8. The analyses indicate that the DTR decreases by about 1°C in the winter over Eastern Anatolia. In the spring, while the DTR decreases over the northeast of Turkey and the Caucasus by around 0.75°C, it increases over a part of Central Anatolia and Crimea. In the summer, there is a noticeable increase in the DTR over the northwest of Turkey, Bulgaria, Romania, and Crimea. Specifically, the increase in the DTR is more than 1°C over a broad part of Bulgaria and the South Marmara Region of Turkey. In the autumn, the DTR increases between 0.5-1°C over a part of Central and Eastern Anatolia, Georgia, and the south of Russia.

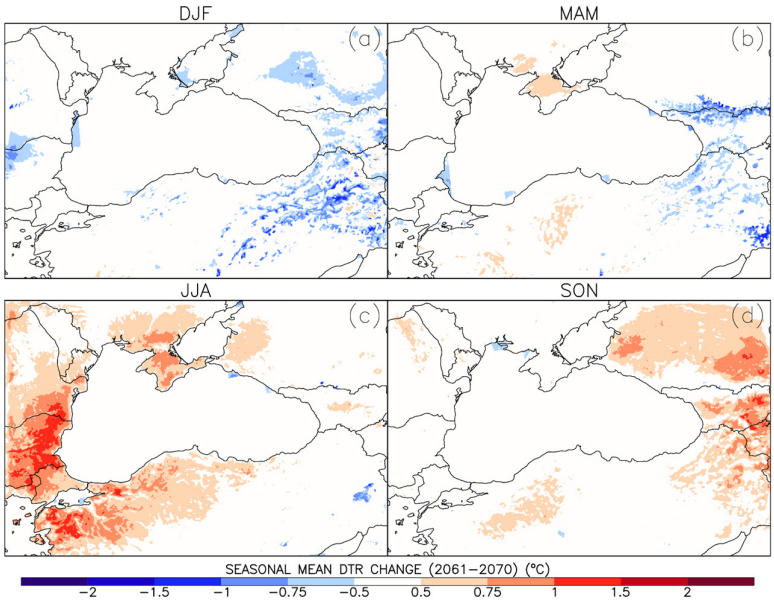

Figure 4.8 : The future change of diurnal temperature range for all seasons.

Given the significant increase in the Tmax in the future, we calculated seasonal changes in the fraction of the very warm days index (TX90P), as shown in Figure 4.9, based on the 90th percentile of the daily maximum temperatures in the reference period. The results show that the TX90P increases by about 10% over a broad part of the BSA. The highest increase of TX90P, reaching up to 12%, occurs over the west of the study area. In particular, this increase exceeds 13% over the south of Istanbul.

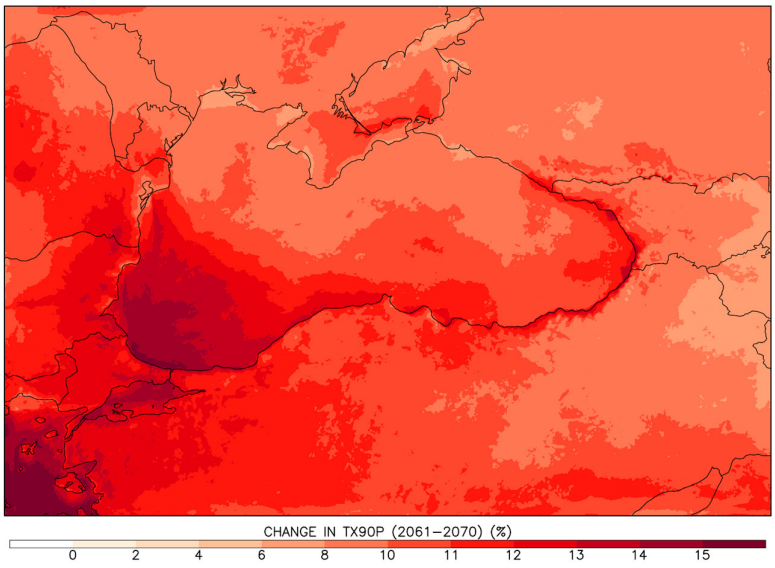

Figure 4.9 : The percent change in the very warm days index between 2061-2070.

4.2 Changes in Precipitation

4.2.1 Seasonal precipitation changes

The future change of seasonal total precipitation and the significance level of the change are given in Figure 4.10 and Figure 4.11, respectively. In the winter, the most significant change in the total precipitation is over the eastern coast of the Black Sea and Georgia and is around 3 mm/day, at least at a 95% confidence level. In particular, the increasing rate reaches up to 4 mm/day over the Kaçkar Mountains in the Eastern Black Sea region of Turkey at a 99% confidence level. In the spring, there is a domain-wide reduction in the total precipitation at a rate of about 2 mm/day. This change is statistically significant at a 99% confidence level over the central part of the Black Sea region of Turkey and the western coast of the Azov Sea. In the summer, the total precipitation rate decreases only about 1 mm/day and is significant over the west coast of the Black Sea, the Marmara Region of Turkey, except for Istanbul, and a part of Western Anatolia. In autumn, although there is a precipitation increase of about 1 mm/day over the Black Sea coast of Turkey, these changes are statistically insignificant.

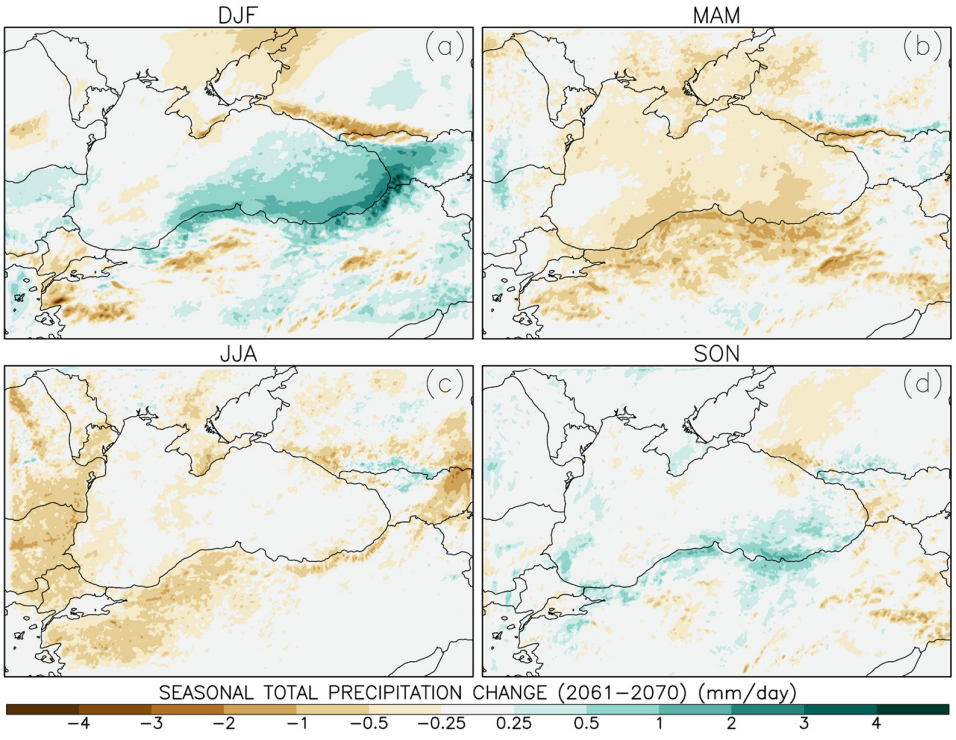

Figure 4.10 : The future change of seasonal total precipitation.

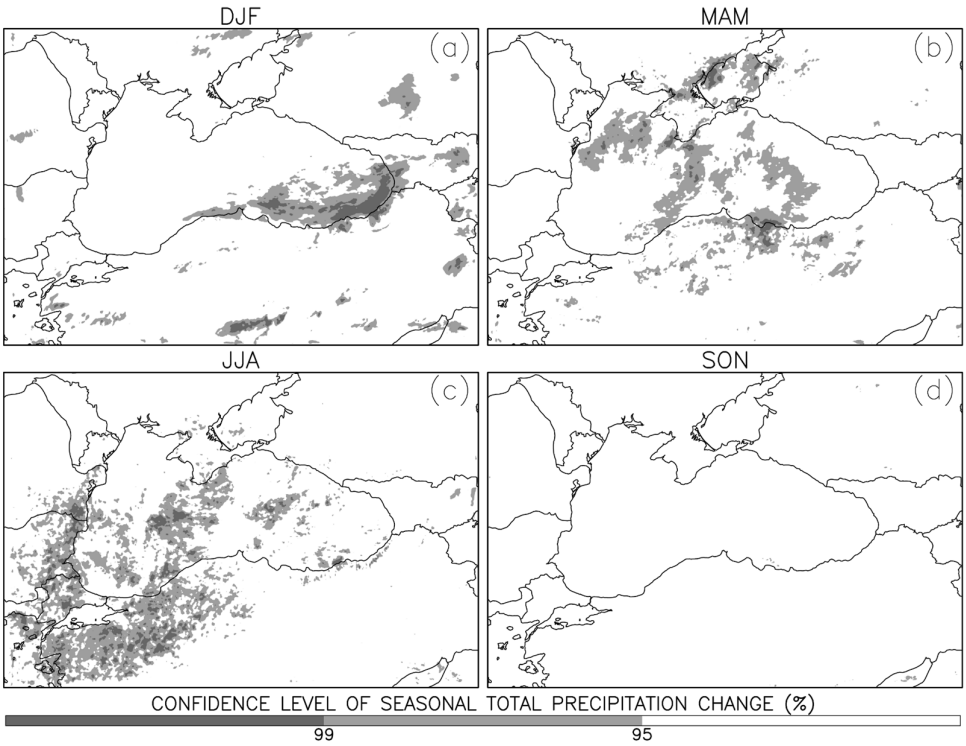

Figure 4.11 : The confidence level of future change of seasonal precipitation.

Furthermore, Figure 4.12 shows the change in the number of wet days (>1 mm/day precipitation) in a season per year. In the winter, in line with the precipitation increase, the number of wet days rises in the future over a broad part of the Black Sea Basin. In particular, this increase is of about 8 days per year over the coastal areas of Turkey and Georgia. On the other hand, in spring and autumn, the number of wet days decreases across the BSA locally by up to 10 days per year because of the drying in these seasons. In the autumn, the number of wet days does not change significantly.

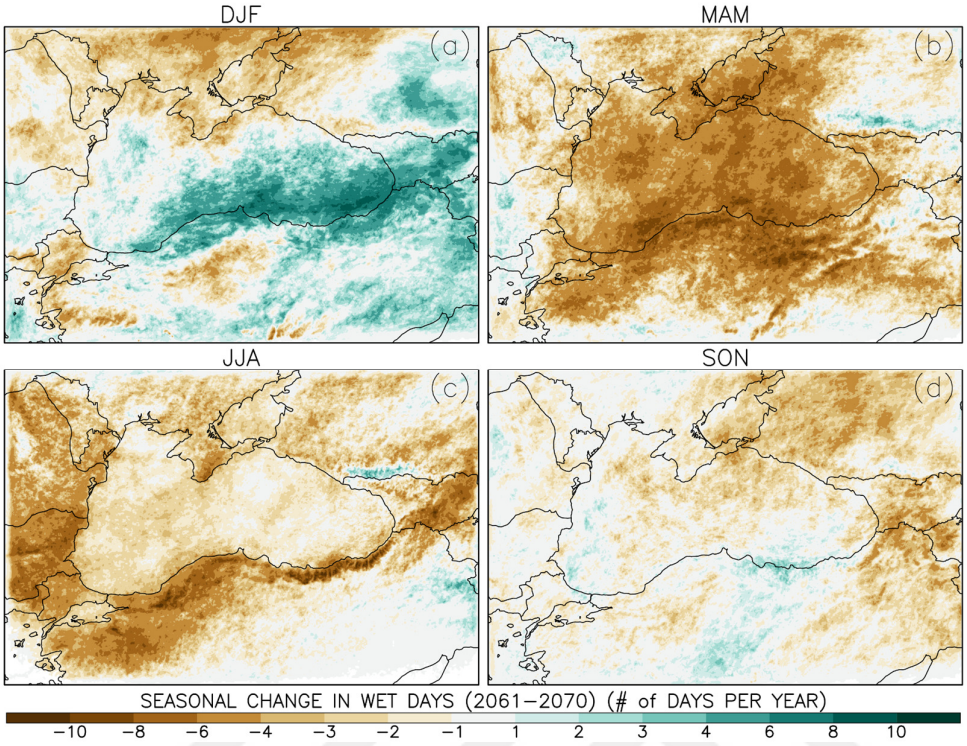

Figure 4.12 : The future change of the seasonal number of wet days per year.

The significant precipitation increase in winter over the Eastern Black Sea region can be related to the intensified moisture supply due to the increased evaporation. To this end, we analysed the change in surface evaporation in winter. Moreover, we examined the mean 850 hPa wind to reveal the mean flow in order to gain insight into the moisture transport at the lower troposphere. Figure 4.13 shows the change in winter total surface evaporation and the winter climatological mean of 850 hPa level wind vectors for the 2061-2070 period over the Eastern Black Sea region. The results highlight that the total surface evaporation increases by about 15% in winter over the southeast of the Black Sea. This intensification is due to the pronounced warming of the SST in winter over the same area (Figure 4.5). We also analysed changes in the U and V components of the mean 850 wind and showed the results in Figure 4.14. We found a strengthening in the U component and a weakening in the V component of the mean 850 hPa wind over the southeast of the Black Sea. Thus, the enhanced westerly mean 850 hPa flow at the lower troposphere carries the additional moisture input to the eastern coast of the Black Sea and results in an enhancement in the precipitation over this area. Furthermore, the weakening of the southerly flow at the 850 hPa level

increases the moisture content over the coastal regions of Turkey, which in turn intensifies the precipitation induced by the orographic forcing.

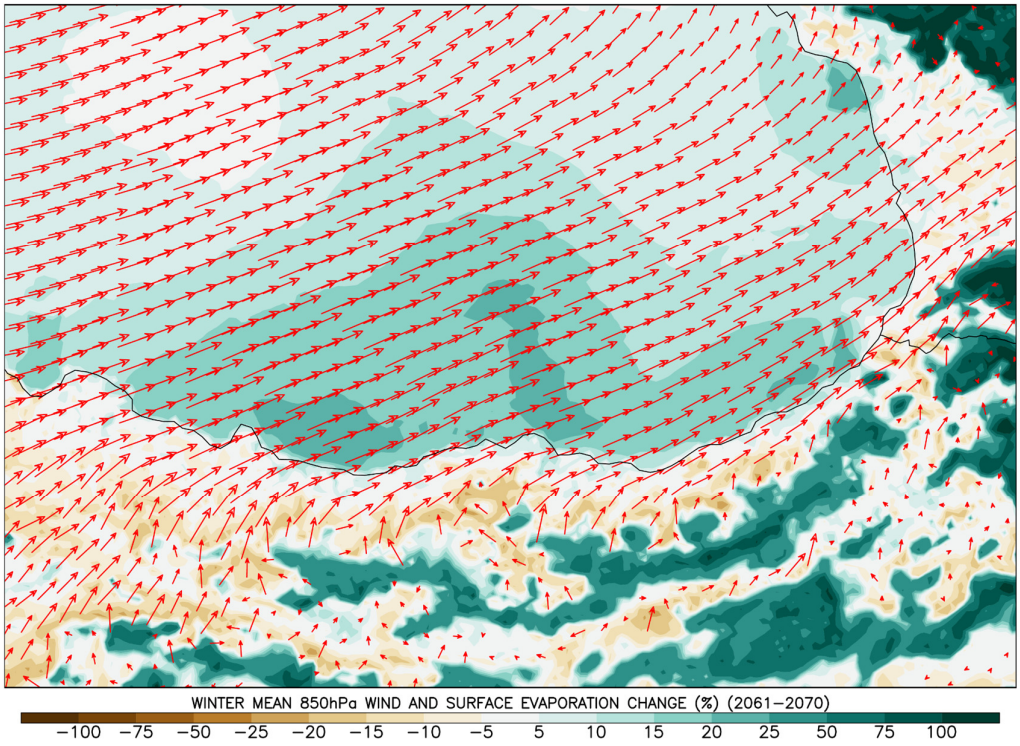

Figure 4.13 : The future winter mean of 850 hPa wind (vectors) and the future change of surface evaporation (shaded).

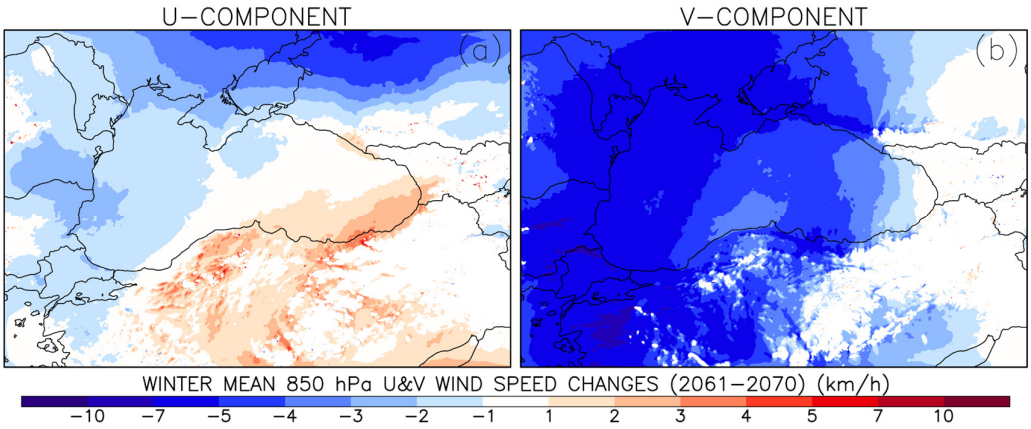

Figure 4.14 : The future change of the winter mean U and V components of 850 hPa wind.

4.2.2 Future precipitation extremes

In addition to changes in the mean climate, extreme precipitation analyses are also crucial because of the environmental and societal impacts. Therefore, we carried out

analyses to investigate future precipitation extremes. Figure 4.15 shows the maximum daily total precipitation amounts for 2005-2014 and 2061-2070 periods. The results indicate that the maximum daily precipitation amount increases in the future compared to the 2005-2014 period over the parts of the Marmara Region, the coastal areas of Turkey, and the Caucasus. In particular, the maximum values exceed 225 mm over the Central Black Sea region of Turkey and 350 mm over the Black Sea coast of the Marmara Region and over the Caucasus.

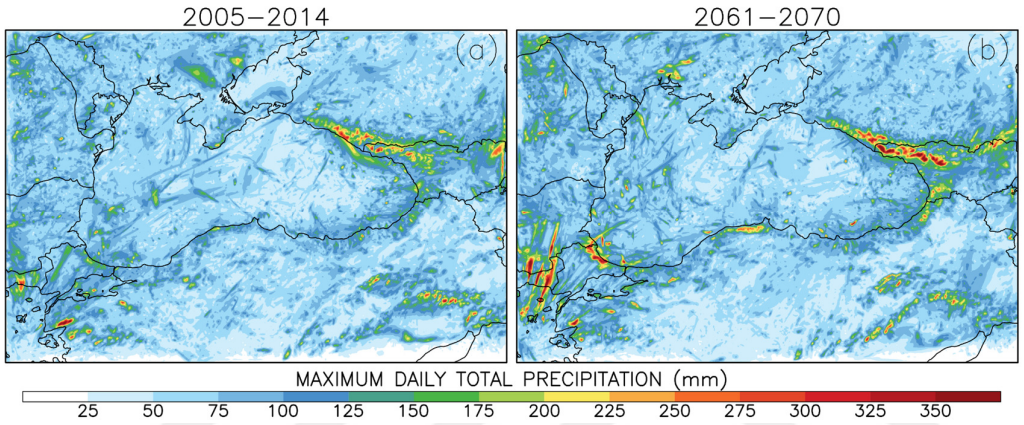

Figure 4.15 : The maximum daily precipitation for 2005-2014 (a) and 2061-2070 (b) periods.

To emphasize the daily precipitation intensification, we calculated percent changes in the number of very wet and extremely wet days based on the 90th and 99th percentile reference period thresholds, respectively, the changes in the R90P and R99P days indices. Figure 4.16 shows the change in the R90P days. The results show that the percentage of very wet days increases over a broad part of the Black Sea coast of Turkey and Georgia by around 3%. Moreover, as shown in Figure 4.17, R99P days increase by about 1% over the mountainous areas of the Eastern Black Sea region of Turkey and parts of Georgia.

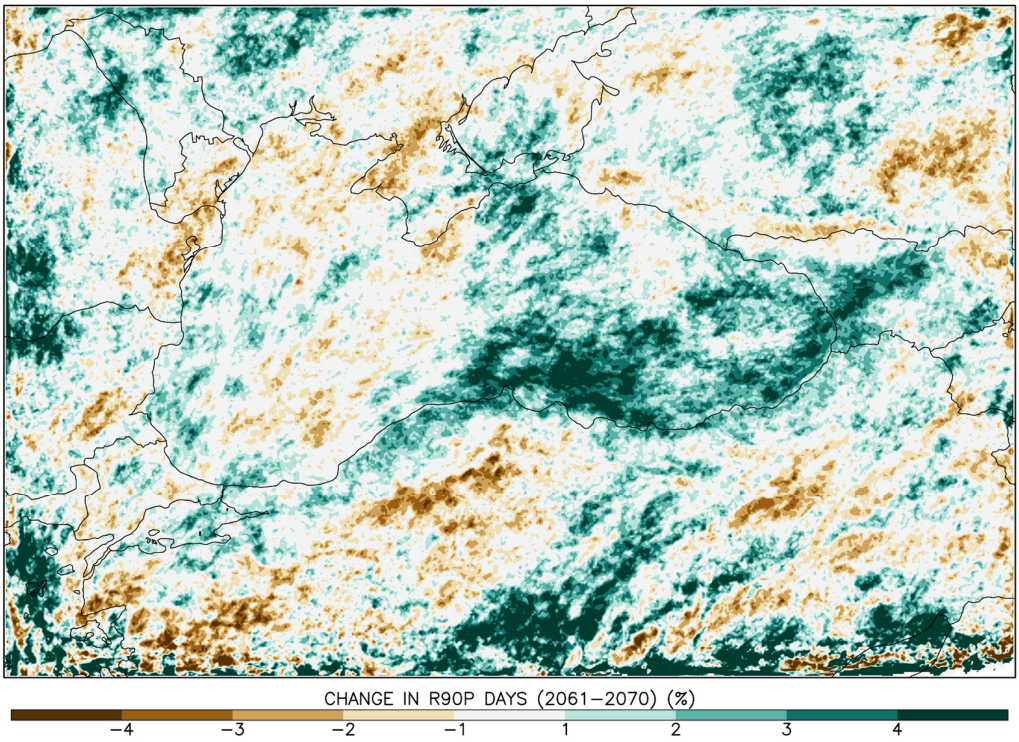

Figure 4.16 : The future change of the very wet days index.

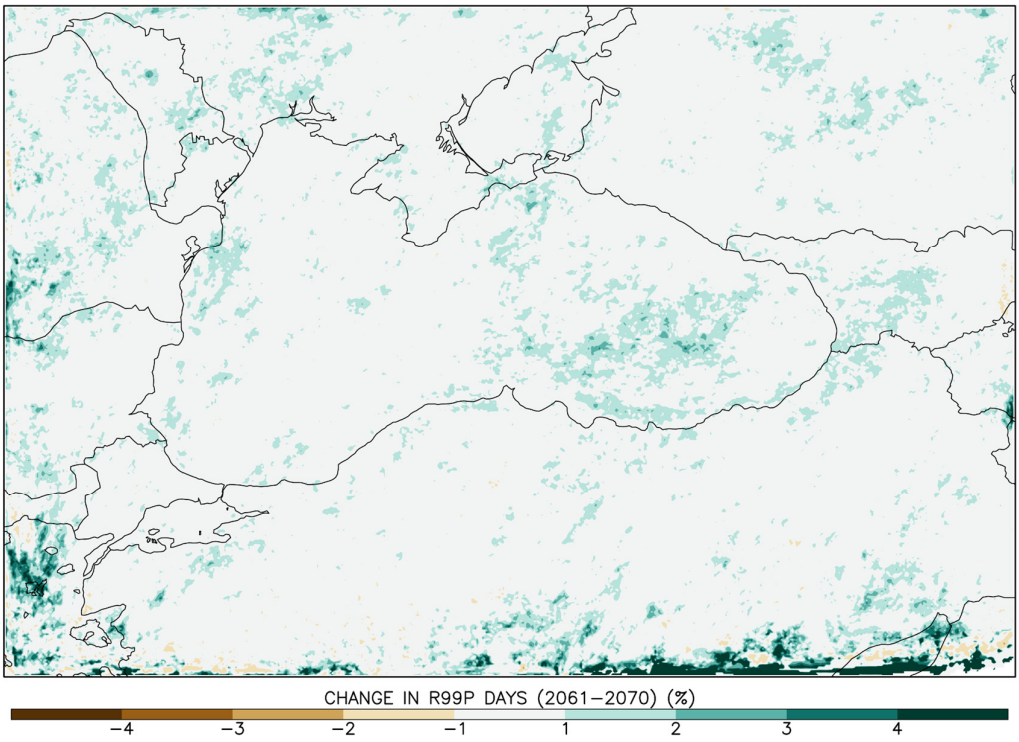

Figure 4.17 : The future change of the extremely wet days index.

To point out the shifting towards higher daily precipitation amounts, we calculated changes in the daily extreme precipitation thresholds as 90th, 99th, and 99.9th percentiles, as shown in Figure 4.18. Three of the percentiles shifts toward higher values in the future across the area of interest. In particular, this shift exceeds 18 mm for 99th and 99.9th percentiles over the higher elevations of the Eastern Black Sea region of Turkey and Georgia.

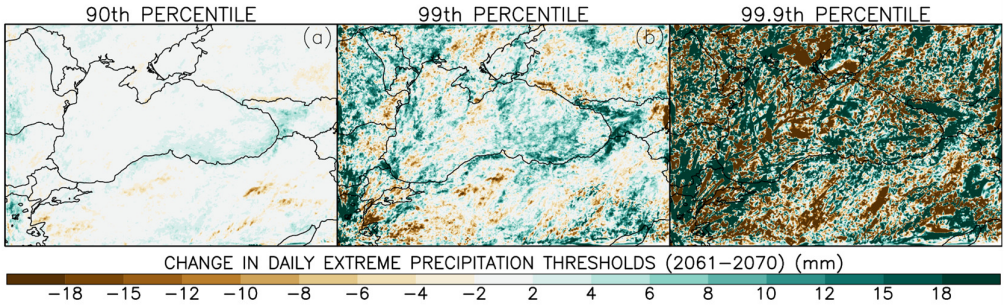

Figure 4.18 : The future change of the daily extreme precipitation thresholds.

4.2.2.1 Subregional analyses

In addition to domain-wide extreme precipitation analyses, we examined daily precipitation amounts on wet days for each subregion using all grid points and timesteps. Figure 4.19 shows reference and future period daily precipitation probabilities, the thresholds as 90th, 99th, and 99.9th percentiles, and maximum daily precipitation between 2061-2070 in the subregions. In accordance with the domain-wide analyses, there is a shift towards higher daily precipitation amounts in most subregions, especially after the 99.9th percentile. In particular, the increasing signal is more pronounced in the coastal regions such as BG34, DON, GEO, TR42, TR81, TR82, TR83, and TR90, with the indication of shifting in the thresholds toward higher values and estimation of maximum daily precipitation amounts reaching above 250 mm/day.

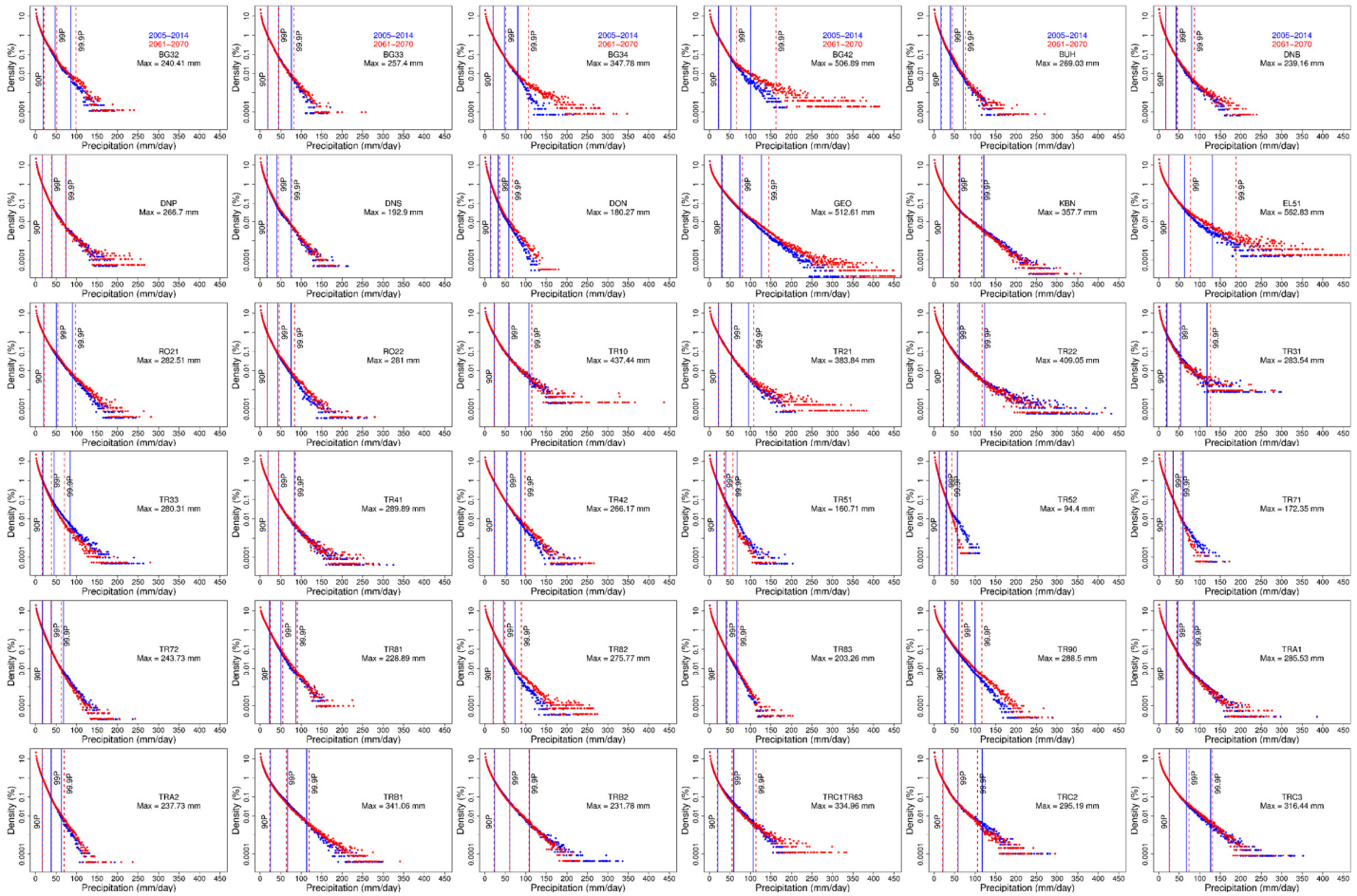

Figure 4.19 : The daily precipitation probabilities for 2005-2014 (blue) and 2061-2070 (red) periods in each subregion.

The daily analyses highlight the intensification of future precipitation, especially over the coastal areas. Therefore, as a detailed analysis, we analysed changes in the hourly precipitation probabilities in wet hours (>0.1 mm/hour precipitation) for the coastal subregions. The hourly precipitation probabilities for reference and future periods, along with 99.9th and 99.99th percentiles, and the maximum hourly precipitation amount in the 2061-2070 period in coastal subregions are given in Figure 4.20. The most pronounced increase in the hourly precipitation probabilities and shifting of the percentiles toward higher values are in the BG33, DON, GEO, KBN, TR42, TR82, TR83, and TR90 subregions, most of which are located in the Black Sea coast of Turkey and the east coast the Black Sea. Also, in these regions, maximum hourly precipitation amounts increase up to 100 mm/hour.

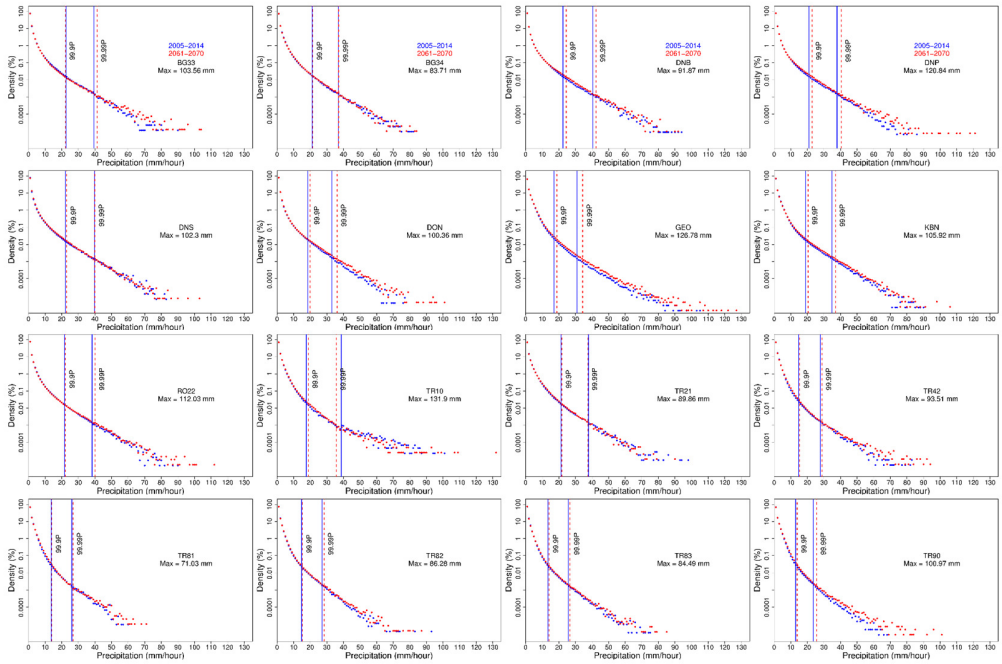

Figure 4.20 : The hourly precipitation probabilities for 2005-2014 (blue) and 2061-2070 (red) periods in coastal subregions.

Given the significant increase in the higher values of daily and sub-daily precipitation amounts, we analysed the diurnal cycle of precipitation for each season to highlight the intensification of future sub-daily precipitation in the coastal subregions. Figure 4.21 shows the diurnal precipitation cycle in winter for these subregions. Among the subregions, while GEO and TR90 in the eastern Black Sea part of the domain exhibit an increase in hourly precipitation, DNB, DNP, and KBN show a decrease for the 24 hours of the day. Furthermore, in the TR10 and TR42 subregions, while daytime

hourly precipitation amounts decrease, evening-time and night-time precipitation amounts increase in the future.

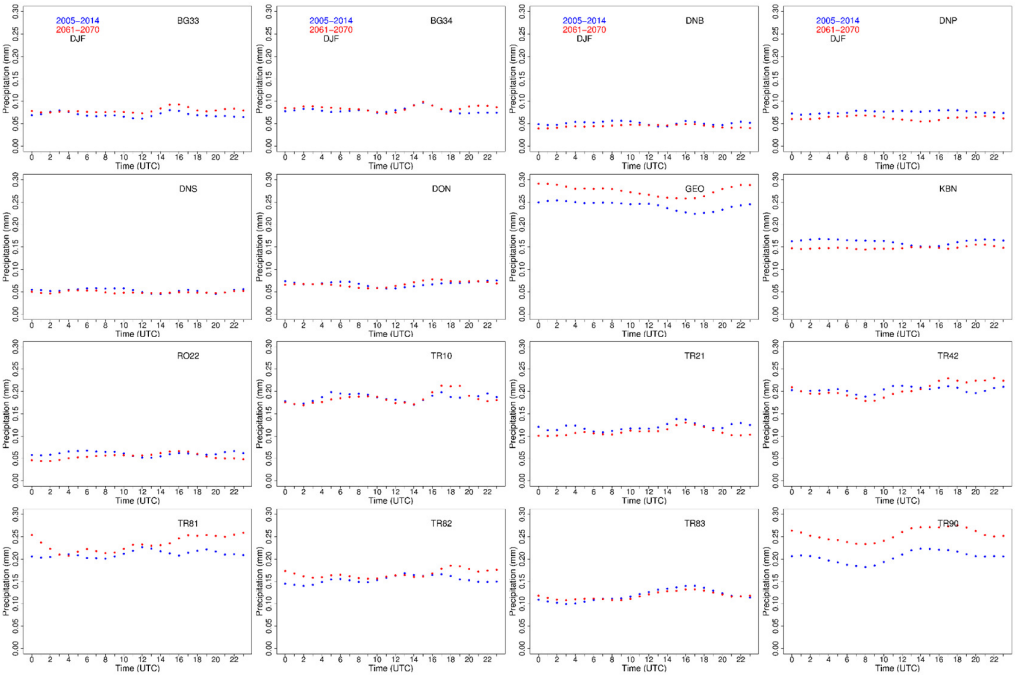

Figure 4.21 : Diurnal precipitation cycle based on mean hourly data over the coastal subregions for the reference and the future periods (winter).

For the spring, as shown in Figure 4.22, there is a reduction in the hourly precipitation amounts in most subregions, except in DON and KBN. In the DON and KBN subregions, there is an intensification of afternoon precipitation.

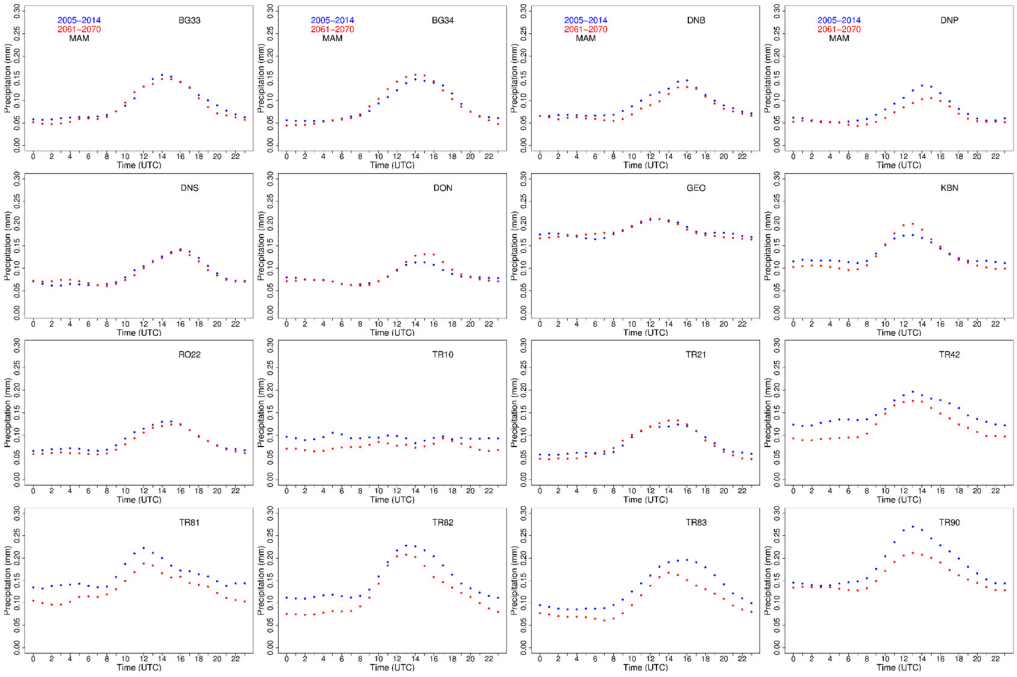

Figure 4.22 : Diurnal precipitation cycle based on mean hourly data over the coastal subregions for the reference and the future periods (spring).

In the summer, there is a significant decrease in the sub-daily precipitation over all coastal subregions, as shown in Figure 4.23. In particular, the BG33, BG34, TR21, TR42, TR81, and TR82 subregions exhibit a more pronounced reduction in the afternoon precipitation. Figure 4.21 shows the diurnal precipitation cycle in autumn. In the autumn, the afternoon precipitation increases in the TR81, TR82, and TR90 subregions of Turkey. Moreover, the noon precipitation intensifies in the TR10 (Istanbul) subregion.

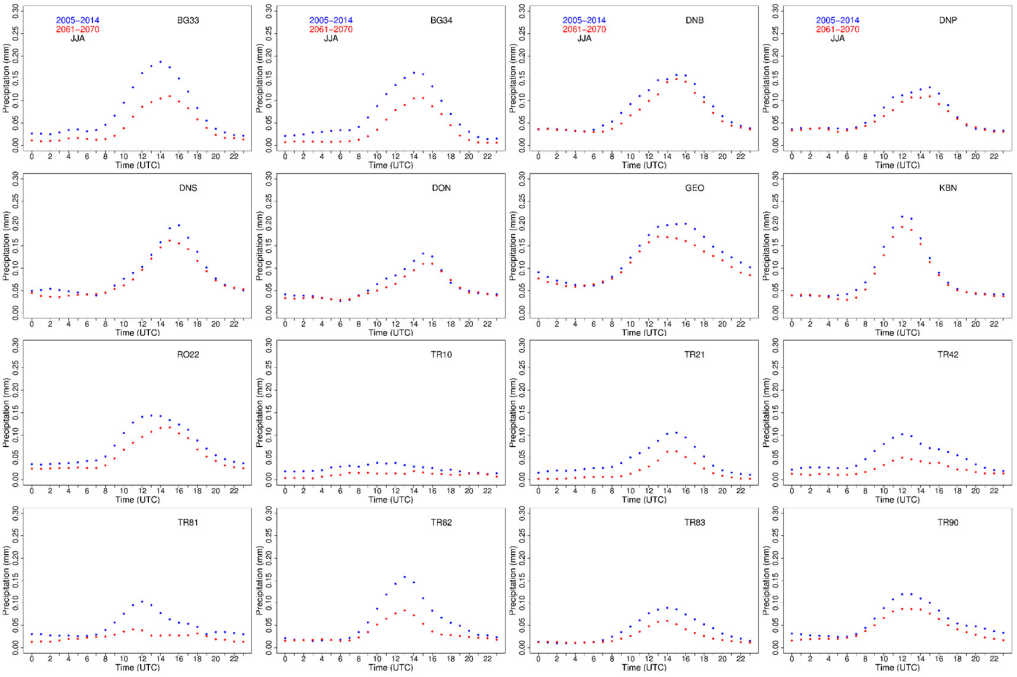

Figure 4.23 : Diurnal precipitation cycle based on mean hourly data over the coastal subregions for the reference and the future periods (summer).

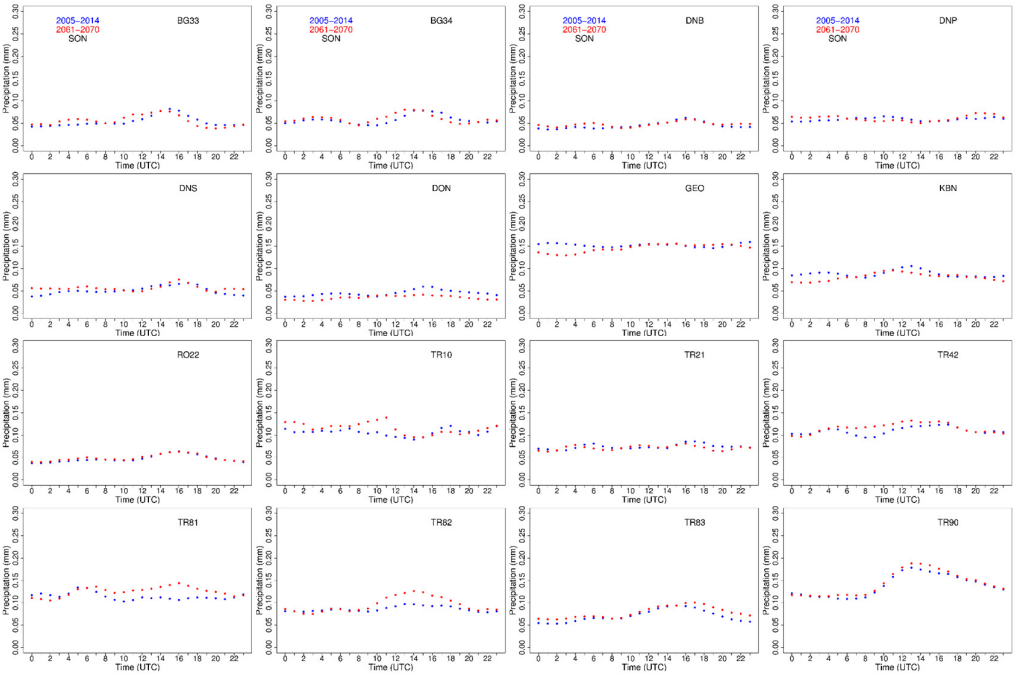

Figure 4.24 : Diurnal precipitation cycle based on mean hourly data over the coastal subregions for the reference and the future periods (autumn).

5. CONCLUSIONS AND RECOMMENDATIONS

The GCMs are the primary tools for global climate change studies. The RCMs, on the other hand, provide more detailed and physically more reliable regional climate information compared to GCMs because of their higher resolution. The recent RCMs are run at grid spacings of less or equal to 4 km, so-called the CPMs. In this study, we performed historical (2005-2014) and future (2061-2070) convection-permitting climate simulations forced with CMIP6-based SSP3-7.0 scenario produced by last generation MPI-ESM-HR GCM over the Black Sea Basin. First, we evaluated the historical simulation outputs using high-resolution gridded observational and reanalysis datasets and station observations. Following that, we examined the future changes in the climate of the Black Sea Basin. The main findings of the study are listed as follows:

- For the mean seasonal Tmax, WRFCP has a negative bias in winter and spring, especially over mountainous regions, and a positive bias of around 3°C in summer and autumn across the study area. Compared with the gridded datasets, part of these biases can be related to data production methods, i.e., reanalysis from a dynamic model or observation-based gridded data. For the mean seasonal Tmin, WRFCP has a positive bias of around 4°C in all seasons over the simulation domain. On the other hand, station-based analyses highlighted that WRFCP significantly improves the low-resolution MPI-ESM-HR outputs by reducing the monthly mean Tmax and Tmin biases and capturing the annual cycle.
- For the precipitation outputs, WRFCP has a positive bias of about 6 mm/day in winter over mountainous areas due to the positive bias of MPI-ESM-HR. The station-based analyses support this finding. In particular, WRFCP and MPI-ESM-HR have a positive bias in winter and spring at high-elevation station points.
- Although WRFCP has seasonal total precipitation biases, it significantly improves the daily precipitation amounts compared to MPI-ESM-HR outputs.

Compared with the station observations and MSWEP, the daily precipitation probabilities of WRFCP are closer to the observations than one of the MPI-ESM-HR outputs. In particular, WRFCP is superior to MPI-ESM-HR for high amounts of daily precipitation exceeding 50 mm at high-elevation station points. Moreover, subregional analyses indicate that WRFCP provides better estimations of 3-hourly precipitation probabilities for extreme precipitation values than MPI-ESM-HR when compared to MSWEP, especially over the northeast of Turkey and the Eastern Black Sea region.

- The future climate simulation results highlight that the Tmean, Tmin and Tmax increase in spring, summer, and autumn in the future. In particular, the warming rate exceeds 3°C in the summer. In the winter, there is a suppression in the warming due to increased low- and mid-level cloud covers. However, there is regional warming over the Carpathians and Eastern Anatolia due to a reduction in the surface albedo, which may be related to the shrinking snow cover over these regions, triggering the warming.
- In terms of extreme temperature, the DTR and TX90P increase in the future due to the increase in the Tmax especially over the west of the BSA and the northwest of Turkey.
- In addition to air temperature, the SST across the Black Sea increases by about 1.5°C in the future. In particular, the increase of the SST in summer reaches up to 2°C over the western and the central parts of the Black Sea.
- In terms of precipitation, there is a significant increase in winter reaching up to 3 mm/day over the Eastern Black Sea region. This precipitation increase is due to the 15% evaporation increase enhanced by the pronounced warming of the SST by about 1°C in winter over the same area. This additional moisture content in the lower troposphere is carried to the eastern coast by the strengthened mean westerly flow at 850 hPa level and leads to an increase in the precipitation. Furthermore, the weakened southerly flow at the same atmospheric level increases the moisture content over the coast of Turkey and increases the precipitation along with orographic forcing. On the other hand, the total precipitation amount decreases in spring and summer over the Black Sea Basin.

- The daily precipitation analyses indicate that extreme precipitation events increase over the area of interest. According to the subregional analyses, the most pronounced increase occurs in the coastal regions of the Black Sea Basin, where the daily precipitation amount reaches 350 mm in the future. Moreover, the daily extreme precipitation thresholds of the 90th, 99th, and 99.9th percentiles shift toward higher values, and the increase of the percentage of very wet days reaches 3% over the northeast of Turkey and Georgia. Furthermore, sub-daily precipitation analyses indicate that the hourly precipitation amounts exceed 100 mm in most subregions. In particular, in the autumn, there is an intensification in the afternoon precipitation, especially over the coastal regions of Turkey.

This study highlighted the added value of a high-resolution CPM in representing temperature and precipitation over the complex topography of the Black Sea Basin. Moreover, the significant warming of this region and the increase in daily and sub-daily precipitation amounts can increase human exposure to extreme climatic conditions. Therefore, future impact assessment studies over this region would be beneficial in developing mitigation and adaptation strategies for climate change. To this end, in future studies, high-resolution convection-permitting simulations can be performed for different future periods under different GHG emissions scenarios. Moreover, ensemble convection-permitting climate simulations forced with different GCMs would be beneficial to enhance our understanding of the future climate over the Black Sea Basin.

REFERENCES

Abatzoglou, J. T., Dobrowski, S. Z., Parks, S. A., & Hegewisch, K. C. (2018). TerraClimate, a high-resolution global dataset of monthly climate and climatic water balance from 1958–2015. *Scientific Data*, *5*(1), 170191. https://doi.org/10.1038/sdata.2017.191

Aksu, H., & Akgül, M. A. (2020). Performance evaluation of CHIRPS satellite precipitation estimates over Turkey. *Theoretical and Applied Climatology*, *142*(1–2), 71–84. https://doi.org/10.1007/s00704-020-03301-5

Aksu, H., Cetin, M., Aksoy, H., Yaldiz, S. G., Yildirim, I., & Keklik, G. (2022). Spatial and temporal characterization of standard duration-maximum precipitation over Black Sea Region in Turkey. *Natural Hazards*, *111*(3), 2379–2405. https://doi.org/10.1007/s11069-021-05141-6

Arias, P.A., N. Bellouin, E. Coppola, R.G. Jones, G. Krinner, J. Marotzke, V. Naik, M.D. Palmer, G.-K. Plattner, J. Rogelj, M. Rojas, J. Sillmann, T. Storelvmo, P.W. Thorne, B. Trewin, K. Achuta Rao, B. Adhikary, R.P. Allan, K. Armour, G. Bala, R. Barimalala, … K. Zickfeld. (2021). Technical Summary. In *Climate Change 2021: The Physical Science Basis. Contribution of Working Group I to the Sixth Assessment Report of the Intergovernmental Panel on Climate Change* [Masson-Delmotte, V., P. Zhai, A. Pirani, S.L. Connors, C. Péan, S. Berger, N. Caud, Y. Chen, L. Goldfarb, M.I. Gomis, M. Huang, K. Leitzell, E. Lonnoy, J.B.R. Matthews, T.K. Maycock, T. Waterfield, O. Yelekçi, R. Yu, and B. Zhou (eds.)]. Cambridge University Press, Cambridge, United Kingdom and New York, NY, USA, pp. 33−144. doi:10.1017/9781009157896.002.

Bağçaci, S. Ç., Yucel, I., Duzenli, E., & Yilmaz, M. T. (2021). Intercomparison of the expected change in the temperature and the precipitation retrieved from CMIP6 and CMIP5 climate projections: A Mediterranean hot spot case, Turkey. *Atmospheric Research*, *256*, 105576. https://doi.org/10.1016/j.atmosres.2021.105576

Ban, N., Rajczak, J., Schmidli, J., & Schär, C. (2020). Analysis of Alpine precipitation extremes using generalized extreme value theory in convection-resolving climate simulations. *Climate Dynamics*, *55*(1–2), 61–75. https://doi.org/10.1007/s00382-018-4339-4

Ban, N., Schmidli, J., & Schär, C. (2014). Evaluation of the convection-resolving regional climate modeling approach in decade-long simulations. *Journal of Geophysical Research: Atmospheres*, *119*(13), 7889–7907. https://doi.org/10.1002/2014JD021478

Ban, N., Schmidli, J., & Schär, C. (2015). Heavy precipitation in a changing climate: Does short-term summer precipitation increase faster? *Geophysical*

Research Letters, *42*(4), 1165–1172. https://doi.org/10.1002/2014GL062588

Batibeniz, F., Hauser, M., & Seneviratne, S. I. (2022). Countries most exposed to individual and compound extremes at different global warming levels [Preprint]. *EGUsphere,* https://doi.org/10.5194/egusphere-2022-321

Beck, H. E., Wood, E. F., Pan, M., Fisher, C. K., Miralles, D. G., van Dijk, A. I. J. M., McVicar, T. R., & Adler, R. F. (2019). MSWEP V2 Global 3-Hourly 0.1° Precipitation: Methodology and Quantitative Assessment. *Bulletin of the American Meteorological Society*, *100*(3), 473–500. https://doi.org/10.1175/BAMS-D-17-0138.1

Berthou, S., Kendon, E. J., Chan, S. C., Ban, N., Leutwyler, D., Schär, C., & Fosser, G. (2020). Pan-European climate at convection-permitting scale: A model intercomparison study. *Climate Dynamics*, *55*(1–2), 35–59. https://doi.org/10.1007/s00382-018-4114-6

Bozkurt, D., & Sen, O. L. (2011). Precipitation in the Anatolian Peninsula: Sensitivity to increased SSTs in the surrounding seas. *Climate Dynamics*, *36*(3–4), 711–726. https://doi.org/10.1007/s00382-009-0651-3

Bozkurt, D., Turuncoglu, U., Sen, O. L., Onol, B., & Dalfes, H. N. (2012). Downscaled simulations of the ECHAM5, CCSM3 and HadCM3 global models for the eastern Mediterranean–Black Sea region: Evaluation of the reference period. *Climate Dynamics*, *39*(1–2), 207–225. https://doi.org/10.1007/s00382-011-1187-x

Brisson, E., Van Weverberg, K., Demuzere, M., Devis, A., Saeed, S., Stengel, M., & van Lipzig, N. P. M. (2016). How well can a convection-permitting climate model reproduce decadal statistics of precipitation, temperature and cloud characteristics? *Climate Dynamics*, *47*(9–10), 3043–3061. https://doi.org/10.1007/s00382-016-3012-z

Broxton, P. D., Zeng, X., Sulla-Menashe, D., & Troch, P. A. (2014). A Global Land Cover Climatology Using MODIS Data. *Journal of Applied Meteorology and Climatology*, *53*(6), 1593–1605. https://doi.org/10.1175/JAMC-D-13-0270.1

Chan, S. C., Kendon, E. J., Berthou, S., Fosser, G., Lewis, E., & Fowler, H. J. (2020). Europe-wide precipitation projections at convection permitting scale with the Unified Model. *Climate Dynamics*, *55*(3–4), 409–428. https://doi.org/10.1007/s00382-020-05192-8

Coppola, E., Sobolowski, S., Pichelli, E., Raffaele, F., Ahrens, B., Anders, I., Ban, N., Bastin, S., Belda, M., Belusic, D., Caldas-Alvarez, A., Cardoso, R. M., Davolio, S., Dobler, A., Fernandez, J., Fita, L., Fumiere, Q., Giorgi, F., Goergen, K., … Warrach-Sagi, K. (2020). A first-of-its-kind multi-model convection permitting ensemble for investigating convective phenomena over Europe and the Mediterranean. *Climate Dynamics*, *55*(1–2), 3–34. https://doi.org/10.1007/s00382-018-4521-8

Cos, J., Doblas-Reyes, F., Jury, M., Marcos, R., Bretonnière, P.-A., & Samsó, M. (2022). The Mediterranean climate change hotspot in the CMIP5 and CMIP6 projections. *Earth System Dynamics*, *13*(1), 321–340. https://doi.org/10.5194/esd-13-321-2022

Dai, A., Giorgi, F., & Trenberth, K. E. (1999). Observed and model-simulated diurnal cycles of precipitation over the contiguous United States. *Journal of Geophysical Research: Atmospheres*, *104*(D6), 6377–6402. https://doi.org/10.1029/98JD02720

Danielson, J. J., & Gesch, D. B. (2011). Global multi-resolution terrain elevation data 2010 (GMTED2010). In Open-File Report. US Geological Survey. https://doi.org/10.3133/ofr20111073

Dickinson, RobertE., Errico, RonaldM., Giorgi, F., & Bates, GaryT. (1989). A regional climate model for the western United States. *Climatic Change*, *15*(3). https://doi.org/10.1007/BF00240465

Diez-Sierra, J., Iturbide, M., Gutiérrez, J. M., Fernández, J., Milovac, J., Cofiño, A. S., Cimadevilla, E., Nikulin, G., Levavasseur, G., Kjellström, E., Bülow, K., Horányi, A., Brookshaw, A., García-Díez, M., Pérez, A., Baño-Medina, J., Ahrens, B., Alias, A., Ashfaq, M., … Zittis, G. (2022). The worldwide C3S CORDEX grand ensemble: A major contribution to assess regional climate change in the IPCC AR6 Atlas. *Bulletin of the American Meteorological Society*. https://doi.org/10.1175/BAMS-D-22-0111.1

Diffenbaugh, N. S., & Giorgi, F. (2012). Climate change hotspots in the CMIP5 global climate model ensemble. *Climatic Change*, *114*(3–4), 813–822. https://doi.org/10.1007/s10584-012-0570-x

Dirmeyer, P. A., Jin, Y., Singh, B., & Yan, X. (2013). Trends in Land–Atmosphere Interactions from CMIP5 Simulations. *Journal of Hydrometeorology*, *14*(3), 829–849. https://doi.org/10.1175/JHM-D-12-0107.1

Doblas-Reyes, F.J., A.A. Sörensson, M. Almazroui, A. Dosio, W.J. Gutowski, R. Haarsma, R. Hamdi, B. Hewitson, W.-T. Kwon, B.L. Lamptey, D. Maraun, T.S. Stephenson, I. Takayabu, L. Terray, A. Turner, and Z. Zuo. (2021). Linking Global to Regional Climate Change. In *Climate Change 2021: The Physical Science Basis. Contribution of Working Group I to the Sixth Assessment Report of the Intergovernmental Panel on Climate Change* [Masson-Delmotte, V., P. Zhai, A. Pirani, S.L. Connors, C. Péan, S. Berger, N. Caud, Y. Chen, L. Goldfarb, M.I. Gomis, M. Huang, K. Leitzell, E. Lonnoy, J.B.R. Matthews, T.K. Maycock, T. Waterfield, O. Yelekçi, R. Yu, and B. Zhou (eds.)]. Cambridge University Press, Cambridge, United Kingdom and New York, NY, USA, pp. 1363–1512, doi:10.1017/9781009157896.012.

Doğan, O. H. (2018). *Şiddetli yağışların Karadeniz yüzey sıcaklığına duyarlılığının Artvin/Hopa seli özelinde topluluk simülasyonları üretilerek incelenmesi.* (Master thesis). Istanbul Technical University, Institute of Science and Technology, Istanbul.

Ek, M. B., Mitchell, K. E., Lin, Y., Rogers, E., Grunmann, P., Koren, V., Gayno, G., & Tarpley, J. D. (2003). Implementation of Noah land surface model advances in the National Centers for Environmental Prediction operational mesoscale Eta model. *Journal of Geophysical Research: Atmospheres*, *108*(D22), 2002JD003296. https://doi.org/10.1029/2002JD003296

European Commission. Statistical Office of the European Union. (2022). *Statistical regions in the European Union and partner countries: NUTS and statistical regions 2021 : 2022 edition.* Publications Office. https://data.europa.eu/doi/10.2785/321792

Eyring, V., Bony, S., Meehl, G. A., Senior, C. A., Stevens, B., Stouffer, R. J., & Taylor, K. E. (2016). Overview of the Coupled Model Intercomparison Project Phase 6 (CMIP6) experimental design and organization. *Geoscientific Model Development*, *9*(5), 1937–1958. https://doi.org/10.5194/gmd-9-1937-2016

Feser, F., Rockel, B., von Storch, H., Winterfeldt, J., & Zahn, M. (2011). Regional Climate Models Add Value to Global Model Data: A Review and Selected Examples. *Bulletin of the American Meteorological Society*, *92*(9), 1181–1192. https://doi.org/10.1175/2011BAMS3061.1

Fosser, G., Khodayar, S., & Berg, P. (2015). Benefit of convection permitting climate model simulations in the representation of convective precipitation. *Climate Dynamics*, *44*(1–2), 45–60. https://doi.org/10.1007/s00382-014-2242-1

Fumière, Q., Déqué, M., Nuissier, O., Somot, S., Alias, A., Caillaud, C., Laurantin, O., & Seity, Y. (2020). Extreme rainfall in Mediterranean France during the fall: Added value of the CNRM-AROME Convection-Permitting Regional Climate Model. *Climate Dynamics*, *55*(1–2), 77–91. https://doi.org/10.1007/s00382-019-04898-8

Funk, C., Peterson, P., Landsfeld, M., Pedreros, D., Verdin, J., Shukla, S., Husak, G., Rowland, J., Harrison, L., Hoell, A., & Michaelsen, J. (2015). The climate hazards infrared precipitation with stations—A new environmental record for monitoring extremes. *Scientific Data*, *2*(1), 150066. https://doi.org/10.1038/sdata.2015.66

Giorgi, F. (2006). Climate change hot-spots. *Geophysical Research Letters*, *33*(8), L08707. https://doi.org/10.1029/2006GL025734

Giorgi, F. (2019). Thirty Years of Regional Climate Modeling: Where Are We and Where Are We Going next? *Journal of Geophysical Research: Atmospheres*, 2018JD030094. https://doi.org/10.1029/2018JD030094

Giorgi, F., & Bates, G. T. (1989). The Climatological Skill of a Regional Model over Complex Terrain. *Monthly Weather Review*, *117*(11), 2325–2347. https://doi.org/10.1175/1520-0493(1989)117<2325:TCSOAR>2.0.CO;2

Giorgi, F., Coppola, E., Jacob, D., Teichmann, C., Abba Omar, S., Ashfaq, M., Ban, N., Bülow, K., Bukovsky, M., Buntemeyer, L., Cavazos, T., Ciarlo`, J., da Rocha, R. P., Das, S., di Sante, F., Evans, J. P., Gao, X., Giuliani, G., Glazer, R. H., … Weber, T. (2022). The CORDEX-CORE EXP-I Initiative: Description and Highlight Results from the Initial Analysis. *Bulletin of the American Meteorological Society*, *103*(2), E293–E310. https://doi.org/10.1175/BAMS-D-21-0119.1

Giorgi, F., & Gutowski, W. J. (2015). Regional Dynamical Downscaling and the CORDEX Initiative. *Annual Review of Environment and Resources*,

40(1), 467–490. https://doi.org/10.1146/annurev-environ-102014-021217

Giorgi, F., Jones, C., & Asrar, G. R. (2009). *Addressing climate information needs at the regional level: The CORDEX framework*. 9.

GRDC. (2020). *Major River Basins of the World.* Global Runoff Data Centre, GRDC. 2nd, rev. ext. ed. Koblenz, Germany: Federal Institute of Hydrology (BfG).

Gutjahr, O., Putrasahan, D., Lohmann, K., Jungclaus, J. H., von Storch, J.-S., Brüggemann, N., Haak, H., & Stössel, A. (2019). Max Planck Institute Earth System Model (MPI-ESM1.2) for the High-Resolution Model Intercomparison Project (HighResMIP). *Geoscientific Model Development*, *12*(7), 3241–3281. https://doi.org/10.5194/gmd-12-3241-2019

Gutowski Jr., W. J., Giorgi, F., Timbal, B., Frigon, A., Jacob, D., Kang, H.-S., Raghavan, K., Lee, B., Lennard, C., Nikulin, G., O'Rourke, E., Rixen, M., Solman, S., Stephenson, T., & Tangang, F. (2016). WCRP COordinated Regional Downscaling EXperiment (CORDEX): A diagnostic MIP for CMIP6. *Geoscientific Model Development*, *9*(11), 4087–4095. https://doi.org/10.5194/gmd-9-4087-2016

Gutowski, W. J., Ullrich, P. A., Hall, A., Leung, L. R., O'Brien, T. A., Patricola, C. M., Arritt, R. W., Bukovsky, M. S., Calvin, K. V., Feng, Z., Jones, A. D., Kooperman, G. J., Monier, E., Pritchard, M. S., Pryor, S. C., Qian, Y., Rhoades, A. M., Roberts, A. F., Sakaguchi, K., … Zarzycki, C. (2020). The Ongoing Need for High-Resolution Regional Climate Models: Process Understanding and Stakeholder Information. *Bulletin of the American Meteorological Society*, *101*(5), E664–E683. https://doi.org/10.1175/BAMS-D-19-0113.1

Haarsma, R. J., Roberts, M. J., Vidale, P. L., Senior, C. A., Bellucci, A., Bao, Q., Chang, P., Corti, S., Fučkar, N. S., Guemas, V., von Hardenberg, J., Hazeleger, W., Kodama, C., Koenigk, T., Leung, L. R., Lu, J., Luo, J.-J., Mao, J., Mizielinski, M. S., … von Storch, J.-S. (2016). High Resolution Model Intercomparison Project (HighResMIP v1.0) for CMIP6. *Geoscientific Model Development*, *9*(11), 4185–4208. https://doi.org/10.5194/gmd-9-4185-2016

Hohenegger, C., Brockhaus, P., Bretherton, C. S., & Schär, C. (2009). The Soil Moisture–Precipitation Feedback in Simulations with Explicit and Parameterized Convection. *Journal of Climate*, *22*(19), 5003–5020. https://doi.org/10.1175/2009JCLI2604.1

Hohenegger, C., Brockhaus, P., & Schär, C. (2008). Towards climate simulations at cloud-resolving scales. *Meteorologische Zeitschrift*, *17*(4), 383–394. https://doi.org/10.1127/0941-2948/2008/0303

Hong, S.-Y., Noh, Y., & Dudhia, J. (2006). A New Vertical Diffusion Package with an Explicit Treatment of Entrainment Processes. *Monthly Weather Review*, *134*(9), 2318–2341. https://doi.org/10.1175/MWR3199.1

Houghton, J. T. (Ed.). (1996). *Climate change 1995: The science of climate change*. Cambridge University Press.

Houghton, J. T., Callander, B. A., Varney, S. K., & Intergovernmental Panel on Climate Change (Eds.). (1992). *Climate change 1992: The supplementary report to the IPCC scientific assessment*. Cambridge University Press.

Iacono, M. J., Delamere, J. S., Mlawer, E. J., Shephard, M. W., Clough, S. A., & Collins, W. D. (2008). Radiative forcing by long-lived greenhouse gases: Calculations with the AER radiative transfer models. *Journal of Geophysical Research*, *113*(D13), D13103. https://doi.org/10.1029/2008JD009944

Jiménez, P. A., Dudhia, J., González-Rouco, J. F., Navarro, J., Montávez, J. P., & García-Bustamante, E. (2012). A Revised Scheme for the WRF Surface Layer Formulation. *Monthly Weather Review*, *140*(3), 898–918. https://doi.org/10.1175/MWR-D-11-00056.1

Kelebek, M. B., Batibeniz, F., & Önol, B. (2021). Exposure Assessment of Climate Extremes over the Europe–Mediterranean Region. *Atmosphere*, *12*(5), 633. https://doi.org/10.3390/atmos12050633

Kendon, E. J., Ban, N., Roberts, N. M., Fowler, H. J., Roberts, M. J., Chan, S. C., Evans, J. P., Fosser, G., & Wilkinson, J. M. (2017). Do Convection-Permitting Regional Climate Models Improve Projections of Future Precipitation Change? *Bulletin of the American Meteorological Society*, *98*(1), 79–93. https://doi.org/10.1175/BAMS-D-15-0004.1

Kendon, E. J., Roberts, N. M., Fowler, H. J., Roberts, M. J., Chan, S. C., & Senior, C. A. (2014). Heavier summer downpours with climate change revealed by weather forecast resolution model. *Nature Climate Change*, *4*(7), 570–576. https://doi.org/10.1038/nclimate2258

Kendon, E. J., Roberts, N. M., Senior, C. A., & Roberts, M. J. (2012). Realism of Rainfall in a Very High-Resolution Regional Climate Model. *Journal of Climate*, *25*(17), 5791–5806. https://doi.org/10.1175/JCLI-D-11-00562.1

Kindap, T. (2010). A severe sea-effect snow episode over the city of Istanbul. *Natural Hazards*, *54*(3), 707–723. https://doi.org/10.1007/s11069-009-9496-7

Knist, S., Goergen, K., & Simmer, C. (2020). Evaluation and projected changes of precipitation statistics in convection-permitting WRF climate simulations over Central Europe. *Climate Dynamics*, *55*(1–2), 325–341. https://doi.org/10.1007/s00382-018-4147-x

Leutwyler, D., Fuhrer, O., Lapillonne, X., Lüthi, D., & Schär, C. (2016). Towards European-scale convection-resolving climate simulations with GPUs: A study with COSMO 4.19. *Geoscientific Model Development*, *9*(9), 3393–3412. https://doi.org/10.5194/gmd-9-3393-2016

Leutwyler, D., Imamovic, A., & Schär, C. (2021). The Continental-Scale Soil-Moisture Precipitation Feedback in Europe with Parameterized and Explicit Convection. *Journal of Climate*, 1–56. https://doi.org/10.1175/JCLI-D-20-0415.1

Leutwyler, D., Lüthi, D., Ban, N., Fuhrer, O., & Schär, C. (2017). Evaluation of the convection-resolving climate modeling approach on continental

scales. *Journal of Geophysical Research: Atmospheres*, *122*(10), 5237–5258. https://doi.org/10.1002/2016JD026013

Lima, L., Ciliberti, S. A., Aydoğdu, A., Masina, S., Escudier, R., Cipollone, A., Azevedo, D., Causio, S., Peneva, E., Lecci, R., Clementi, E., Jansen, E., Ilicak, M., Cretì, S., Stefanizzi, L., Palermo, F., & Coppini, G. (2021). Climate Signals in the Black Sea From a Multidecadal Eddy-Resolving Reanalysis. *Frontiers in Marine Science*, *8*, 710973. https://doi.org/10.3389/fmars.2021.710973

Lionello, P., & Scarascia, L. (2018). The relation between climate change in the Mediterranean region and global warming. *Regional Environmental Change*, *18*(5), 1481–1493. https://doi.org/10.1007/s10113-018-1290-1

Liu, C., Ikeda, K., Rasmussen, R., Barlage, M., Newman, A. J., Prein, A. F., Chen, F., Chen, L., Clark, M., Dai, A., Dudhia, J., Eidhammer, T., Gochis, D., Gutmann, E., Kurkute, S., Li, Y., Thompson, G., & Yates, D. (2017). Continental-scale convection-permitting modeling of the current and future climate of North America. *Climate Dynamics*, *49*(1–2), 71–95. https://doi.org/10.1007/s00382-016-3327-9

Liu, Z., Gao, Y., & Zhang, G. (2022). How well can a convection-permitting-modelling improve the simulation of summer precipitation diurnal cycle over the Tibetan Plateau? *Climate Dynamics*, *58*(11–12), 3121–3138. https://doi.org/10.1007/s00382-021-06090-3

Lucas-Picher, P., Argüeso, D., Brisson, E., Tramblay, Y., Berg, P., Lemonsu, A., Kotlarski, S., & Caillaud, C. (2021). Convection-permitting modeling with regional climate models: Latest developments and next steps. *WIREs Climate Change*, *12*(6). https://doi.org/10.1002/wcc.731

Meehl, G. A., G.J. Boer, C. Covey, M. Latif, and R.J. Stouffer. (1997). Intercomparison makes for a better climate model. *Eos, Trans. Amer. Geophys. Union, 78*, 445–446, 451.

Meehl, G. A., Boer, G. J., Covey, C., Latif, M., & Stouffer, R. J. (2000). The Coupled Model Intercomparison Project (CMIP). *Bulletin of the American Meteorological Society*, *81*(2), 313–318. https://doi.org/10.1175/1520-0477(2000)081<0313:TCMIPC>2.3.CO;2

Meehl, G. A., Covey, C., Delworth, T., Latif, M., McAvaney, B., Mitchell, J. F. B., Stouffer, R. J., & Taylor, K. E. (2007). THE WCRP CMIP3 Multimodel Dataset: A New Era in Climate Change Research. *Bulletin of the American Meteorological Society*, *88*(9), 1383–1394. https://doi.org/10.1175/BAMS-88-9-1383

Meinshausen, M., Nicholls, Z. R. J., Lewis, J., Gidden, M. J., Vogel, E., Freund, M., Beyerle, U., Gessner, C., Nauels, A., Bauer, N., Canadell, J. G., Daniel, J. S., John, A., Krummel, P. B., Luderer, G., Meinshausen, N., Montzka, S. A., Rayner, P. J., Reimann, S., … Wang, R. H. J. (2020). The shared socio-economic pathway (SSP) greenhouse gas concentrations and their extensions to 2500. *Geoscientific Model*

Development, *13*(8), 3571–3605. https://doi.org/10.5194/gmd-13-3571-2020

Meredith, E. P., Semenov, V. A., Maraun, D., Park, W., & Chernokulsky, A. V. (2015). Crucial role of Black Sea warming in amplifying the 2012 Krymsk precipitation extreme. *Nature Geoscience*, *8*(8), 615–619. https://doi.org/10.1038/ngeo2483

Mohamed, B., Ibrahim, O., & Nagy, H. (2022). Sea Surface Temperature Variability and Marine Heatwaves in the Black Sea. *Remote Sensing*, *14*(10), 2383. https://doi.org/10.3390/rs14102383

Moss, R. (Ed.). (2008). *Towards new scenarios for analysis of emissions, climate change, impacts, and response strategies.* Intergovernmental Panel on Climate Change.

Muñoz Sabater, J. (2019). *ERA5-Land hourly data from 1981 to present.* Copernicus Climate Change Service (C3S) Climate Data Store (CDS).

Nakićenović, N. (Ed.). (2000). *Special report on emissions scenarios: A special report of Working Group III of the Intergovernmental Panel on Climate Change*. Cambridge University Press.

O'Neill, B. C., Kriegler, E., Ebi, K. L., Kemp-Benedict, E., Riahi, K., Rothman, D. S., van Ruijven, B. J., van Vuuren, D. P., Birkmann, J., Kok, K., Levy, M., & Solecki, W. (2017). The roads ahead: Narratives for shared socioeconomic pathways describing world futures in the 21st century. *Global Environmental Change*, *42*, 169–180. https://doi.org/10.1016/j.gloenvcha.2015.01.004

Önol, B. (2012). Effects of coastal topography on climate: High-resolution simulation with a regional climate model. *Climate Research*, *52*, 159–174. https://doi.org/10.3354/cr01077

Önol, B., Bozkurt, D., Turuncoglu, U. U., Sen, O. L., & Dalfes, H. N. (2014). Evaluation of the twenty-first century RCM simulations driven by multiple GCMs over the Eastern Mediterranean–Black Sea region. *Climate Dynamics*, *42*(7–8), 1949–1965. https://doi.org/10.1007/s00382-013-1966-7

Önol, B., & H. M. Semazzi, F. (2009). Regionalization of Climate Change Simulations over the Eastern Mediterranean. *Journal of Climate*, *22*(8), 1944–1961. https://doi.org/10.1175/2008JCLI1807.1

Önol, B., & Unal, Y. S. (2014). Assessment of climate change simulations over climate zones of Turkey. *Regional Environmental Change*, *14*(5), 1921–1935. https://doi.org/10.1007/s10113-012-0335-0

Pachauri, R. K. (Ed.). (2008). *Climate change 2007: Synthesis Report*. IPCC.

Pachauri, R. K., & Mayer, L. (Eds.). (2015). *Climate change 2014: Synthesis Report*. Intergovernmental Panel on Climate Change.

Pal, S., Chang, H.-I., Castro, C. L., & Dominguez, F. (2019). Credibility of Convection-Permitting Modeling to Improve Seasonal Precipitation Forecasting in the Southwestern United States. *Frontiers in Earth Science*, *7*, 11. https://doi.org/10.3389/feart.2019.00011

Prein, A. F., Gobiet, A., Suklitsch, M., Truhetz, H., Awan, N. K., Keuler, K., & Georgievski, G. (2013). Added value of convection permitting seasonal simulations. *Climate Dynamics*, *41*(9–10), 2655–2677. https://doi.org/10.1007/s00382-013-1744-6

Prein, A. F., Langhans, W., Fosser, G., Ferrone, A., Ban, N., Goergen, K., Keller, M., Tölle, M., Gutjahr, O., Feser, F., Brisson, E., Kollet, S., Schmidli, J., Lipzig, N. P. M., & Leung, R. (2015). A review on regional convection-permitting climate modeling: Demonstrations, prospects, and challenges. *Reviews of Geophysics*, *53*(2), 323–361. https://doi.org/10.1002/2014RG000475

Prein, A. F., Liu, C., Ikeda, K., Bullock, R., Rasmussen, R. M., Holland, G. J., & Clark, M. (2020). Simulating North American mesoscale convective systems with a convection-permitting climate model. *Climate Dynamics*, *55*(1–2), 95–110. https://doi.org/10.1007/s00382-017-3993-2

Rummukainen, M. (2016). Added value in regional climate modeling. *WIREs Climate Change*, *7*(1), 145–159. https://doi.org/10.1002/wcc.378

Ruti, P. M., Somot, S., Giorgi, F., Dubois, C., Flaounas, E., Obermann, A., Dell'Aquila, A., Pisacane, G., Harzallah, A., Lombardi, E., Ahrens, B., Akhtar, N., Alias, A., Arsouze, T., Aznar, R., Bastin, S., Bartholy, J., Béranger, K., Beuvier, J., … Vervatis, V. (2016). Med-CORDEX Initiative for Mediterranean Climate Studies. *Bulletin of the American Meteorological Society*, *97*(7), 1187–1208. https://doi.org/10.1175/BAMS-D-14-00176.1

Sakalli, A., & Başusta, N. (2018). Sea surface temperature change in the Black Sea under climate change: A simulation of the sea surface temperature up to 2100. *International Journal of Climatology*, *38*(13), 4687–4698. https://doi.org/10.1002/joc.5688

Seneviratne, S. I., Nicholls, N., Easterling, D., Goodess, C. M., Kanae, S., Kossin, J., Luo, Y., Marengo, J., McInnes, K., Rahimi, M., Reichstein, M., Sorteberg, A., Vera, C., Zhang, X., Rusticucci, M., Semenov, V., Alexander, L. V., Allen, S., Benito, G., … Zwiers, F. W. (2012). Changes in Climate Extremes and their Impacts on the Natural Physical Environment. In C. B. Field, V. Barros, T. F. Stocker, & Q. Dahe (Eds.), *Managing the Risks of Extreme Events and Disasters to Advance Climate Change Adaptation* (1st ed., pp. 109–230). Cambridge University Press. https://doi.org/10.1017/CBO9781139177245.006

Seneviratne, S. I., Wilhelm, M., Stanelle, T., Hurk, B., Hagemann, S., Berg, A., Cheruy, F., Higgins, M. E., Meier, A., Brovkin, V., Claussen, M., Ducharne, A., Dufresne, J., Findell, K. L., Ghattas, J., Lawrence, D. M., Malyshev, S., Rummukainen, M., & Smith, B. (2013). Impact of soil moisture-climate feedbacks on CMIP5 projections: First results from the GLACE-CMIP5 experiment. *Geophysical Research Letters*, *40*(19), 5212–5217. https://doi.org/10.1002/grl.50956

Seneviratne, S.I., X. Zhang, M. Adnan, W. Badi, C. Dereczynski, A. Di Luca, S. Ghosh, I. Iskandar, J. Kossin, S. Lewis, F. Otto, I. Pinto, M. Satoh, S.M. Vicente-Serrano, M. Wehner, and B. Zhou. (2021). Weather

and Climate Extreme Events in a Changing Climate. In *Climate Change 2021: The Physical Science Basis. Contribution of Working Group I to the Sixth Assessment Report of the Intergovernmental Panel on Climate Change* [Masson-Delmotte, V., P. Zhai, A. Pirani, S.L. Connors, C. Péan, S. Berger, N. Caud, Y. Chen, L. Goldfarb, M.I. Gomis, M. Huang, K. Leitzell, E. Lonnoy, J.B.R. Matthews, T.K. Maycock, T. Waterfield, O. Yelekçi, R. Yu, and B. Zhou (eds.)]. Cambridge University Press, Cambridge, United Kingdom and New York, NY, USA, pp. 1513–1766, doi:10.1017/9781009157896.013.

Shaltout, M., & Omstedt, A. (2014). Recent sea surface temperature trends and future scenarios for the Mediterranean Sea. *Oceanologia*, *56*(3), 411–443. https://doi.org/10.5697/oc.56-3.411

Skamarock, W. C., Klemp, J. B., Dudhia, J., Gill, D. O., Barker, D.M., Duda, M.G., Huang, X.Y. , Wang, W. , Powers, J.G. (2008). A Description of the Advanced Research WRF Version 3, NCAR.

Sonuç, C. Y., Ünal, Y. S., İncecik, S. (2022). Convection-permitting climate simulations with COSMO-CLM over northwestern Turkey under the RCP8.5 scenario. Manuscript submitted for publication.

Stocchi, P., Pichelli, E., Torres Alavez, J. A., Coppola, E., Giuliani, G., & Giorgi, F. (2022). Non-Hydrostatic Regcm4 (Regcm4-NH): Evaluation of Precipitation Statistics at the Convection-Permitting Scale over Different Domains. *Atmosphere*, *13*(6), 861. https://doi.org/10.3390/atmos13060861

Taylor, C. M., Birch, C. E., Parker, D. J., Dixon, N., Guichard, F., Nikulin, G., & Lister, G. M. S. (2013). Modeling soil moisture-precipitation feedback in the Sahel: Importance of spatial scale versus convective parameterization. *Geophysical Research Letters*, *40*(23), 6213–6218. https://doi.org/10.1002/2013GL058511

Taylor, K. E., Stouffer, R. J., & Meehl, G. A. (2012). An Overview of CMIP5 and the Experiment Design. *Bulletin of the American Meteorological Society*, *93*(4), 485–498. https://doi.org/10.1175/BAMS-D-11-00094.1

Thompson, G., Field, P. R., Rasmussen, R. M., & Hall, W. D. (2008). Explicit Forecasts of Winter Precipitation Using an Improved Bulk Microphysics Scheme. Part II: Implementation of a New Snow Parameterization. *Monthly Weather Review*, *136*(12), 5095–5115. https://doi.org/10.1175/2008MWR2387.1

Vogel, M. M., Hauser, M., & Seneviratne, S. I. (2020). Projected changes in hot, dry and wet extreme events' clusters in CMIP6 multi-model ensemble. *Environmental Research Letters*, *15*(9), 094021. https://doi.org/10.1088/1748-9326/ab90a7

Watson, R. T., Albritton, D. L., Intergovernmental Panel on Climate Change, Intergovernmental Panel on Climate Change, & Intergovernmental Panel on Climate Change (Eds.). (2001). *Climate change 2001: Synthesis Report*. Cambridge University Press.

Yun, Y., Liu, C., Luo, Y., Liang, X., Huang, L., Chen, F., & Rasmmusen, R. (2020). Convection-permitting regional climate simulation of warm-

season precipitation over Eastern China. *Climate Dynamics*, *54*(3–4), 1469–1489. https://doi.org/10.1007/s00382-019-05070-y

Yürük, C. & Ünal, Y. S. (2017a). Performance Evaluation of COSMO-CLM over Istanbul. *COSMO/CLM/ICON/ART User Seminar*, Offenbach, Germany, 6-8 March 2017.

Yürük, C. & Ünal, Y. S. (2017b). Comparison of the Climate Extremes of the High Resolution COSMO-CLM Simulations with Observations in Istanbul City. *International Conference on Meteorology and Climatology of the Mediterranean MetMed2017*, Zagreb, Croatia, 20-22 February 2017.

Url-1 <https://cds.climate.copernicus.eu/cdsapp#!/dataset/reanalysis-era5-land>, date retrieved 21.11.2022.

CURRICULUM VITAE

Name Surname : Mehmet Barış Kelebek

- **B.Sc.** **:** 2020, Istanbul Technical University, Faculty of Aeronautics and Astronautics, Department of Meteorological Engineering

PROFESSIONAL EXPERIENCE:

- Research Assistant - Istanbul Technical University Faculty of Aeronautics and Astronautics (2020-).

PUBLICATIONS, PRESENTATIONS AND PATENTS ON THE THESIS:

- **Kelebek, M. B. & Önol, B.** (2022). Evaluation of Historical CMIP6 Based Convection-Permitting Climate Simulation over the Black Sea Region. *10th Atmospheric Sciences Symposium*, Istanbul, Turkey, 18-21 October 2022. (Presentation Instance)
- **Kelebek, M. B. & Önol, B.** (2022). Sensitivity to Microphysics and PBL Schemes for Extreme Precipitation over the Black Sea Region in Future Climate: Warm and Cold Cases. *EGU General Assembly 2022*, Vienna, Austria, 23–27 May 2022, https://doi.org/10.5194/egusphere-egu22-408. (Presentation Instance)

OTHER PUBLICATIONS, PRESENTATIONS AND PATENTS:

- **Kelebek, M. B., Batibeniz, F., & Önol, B.** (2022). Multi-hazard assessment over Europe-Mediterranean Region. *DAMOCLES Final Conference: Perspectives and ways forward in Compound Event research*, Lisbon, Portugal, 6–8 September 2022.
- **Kelebek, M. B., Batibeniz, F., & Önol, B.** (2022). Changes in Modified Climate Extremes Index (mCEI) Over Turkey. *Japan Geoscience Union Meeting 2022*, Chiba, Japan, May 29 - June 3, 2022.
- **Kelebek, M. B., Batibeniz, F., & Önol, B.** (2021). Exposure Assessment of Climate Extremes over the Europe–Mediterranean Region. *Atmosphere, 12*(5), 633. https://doi.org/10.3390/atmos12050633

- **Kelebek, M. B., Batibeniz, F., & Önol, B.** (2021). CHANGES IN COMBINED EFFECT OF EXTREMES BASED ON MODIFIED CLIMATE EXTREMES INDEX (mCEI) OVER THE EUROPEMEDITERRANEAN REGION. *EGU General Assembly 2021*, Vienna, Austria, 19–30 April 2021, https://doi.org/10.5194/egusphere-egu21-12087.
- **Kelebek, M. B., Batibeniz, F., & Önol, B.** (2019). Recent Changes in the Climate Extremes Based on Modified Climate Extremes Index Over Europe-Mediterranean Climate Hotspot. *9th Atmospheric Sciences Symposium*, Istanbul, Turkey.
- **Kelebek, M. B., Batibeniz, F., & Önol, B.** (2018). Combined Effects of Temperature and Precipitation Extremes Based on Climate Extremes Index over Europe. *MedCLIVAR 2018*, Belgrade, Serbia.
- **Kelebek, M. B., Batibeniz, F., & Önol, B.** (2017). Analysis of Climate Extremes Index Over Turkey. *9th Atmospheric Sciences Symposium*, Istanbul, Turkey.